

# **Adaptive Controllers for Assistive Robotic Devices**

by

Jeffrey R. Koller

A dissertation submitted in partial fulfillment  
of the requirements for the degree of  
Doctor of Philosophy  
(Mechanical Engineering)  
in the University of Michigan  
2018

## Doctoral Committee:

Professor Daniel P. Ferris, Co-Chair, University of Florida  
Associate Professor C. David Remy, Co-Chair  
Associate Professor Deanna Gates  
Professor Brent Gillespie  
Professor Noel C. Perkins

Jeffrey R. Koller  
jrkoller@umich.edu  
ORCID iD: 0000-0003-1436-1619

---

©Jeffrey R. Koller, 2018

To my parents, for all of the loving support and continued encouragement throughout the years. I would not be who I am today without you.

## *Acknowledgments*

None of this graduate work would have been possible without the support from friends, family, and a great academic community.

First and foremost, I would like to thank my advisers David Remy and Dan Ferris for their support, guidance, and mentorship throughout my time at Michigan. Dan, thank you for giving me the opportunity to explore my interests and teaching me the necessary foundations to be a mechanical engineer working in a kinesiology lab. David, thank you for knowing how to push and motivate me to expand my knowledge base both academically and professionally. You both have taught and exposed me to so many valuable new skills, techniques, and research practices that I could not have learned without you.

Additionally, I would like to thank Sandy Mouch, Kevin Rabideau, and Reilley Jones for their tremendous help with data collections and data processing.

I would also like to acknowledge Noel Perkins and Alex Shorter who gave me the opportunity to teach on a larger scale. The skills I gained from teaching under you both have had a major impact on how I present my work and the directions I intend to take my future career.

To my friends Yevgeniy Yesilevskiy and Ben Marchi, graduate school would not have been the same without you two. Thank you for the support, friendship, and good times throughout this process. I think I would have gone mad without our late night homework sessions, bike rides, runs, weekday lunches, or overall debauchery.

I would like to thank my parents and my sister for their constant love and encouragement. You guys were always there to talk, listen, and help me work things through when I needed it most. I would also like to thank my Ann Arbor family, Keith, Dina, and Aaron Kurz, for their support. It has made a world of difference having such loving family near by.

Finally, I would like to thank my partner Sarah Kurz who has been by my side throughout this journey. Thank you for all the amazing Ann Arbor memories, grounding me, and being there for me every step of the way.

## *Preface*

Chapters 2-5 have each been written as separate manuscripts. Given this, there may be some repetition of presented material, particularly in the methodology of experiments, between Chapters 2 and 3 as well as between Chapters 4 and 5.

# TABLE OF CONTENTS

<b>Dedication</b> . . . . .	<b>ii</b>
<b>Acknowledgments</b> . . . . .	<b>iii</b>
<b>Preface</b> . . . . .	<b>iv</b>
<b>List of Figures</b> . . . . .	<b>viii</b>
<b>List of Tables</b> . . . . .	<b>x</b>
<b>Abstract</b> . . . . .	<b>xi</b>
 <b>Chapter</b>	
<b>1 The Control of Assistive Robotic Devices</b> . . . . .	<b>1</b>
1.1 Motivation and Identifying a Need for Research . . . . .	1
1.2 State of the Art . . . . .	4
1.3 Contributions . . . . .	9
<b>2 Confidence in the Curve: Establishing Instantaneous Cost Mapping Tech- niques using Bilateral Ankle Exoskeletons</b> . . . . .	<b>11</b>
2.1 Introduction . . . . .	11
2.2 Methods . . . . .	14
2.2.1 Mapping of a Metabolic Cost Landscape . . . . .	14
2.2.2 Representing an Estimate of the Metabolic Cost Landscape . . . . .	14
2.2.3 Measuring $x(\mathbf{p})$ . . . . .	15
2.2.4 Metabolic Cost Mapping Analyses . . . . .	16
2.2.5 Confidence in the Curve . . . . .	19
2.2.6 Validation Study with Ankle Exoskeletons . . . . .	24
2.3 Results . . . . .	28
2.3.1 Step Exploration with an ICM Analysis . . . . .	29
2.3.2 Ramp Exploration with an ICM Analysis . . . . .	30
2.4 Discussion & Conclusion . . . . .	31
2.5 Appendix: Proving an Analytic Solution to Solving the Confidence Band of a Curve . . . . .	34
<b>3 ‘Body-in-the-Loop’ Optimization of Assistive Robotic Devices</b> . . . . .	<b>36</b>
3.1 Introduction . . . . .	36

3.2	A Pneumatically Actuated Robotic Ankle Exoskeleton . . . . .	39
3.2.1	Hardware . . . . .	40
3.2.2	Control . . . . .	41
3.3	Metabolic Effort as a Physiological Cost Function . . . . .	42
3.4	Optimization of Metabolic Effort . . . . .	43
3.4.1	Establishing a Ground Truth . . . . .	43
3.4.2	Online Optimization . . . . .	45
3.4.3	Implementation . . . . .	49
3.5	Experimental Evaluation . . . . .	50
3.5.1	Experimental Protocol . . . . .	51
3.5.2	Results . . . . .	52
3.6	Discussion & Conclusion . . . . .	53
<b>4</b>	<b>An Adaptive Gain Proportional Myoelectric Controller for a Robotic Ankle Exoskeleton . . . . .</b>	<b>56</b>
4.1	Background . . . . .	56
4.2	Methods . . . . .	60
4.2.1	Subjects . . . . .	60
4.2.2	Exoskeleton Hardware . . . . .	61
4.2.3	Exoskeleton Control . . . . .	62
4.2.4	Testing Protocol . . . . .	63
4.2.5	Metabolic Cost . . . . .	63
4.2.6	Electromyography . . . . .	64
4.2.7	Kinematics . . . . .	64
4.2.8	Joint Mechanics . . . . .	65
4.2.9	Exoskeleton Mechanics . . . . .	66
4.2.10	Statistical Analyses . . . . .	66
4.3	Results . . . . .	66
4.3.1	Metabolic Cost . . . . .	66
4.3.2	Dynamically Adjusted Gain . . . . .	68
4.3.3	Electromyography . . . . .	68
4.3.4	Joint Kinematics . . . . .	69
4.3.5	Joint Mechanics . . . . .	70
4.4	Discussion . . . . .	72
4.5	Conclusion . . . . .	76
<b>5</b>	<b>Biomechanics and Energetics of Walking in Powered Ankle Exoskeletons Using Myoelectric Control versus Mechanically Intrinsic Control . . . . .</b>	<b>77</b>
5.1	Background . . . . .	77
5.2	Methods . . . . .	79
5.2.1	Subjects . . . . .	79
5.2.2	Exoskeleton Hardware . . . . .	80
5.2.3	Exoskeleton Control . . . . .	80
5.2.4	Testing Protocol . . . . .	82
5.2.5	Metabolic Cost . . . . .	83

5.2.6	Electromyography . . . . .	83
5.2.7	Kinematics . . . . .	84
5.2.8	Joint Mechanics . . . . .	85
5.2.9	Exoskeleton Mechanics . . . . .	85
5.2.10	Statistical Analyses . . . . .	86
5.3	Results . . . . .	86
5.3.1	Metabolic Work Rate . . . . .	86
5.3.2	Electromyography . . . . .	87
5.3.3	Gait Kinematics . . . . .	89
5.3.4	Joint Kinematics . . . . .	89
5.3.5	Joint Kinetics . . . . .	90
5.4	Discussion . . . . .	93
5.5	Conclusion . . . . .	97
<b>6</b>	<b>Discussion and Conclusion . . . . .</b>	<b>98</b>
6.1	Discussion of Contributions . . . . .	98
6.2	Limitations and Need for Future Research . . . . .	101
6.3	Concluding Remarks . . . . .	102
	<b>Bibliography . . . . .</b>	<b>104</b>

## LIST OF FIGURES

2.1	Proposed human subject testing to validate confidence in the curve techniques .	13
2.2	Modeling the human metabolic system as a discrete, time-delayed first order system . . . . .	18
2.3	Example of how the covariance matrix affects the confidence analysis . . . . .	23
2.4	Exoskeleton controller used for experimental validation of confidence analyses	24
2.5	Exploration and analysis protocols used in experimental validation of confidence analyses . . . . .	26
2.6	Experimental results comparing parameter explorations and analyses against one another . . . . .	29
2.7	Comparing a step exploration with a SSCM analysis to a step exploration with an ICM analysis for a single representative subject . . . . .	30
2.8	Comparing a step exploration with a SSCM analysis to a ramp exploration with an ICM analysis for a single representative subject . . . . .	31
3.1	An example of the generalized approach to the Body-in-the-Loop optimization of assistive robotic devices . . . . .	37
3.2	Proposed experiment for Body-in-the-Loop optimization of bilateral robotic ankle exoskeletons . . . . .	39
3.3	Experimental setup for Body-in-the-Loop optimization of bilateral robotic ankle exoskeletons . . . . .	40
3.4	Controller to be optimized during the Body-in-the-Loop optimization . . . . .	41
3.5	Establishing a ground truth cost landscape to compare the optimized results to .	44
3.6	Fitting subject specific $\tau$ values . . . . .	51
3.7	A single representative subject's optimization trial with the gradient descent algorithm . . . . .	52
4.1	Graphical representation of total ankle activity contributions with a proportional myoelectric controller . . . . .	58
4.2	Testing protocol and the adaptive proportional myoelectric controller . . . . .	61
4.3	Metabolic results from each training session . . . . .	67
4.4	Soelus and rectus femoris results from each training session . . . . .	69
4.5	Joint kinematics, dynamics, and power from the beginning and end of training	70
4.6	A breakdown of ankle power contributions from each training session . . . . .	71
4.7	A breakdown of knee and hip power contributions from each training session .	73
4.8	Total positive power contributions from each joint . . . . .	74

5.1	Control algorithms used in testing and the experimental setup . . . . .	78
5.2	Creating the timing-based control signal for a representative subject . . . . .	81
5.3	Net metabolic work rate for each tested walking condition . . . . .	86
5.4	Soleus and rectus femoris EMG results from each walking condition . . . . .	87
5.5	Joint kinematics, dynamics, and power from each walking condition . . . . .	90
5.6	A breakdown of ankle power contributions from each walking condition . . . .	91
5.7	A breakdown of knee and hip power contributions from each walking condition	93

## LIST OF TABLES

3.1	Variables used in the Body-in-the-Loop optimization . . . . .	50
3.2	Average results from the Body-in-the-Loop optimization . . . . .	53
4.1	Average residual values after final run of the RRA in OpenSim . . . . .	65
4.2	Resulting net metabolic cost from each time interval across sessions . . . . .	66
5.1	Average residual values after final run of the RRA in OpenSim . . . . .	85
5.2	Resulting mean gait kinematics of each walking bout . . . . .	88
5.3	Resulting gait kinematic variability of each walking bout . . . . .	89

## **ABSTRACT**

Lower extremity assistive robotic devices, such as exoskeletons and prostheses, have the potential to improve mobility for millions of individuals, both healthy and disabled. These devices are designed to work in conjunction with the user to enhance or replace lost functionality of a limb. Given the large variability in walking dynamics from person to person, it is still an open research question of how to optimally control such devices to maximize their benefit for each individual user. In this context, it is becoming more and more evident that there exists no “one size fits all” solution, but that each device needs to be tuned on a subject-specific basis to best account for each user’s unique gait characteristics. However, the controllers that run in the background of these devices to dictate when and what type of actuation to deliver often have up to a hundred different parameters that can be tuned on a subject-specific basis. To hand tune each parameter can be an extremely tedious and time consuming process. Additionally, current tuning practices often rely on subjective measures to inform the fitting process.

To address the current obstacles associated with device control and tuning, I have developed novel tools that overcome some of these issues through the design of control architectures that autonomously adapt to the user based upon real-time physiological measures. This approach frames the tuning process of a device as a real-time optimization and allows for the device to co-adapt with the wearer during use. As an outcome of these approaches, I have been able to investigate what qualities of a device controller are beneficial to users through the analysis of whole body kinematics, dynamics, and energetics.

The framework of my research has been broken down into four major projects. First, I investigated how current standards of processing and analyzing physiological measures

could be improved upon. Specifically, I focused on how to analyze non-steady-state measures of metabolic work rate in real time and how the noise content of these measures can inform confidence analyses. Second, I applied the techniques I developed for analyzing non-steady-state measures of metabolic work rate to conduct a real-time optimization of powered bilateral ankle exoskeletons. For this study I employed a gradient descent optimization to tune and optimize an actuation timing parameter of these simple exoskeletons on a subject-specific basis. Third, I investigated how users may use an adaptive controller where they had a more direct impact on the adaptation via their own muscle recruitment. In this study, I designed and tested an adaptive gain proportional myoelectric controller with healthy subjects walking in bilateral ankle exoskeletons. Through this work I showed that subjects adapted to using increased levels of total ankle power compared to unpowered walking in the devices. As a result, subjects decreased power at their hip and were able to achieve large decreases in their metabolic work rate compared to unpowered walking. Fourth, I compared how subjects may use a controller driven by neural signals differently than one driven by mechanically intrinsic signals. The results of this project suggest that control based on neural signals may be better suited for therapeutic rehabilitation than control based on mechanically intrinsic signals. Together, these four projects have drastically improved upon subject-specific control of assistive devices in both a research and clinical setting.

# CHAPTER 1

## The Control of Assistive Robotic Devices

### 1.1 Motivation and Identifying a Need for Research

There is an ever growing population of people that struggle with daily locomotion due to neurological impairment or amputation [57,99]. These disabilities may be a result of stroke, trauma, diabetes, spinal cord injury, or neurological disease and degradation. Regardless of the cause of debilitation, much of this population is putting forth more effort to move than their healthy counterparts. For example, people with stroke (hemiplegia) exhibit large asymmetries in their gait due to resulting impairments, such as drop foot, that can result in a 5%-29% increase in their metabolic work rate during walking compared to healthy controls [149]. Additionally, people with transtibial amputation lack the ability to supply any positive work at the ankle resulting in a 10%-30% increase in their metabolic work rate during walking as compared to healthy individuals [72, 137]. These disabled populations could greatly benefit from assistive robotic devices, such as exoskeletons or prosthesis, to either aid in their rehabilitation or replace lost functionality [26,35].

Lower extremity assistive robotic devices are mechanical structures designed to be worn by and work in conjunction with the user during locomotion. In doing so, these devices perform positive work on the user to aid with walking or running. The success of such devices is commonly evaluated using a number of physiological measurements such as gait kinematics, joint dynamics, gait symmetry, muscle activity, and/or energetic consumption [147]. Theoretically, the synergy between the device and the user has the potential to make it easier for the user to move [78,132]. As such, we would expect a well designed device to offload some of the energy needed from the user to ambulate. This offloading could result in a reduction in the user's metabolic work rate as an outcome of other biomechanical changes. Nonetheless, it is still an open research question as to how to best supply assistance to the user and what the biomechanical implications are of using these devices.

Early work in the field of rehabilitation robotics proved that assistive devices could pos-

itively affect users' locomotion [7, 32, 66, 116]; however, there were many failed attempts made along the way [62, 134, 136, 138]. These early studies have illustrated just how sensitive the performance outcomes of a device are to the overall design. From a hardware perspective, the device weight or kinematic constraints imposed on the user can result in large increases in a wearer's metabolic work rate making it more difficult to move [21, 109, 131]. However, hardware is not the only aspect to consider in device design. Software can also play a big role in performance outcomes. From a software perspective, if a device is not controlled properly it can also result in large increases in a wearer's metabolic work rate as the device can potentially be fighting movement rather than aiding in it [77].

Recent work has shown that users' physiological measures are highly sensitive to the software tuning of a device's control parameters. Control parameters are scalar values in the control architecture, such as gains or thresholds, that dictate aspects of a device's actuation. These control parameters may correspond to actuation characteristics such as virtual impedance, peak power output, or timing. Differences in such actuation characteristics can have large effects on the biomechanics and energetics of the wearer. Malcolm et al. was one of the first to show that systematically varying a control parameter can have a drastic effect on a physiological measure, in this case metabolic work rate [101]. In their work, Malcolm et al. varied the actuation onset timing of bilateral ankle exoskeletons that aided with push off during the stance phase of walking. One could imagine that if the timing of such actuation occurred too early in the stance phase, the actuation may do negative work on the body as it tries to push the center of mass backwards. If the timing were to occur too late in the stance phase, the actuation may do negligible positive work on the body. The results of this parameter study showed that there existed an optimal timing that resulted in the largest reduction in metabolic work rate. Similar studies have been conducted where other parameters that dictate timing, torque, work, power, or virtual stiffness of a device's actuation have been varied to identify what may be the best tuning for different controllers [28, 33, 37, 49, 77]. These studies primarily serve as evaluations of different devices and as basic science studies to investigate how the human body adapts and responds to different forms of assistance. To tune a device for real-world use by this type of brute force parameter exploration would be extremely time consuming and impractical for multidimensional parameter spaces.

The aforementioned studies have presented resulting favorable parameter configurations as global best solutions across subjects; however, more recent research has shown that there is a large benefit to subject-specific parameter configurations. For example, Quesada et al. conducted a parameter study where they varied the amount of push off work done by a powered prosthetic for six different amputee subjects [110]. Their results show that

when considering metabolic work rate on a subject-by-subject basis, the optimal amount of push off work varied drastically for each user. It seems logical that each individual user may need unique parameter configurations given that there exists large amounts of anthropometric and gait variability from person-to-person which would result in each individual using the device somewhat differently [58,142]. The idea of subject-specific tunings of device parameters is not a new concept; however, it is only recently being objectively quantified.

The notion of a subject-specific tuning of device parameters has long been acknowledged during clinical fittings of these devices; yet, the tuning process in a clinic is quite subjective. For a device tuning, a clinician will often custom tune parameters for an individual patient while the patient walks around the clinic. During these walking bouts the clinician is using visual cues of the patient's gait, verbal feedback from the patient, and some measured feedback from sensors on the device in order to identify what they think is the best parameter configuration [55, 114, 124]. Tuning these devices is a lengthy process that is largely heuristic and can vary from clinician to clinician due to the subjective nature of the tuning process. Given that these devices can have dozens of control parameters to tune, it becomes exceedingly complicated and time consuming to fit devices on a subject-specific basis [14,93]. This high dimensional parameter space also makes for a systematic evaluation of each parameter setting nearly impossible. Additionally, users will adapt their gait over time to the added assistance provided by the device [52,59, 116]. This user adaptation makes the ideal parameter configuration a moving target since it changes over time as the wearer better learns to use the device.

***The Challenge:*** Currently there is a large gap between how assistive devices are tuned in a clinic setting and how they are evaluated in a research setting. Clinical tunings are relying on a heuristic and subjective approach to tuning while in a research setting these same types of devices are evaluated using objective measures. Both of these means of tuning and evaluation are highly iterative processes which can be extremely time consuming and often inaccurate over long periods of time due to user adaptations. There is a clear need for more rigorous and objective tuning methods that can also account for the adaptation of the user.

***The Solution:*** Device tunings need to be objectively informed in the same manner in which their success is evaluated. Previous research that suggest optimal tunings based upon evaluation metrics have framed the tuning process as a form of parameter study; however, this framework breaks down as the parameter space grows in dimensionality. Alternatively, our research group has begun to frame this tuning problem in the context of an optimization problem. By framing the tuning of such devices in this manner, the mathematical relationship between a physiological measure and device parameter settings

can be thought of as a type of *cost landscape*. These cost landscapes are unique to each individual user due to distinct gait characteristics and can potentially change over time with user adaptations. In the work presented here, I am proposing to automate the tuning process such that control parameters are optimized in *real-time* based upon physiological measures of the user. This gives rise to a future realm of assistive device control where the controllers themselves autonomously adapt to individual users as users adapt to the devices themselves.

This solution of online adaptation brings the human body into the iterative tuning and evaluation loop and allows for a controller design to be based upon objective physiological measurements taken directly from the user during use. In doing so, a device can be optimally tuned for any user across a number of tasks that the wearer encounters on a daily basis. This ‘Body-in-the-Loop’ approach to tuning and optimizing device control allows for a subject-specific fit of devices and allows for the adaptation of control to individual users and scenarios.

## 1.2 State of the Art

In the following subsections I have introduced the background to a few select topics and discussed some of the current research revolving around each. A more in depth background on some of these topics are presented in the introductory sections of subsequent chapters.

### Assistive Robotic Devices

There are a wide variety of lower extremity assistive robotic devices used in both a research and clinical environment [140, 147]. These devices often rely on electromechanical actuation to supply positive work to the wearer during motion. In the area of prostheses, there are devices targeted toward transtibial (below the knee) amputees [6, 11, 74, 123] as well as devices targeted toward transfemoral (above the knee) amputees [56, 93, 112, 153]. In the area of exoskeletons, there are devices that target assisting at the ankle [106], knee [122], or hip [120] as well as any combination of the three [82, 111]. Additionally, there are a host of many other devices and advancements that would be too numerous to describe here [130, 146].

For the purposes of this dissertation I would like to emphasize that regardless of the assistive device or its applications, all assistive robotic devices rely on an underlying control architecture that determines when and how much power to supply to the user. In each of these control architectures there are a number of different control parameters that physically

shape the actuation that the user receives. Each of these parameters must be tuned for each individual user. Although in the subsequent chapters of this dissertation I will be using ankle exoskeletons as a testing platform to experimentally validate developed methods, the presented techniques could be applied to any assistive robotic device as all require control parameters to be tuned.

## Measures of Metabolic Work Rate

Control parameters of assistive robotic devices can have a large influence on a number of physiological outcome measures [28, 37, 101, 102, 110, 138]. In order to operate in an optimal way, these control parameters must be tuned on a subject-specific basis and these physiological measures are used to inform these tunings. Most commonly, metabolic work rate is the physiological measure used in a research setting to evaluate device performance and identify optimal tuning parameters. Our field's current standard for identifying the optimal parameter configuration of a device is to measure user's metabolic work rate to estimate the user's metabolic cost landscape. From this landscape, the optimal parameter configuration is simply identified as the parameter configuration that minimizes the metabolic work rate.

Estimating a metabolic cost landscape is currently done by measuring users' respiratory gas exchange during a brute force parameter exploration. To this end, users walk in a device with a given parameter configuration until measured metabolic work rate reaches a steady state. This can take multiple minutes due to inherent sensor dynamics associated with respiratory measurements [139]. These dynamics are the result of a time delay between instantaneous energetic demand by the body and oxygen consumption measured at the mouth. Once a steady state is reached, a few minutes of metabolic data are collected for analysis. Such long data collections are required since measurements of oxygen uptake and carbon dioxide output are inherently noisy, having a signal to noise ratio of approximately 4, and are sparsely sampled, having a sample rate of approximately 0.32 Hz [18, 91, 139]. Researchers repeat this collection process for each parameter configuration across the parameter space of interest, average the steady-state breath measurements, and fit a curve to these averaged data points. This curve describes the subjects' metabolic cost landscape.

This type of brute force parameter exploration used to identify a metabolic cost landscape can be quite time consuming. Unfortunately, most of this time is spent waiting for measures of metabolic work rate to reach a steady state. Research by Selinger et al. has targeted this pitfall by developing a simple first order model for the metabolic system [118]. In doing so, Selinger et al. has developed a means of estimating the instantaneous energetic demand of the body from non-steady-state measures of metabolic work rate. Previous

work done by our research group in collaboration with Selinger et al. has built upon this work and shown how such techniques could be used to rapidly identify a metabolic cost landscape [43]. Further background on this topic and an extension of this work is presented in Chapter 2.

## **Parameter Studies**

The standard protocol of conducting parameter studies to identify a cost landscape of a device is deep rooted within the field of experimental biomechanics. A wide variety of experimental biomechanics studies aim to estimate metabolic cost landscapes as a function of biomechanical manipulations. For example, studies have looked at the effects of walking speed, walking incline, step frequency, step width, or step height on metabolic work rate [39, 40, 63, 104, 133, 145, 150]. These types of studies are analogous to evaluating and tuning the parameters on an assistive robotic device in that the biomechanical manipulations being enforced can be thought of as the parameters of interest. However, these biomechanics studies are specifically looking to characterize the metabolic cost landscape and not necessarily identify optimal gait parameter configurations to implement for every-day locomotion. Given that there is no need for optimal biomechanical manipulation parameters to be identified in real time, there is no major draw back to having long time requirements for identifying the the cost landscape.

As assistive devices are becoming more complex and require multiple parameters to tune, these brute force mapping protocols are becoming inefficient and impractical. The time required to experimentally map a cost landscape grows exponentially with parameter dimensionality. Galle et al. has presented work where a two dimensional space was explored using this parameter study type of methodology and the study required subjects to walk in 12 different powered conditions for a total walking time of 48 minutes [49]. This time requirement is within the realm of feasible walking time before fatigue sets in; however, given that more complex devices, such as the BiOM [14] or the Vanderbilt Leg [93], have anywhere from 11 to 140 tuning parameters, these types of studies become impossible to conduct. As such, the realm of tuning assistive robotic devices needs to begin to move away from this type of brute force parameter exploration.

## **Current Tuning Practices for Complex Controllers**

As discussed in the introduction to this chapter, tuning device controllers is a highly iterative and subjective process. Take for example the tuning process described by Rouse et al. for a powered knee prosthesis [114]. Rouse et al. described the tuning process to consist of

iterative walking bouts where tuning parameters were selected based upon three different criteria:

1. A comparison of kinematic and kinetic profiles to those observed from standardized biological datasets
2. Clinical input from a prosthetist
3. The level of comfort of the patient

In conducting this tuning, participants were asked to walk for approximately one minute with the device powered in a given parameter configuration. After that walking bout, parameters were changed based upon the criteria above and then participants walked with the device again. This process was repeated for 6-8 iterations per participant before the device was configured in an acceptable tuning. The process described by Rouse et al. was a relatively fast tuning process despite having 15 different parameters to tune; however, some devices can have upwards of 100 parameters to consider.

One method for speeding up the tuning of a device with a very large number of parameters is to project the parameter space into a smaller dimensional space for tuning as described by Simon et al. [124]. In this work, Simon et al. began by describing the challenges associated with tuning parameter configurations for a powered knee and ankle prosthesis for transfemoral amputees, specifically the Vanderbilt Leg [127]. This prosthesis used an impedance based controller for both the ankle and knee actuation with 5 different ambulation modes (level-ground walking, ramp ascent/descent, and stair ascent/descent) where each ambulation mode was broken into four separate finite states. Given this control break down, the Vanderbilt Leg had a possible 140 control parameters to tune on a subject-specific basis. Simon et al. developed a means to lower the dimensionality of this tuning space by coupling parameters and establishing a standardized set of parameter configurations for subjects to begin from. Subjects in this study walked through a series of ambulation tasks while a clinician tuned the lower dimensional space of parameters accordingly. The tuning of these parameters was based upon a combination of visual inspection of kinematics by the clinician and user feedback. In testing with 6 subjects (3 experienced, 3 novice), they found that their methods allowed for adequate tuning of the device by only changing collectively 21 and 24 parameters for the experienced and novice users, respectively. The time required to tune the device was 2.5-5 hours depending on the subject. Through this work, Simon et al. were able to show that their techniques could drastically reduce the number of parameters needed to be tuned by a clinician fitting a subject with such a complex device. Although this was not an autonomous tuning, this study represents an important step in improving the tuning time for an extremely complex device.

Another means of feedback guided tuning was presented by Caputo et al. [27]. In this study, researchers attempted to simultaneously tune three separate parameters of a tethered powered ankle prosthetic by explicitly using only user feedback. The controller of interest simulated spring like behavior (net-zero work) and the tuning parameters were resting angle, stiffness, and shape (stiffening or softening) of the virtual spring [29]. In this study, an experimenter would begin subjects at a randomized parameter configuration and then deviate one of the three parameter configurations in a randomized direction until the subject reported a decrease in satisfaction. The experimenter would then reverse directions until the subject again reported a decrease in satisfaction. This process was repeated for a total of three reversals. The best parameter configuration for this deviation task was taken to be the mean of the midpoints of the final reversals in each direction. This process was then repeated for the next parameter setting and done in total three times for each parameter. This methodology created a hill climb optimization routine that zeroed in on a parameter configuration that optimized for user satisfaction [115]. The only publication to date on this work shows preliminary findings from a small sample size of 3 transtibial amputees [27]; however, the presented results are quite intriguing. Caputo et al. showed that although there was no large difference in metabolic work rate of the optimized tethered prosthesis compared to subjects' prescribed prosthesis, subjects showed an average decrease in net heart rate, an increase in maximum walking speed, and an increase in user satisfaction scores with the optimized prosthesis compared to their prescribed prosthesis. This study is a great example of alternative cost landscapes that can be used to tune a device and how a form of optimization can be used to direct a multidimensional tuning. It is worth noting that this optimization routine was based purely on subjective information provided by the user and was not autonomously driven.

## **Autonomous Tuning of Devices**

Research conducted by Huang et al. demonstrates an early example of an autonomous tuning strategy that is based upon objective gait measurements taken from the device during walking [73]. Although these are objective measurements, the adaptive tuning of this work was based upon subjective decisions and control laws. Huang has coined this type of tuning as a *cyber expert* tuning. For this study, researchers tuned a impedance based controller for a powered knee-passive ankle prosthesis [98]. Given 3 tuning parameters (virtual spring stiffness, resting angle, and damping coefficient) with 5 discrete states of the stride cycle, a total of 15 parameters needed to be tuned. Two able bodied subjects using a bypass and one amputee subject were first tuned in the device by a human expert. The cyber

expert was then designed using fuzzy logic control with a number of logic rules (IF-THEN statements) developed by means of observing the human expert tuning. These logic rules were based upon objective measures of peak knee angle, gait phase duration, and peak knee angular velocity; however, the action of the logic rules were based upon observed subjective opinions of the human expert tuning. Once designed, the cyber expert was tested by tuning the device for the three subjects in which it was designed around along with one new subject (amputee) to test its performance on a naive subject. Results showed that the cyber expert tuning was able to tune the device toward normal gait kinematics in about half the time of that required by the human expert it was designed around ( $\sim 188$  versus  $\sim 96$  strides) and without any human intervention. This type of tuning approach can potentially allow for autonomous and more objective tunings that can be performed outside of the clinic setting on a more frequent basis for the user.

Similar to Huang et al.'s work, work by Spanias et al. has shown that autonomous tuning based upon objective mechanical measurements is also possible using a machine learning approach [125]. Although in this work pattern recognition for the discrete change in ambulation modes of a device was the targeted tuning, one could imagine this can also be applied towards the tuning of continuous control parameters much like that in Huang et al.'s work. The benefit of Spanias et al.'s approach over Huang et al.'s is that control laws do not need to be explicitly identified by the designer which can be a very time consuming process and relies on an expert's opinion which can be subjective from one expert to another. Additionally, a machine learning approach can potentially identify tuning laws that would be unintuitive for a researcher to identify [15]. Given enough data to train on, a machine learning approach should identify tunings completely autonomously based upon objective measures.

### **1.3 Contributions**

In all of the presented state of the art literature, all tuning approaches were based upon mechanical measurements taken directly from the device or subjective user feedback. However, these devices are often analyzed and evaluated using physiological measures taken directly from the user. Currently, there is a large disconnect between state of the art tuning approaches and evaluation approaches. This dissertation aims to bridge this gap by basing all tunings upon objective physiological measures. To the best of my knowledge, the work of this dissertation serves as the first real-time tuning and adaptation of an assistive device based upon an objective physiological measure.

The content of this dissertation is broken into four major chapters. In Chapter 2, I have

discussed methods that improve upon the current standards of processing and analyzing metabolic work rate data. In this work, I have developed a generalized analysis of non-steady-state measures of metabolic work rate. This approach preserves the noise content of the energetic measures and allows for novel confidence analyses of identified cost landscapes. Additionally, I have experimentally tested these techniques and have rigorously proven their feasibility. In doing so, I have also compared them to current standard practices in the field. In Chapter 3, I applied the techniques presented in Chapter 2 to conduct a real-time optimization of powered bilateral ankle exoskeletons. For this work I used a gradient descent optimization to optimize an actuation timing parameter of these simple exoskeletons on a subject-specific basis. This was the first ever example of an online optimization of an assistive robotic device driven by measures of metabolic work rate. In Chapter 4, I have investigated how users may use and adapt to using an adaptive controller where they have a more direct impact on the adaptation of the device. In this study, I designed an adaptive gain proportional myoelectric controller and tested it with healthy subjects walking in bilateral ankle exoskeletons. The controller itself adapted to maintain maximal power output regardless of users' muscle recruitment allowing the wearers own nervous system to adapt to how it would like to use the device. Results from this work showed that users adapted to joint mechanics that were not biologically feasible without the added assistance. These results suggest that designing controllers to mimic healthy biomechanics may not be the best approach to controller design as users seem to adapt to abnormal joint dynamics when given the freedom to do so. Lastly, in Chapter 5 I have compared how subjects may use a controller driven by neural signals differently than one driven by mechanically intrinsic signals. Given that I have presented two different adaptive controllers in the previous chapters, one driven by mechanically intrinsic signals and the other by neural signals, it is an interesting question to ask that if each were to adapt to the same actuation signal, would subjects use each controller differently? The results of this project suggest that control based on neural signals may be better suited for therapeutic rehabilitation than control based on mechanically intrinsic signals due to different levels of slacking by the users.

As a whole, the collection of work presented in these four chapters has drastically improved upon subject-specific control of assistive devices. These improvements have been made through contributions in novel adaptive controllers and rigorous analysis of how users adapt to using them. It is my hope that this work will lay foundation for many future advancements and studies to come.

## CHAPTER 2

# Confidence in the Curve: Establishing Instantaneous Cost Mapping Techniques using Bilateral Ankle Exoskeletons

### 2.1 Introduction

There are many ways to evaluate lower extremity assistive robotic devices. Most commonly, the field relies on measures of metabolic power to assess device performance [38, 106, 147]. Since these devices are designed to aid in locomotion, we would expect a reduction in users' metabolic power when walking in them. Until a few years ago, the evaluation of assistive robotic devices was limited to merely determining if a reduction in metabolic power was achieved or not [7, 32, 66, 116, 136]. However, more recently, the field has started to investigate in detail the quantitative relationships between various device control parameters and the users' metabolic power. In the context of lower extremity assistive devices, these control parameters may define things such as actuation timing, torque and power output, or virtual stiffness and damping of a device [77, 92, 108]. In current devices, more than a dozen parameters may exist and must be tuned on a subject-by-subject basis for a variety of different tasks [14, 93]. This tuning is important, since the performance of many devices is sensitive to these parameter configurations. In many cases, there exists an optimal configuration that results in the largest reduction in metabolic power. These devices can result in a 10-26% reduction in metabolic power when optimally tuned compared to their unpowered configurations [28, 51, 77, 101, 102, 108]. We refer to the functional relationship between the device parameters and the associated metabolic power as the *metabolic cost landscape*. As subject-specific parameter tuning is becoming increasingly relevant, systematic methods to quickly and accurately identify metabolic cost landscapes are becoming more and

---

The content of this chapter has been previously published in the Journal of Applied Physiology [88].

more important.

Our field’s current standard to identify a metabolic cost landscape is to measure users’ respiratory gas exchange during a brute force parameter exploration. To this end, users walk in a device with a given parameter configuration until measured metabolic power reaches a steady state. This can take multiple minutes due to inherent sensor dynamics associated with respiratory measurements [139]. These dynamics are the result of a time delay between instantaneous energetic demand by the body and oxygen consumption measured at the mouth. Once a steady state is reached, a few minutes of metabolic data are collected for analysis. Such long data collections are required since measurements of oxygen uptake and carbon dioxide output are inherently noisy, having a signal to noise ratio of approximately 4, and are sparsely sampled, having a sample rate of approximately 0.32 Hz [18, 91, 139]. Researchers repeat this collection process for each parameter configuration across the parameter space of interest, average the steady-state breath measurements, and fit a curve to the averaged data points. This curve describes the subjects’ metabolic cost landscape.

There are a number of limitations to this standard practice. First, a brute force exploration that relies on steady-state measures can be time consuming and taxing on both the subject and the researcher or clinician, especially when the parameter space is multidimensional [14, 51, 93]. A lengthy time requirement on device tuning and evaluation can also be problematic when clinical populations, such as people post-stroke or with amputation, are the end users. Many of these clinical users might not have the ability or strength to walk for the long intervals required to conduct this type of parameter exploration. Additionally, all information about inter-breath variability is lost when data is averaged during post-processing. This can lead to a false sense of accuracy in the measurements and curve fits.

We refer to this standard practice of using only steady-state measurements in estimating a cost landscape as a *steady-state cost mapping* analysis. In recent years, researchers have started to work on viable alternatives to this steady-state cost mapping analysis [118]. In our own work, we proposed an *instantaneous cost mapping* analysis that takes into account the sensor dynamics of the metabolic system when post-processing data [43]. This enables the use of all breath measurements, including those recorded not at a steady state, to estimate the metabolic cost landscape. In doing so, the instantaneous cost mapping analysis allows for a more rapid parameter exploration to back out an estimate of the metabolic cost landscape.

In this paper we present methodology for subject-specific metabolic cost landscape confidence analyses. These techniques calculate a confidence band on estimated landscapes and a probability distribution of where the minimizing parameter configuration may lie on

a subject-specific basis. These methods allow for a rigorous comparison of mapping protocols among one another and display how subject-specific measurement noise can affect a given fit. To verify these methods, we applied them to estimating subject-specific metabolic cost landscapes as a function of actuation onset for bilateral ankle exoskeletons (Fig. 2.1). We tested 9 healthy subjects in the exoskeletons using a step and a ramp parameter exploration of the devices' actuation onset. We analyzed both of these explorations using an instantaneous cost mapping analysis and compared the results to the current standard in the field, a step exploration with a steady-state cost mapping analysis. These comparisons clearly illustrate the trade offs associated with different parameter exploration protocols and mapping analyses, comparisons only made possible by the presented confidence techniques.

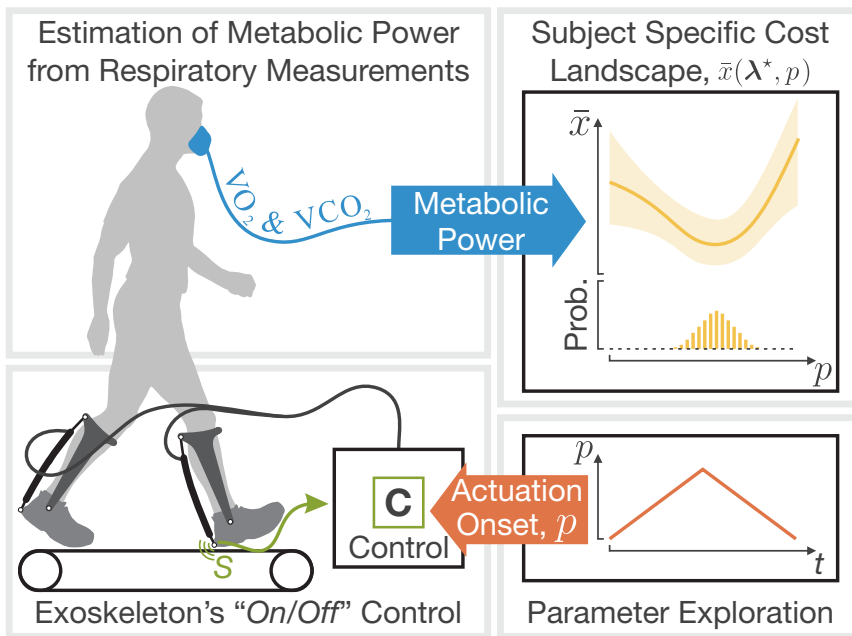


**Figure 2.1: Proposed human subject testing to validate confidence in the curve techniques.** Here we are presenting a generalized instantaneous cost mapping analysis and novel metabolic cost landscape confidence analyses. We verified these techniques using bilateral ankle exoskeletons where we estimated subject-specific metabolic cost landscapes as a function of the exoskeletons' actuation onset timing. We tested a step and ramp parameter exploration and analyzed each using an instantaneous cost mapping analysis. These results were compared to a step exploration with a steady-state cost mapping analysis, the current standard in the field.

## 2.2 Methods

### 2.2.1 Mapping of a Metabolic Cost Landscape

The goal of any metabolic cost mapping protocol is to extract an estimate of the body's metabolic demand,  $x$ , as a function of the device control parameters,  $\mathbf{p}$ . Mathematically, we denote this metabolic cost landscape as  $x(\mathbf{p})$ .  $x$  is also known as the *instantaneous energetic cost* [118]. It is established practice in the field of assistive robotic devices to use linear combinations of basis functions to describe  $x(\mathbf{p})$ . For example, linear combinations of monomials are commonly used to describe  $x(\mathbf{p})$  as a polynomial function [28, 33, 101, 119]. Using a linear combination of basis functions is a deliberate choice to simplify the metabolic cost landscape and thus form a more tractable problem. Although linear with respect to the chosen basis functions, these curves can still be highly nonlinear given the choice of basis functions used.

### 2.2.2 Representing an Estimate of the Metabolic Cost Landscape

Any fitted curve that is linear with respect to a set of basis functions can be expressed as

$$\bar{x}(\boldsymbol{\lambda}, \mathbf{p}) = \sum_{j=1}^m g(\mathbf{p})_j \lambda_j = \mathbf{g}(\mathbf{p})^\top \boldsymbol{\lambda}, \quad (2.1)$$

where  $\bar{x}(\boldsymbol{\lambda}, \mathbf{p})$  represents the functional estimate of the true underlying metabolic cost landscape  $x(\mathbf{p})$ . In this representation,  $\boldsymbol{\lambda}$  is a  $m \times 1$  vector of scalar coefficients and  $\mathbf{g}(\mathbf{p})$  is a  $m \times 1$  vector of basis functions evaluated at  $\mathbf{p}$ .  $g(\mathbf{p})_j$  and  $\lambda_j$  are simply the  $j^{\text{th}}$  elements of the vectors  $\mathbf{g}(\mathbf{p})$  and  $\boldsymbol{\lambda}$ , respectively.

Consider, for example, a second order polynomial curve with a single parameter,  $\mathbf{p} = p$ :

$$\bar{x}(\boldsymbol{\lambda}, \mathbf{p}) = \lambda_1 + \lambda_2 p + \lambda_3 p^2. \quad (2.2)$$

We can describe the above in the format of Eq. (2.1) such that the vector of basis functions,  $\mathbf{g}(\mathbf{p})$ , is defined as

$$\begin{aligned} \mathbf{g}(\mathbf{p}) &= [g(\mathbf{p})_1, g(\mathbf{p})_2, g(\mathbf{p})_3]^\top \\ &= [1, p, p^2]^\top. \end{aligned} \quad (2.3)$$

Similarly, a second order polynomial curve with two parameters,  $\mathbf{p} = [p_1, p_2]$

$$\bar{x}(\boldsymbol{\lambda}, \mathbf{p}) = \lambda_1 + \lambda_2 p_1 + \lambda_3 p_2 + \lambda_4 p_1 p_2 + \lambda_5 p_1^2 + \lambda_6 p_2^2, \quad (2.4)$$

is defined via the vector of basis functions

$$\begin{aligned} \mathbf{g}(\mathbf{p}) &= [g(\mathbf{p})_1, g(\mathbf{p})_2, g(\mathbf{p})_3, g(\mathbf{p})_4, g(\mathbf{p})_5, g(\mathbf{p})_6]^\top \\ &= [1, p_1, p_2, p_1 p_2, p_1^2, p_2^2]^\top. \end{aligned} \quad (2.5)$$

By representing curve fitting functions as a linear summation of basis functions, we are able to generalize the following mathematics so that these techniques can be applied to any dimensionality of parameter space or function order. It is worth noting that the choice of basis functions is not constrained to monomials. Other basis functions, such as exponential or trigonometric functions, can also be used. However, in the realm of assistive devices, monomial are the predominant choice [28,33,101,119].

### 2.2.3 Measuring $x(\mathbf{p})$

The metabolic cost landscape,  $x(\mathbf{p})$ , is commonly estimated by measuring oxygen consumption via respiratory measurements of oxygen uptake and carbon dioxide output [19]. These respiratory measurements give us the correct estimate of  $x(\mathbf{p})$  during steady-state activity; however, there are significant sensor dynamics associated with this process that prevent us from measuring  $x(\mathbf{p})$  during non-steady-state activity. These sensor dynamics are due to an inherent time delay between the body’s instantaneous energetic demand and physical respiratory measurements. Muscles generate mechanical work through the breakdown of adenosine triphosphate at the cross bridge level. Replenishment of adenosine triphosphate through oxidative phosphorylation takes longer than anaerobic reactions and depends on red blood cell transport to the muscle. Changes in cardiac output and respiration rates are not instantaneous and create time lags between energy usage and resupply. In addition, respiratory measurements only sample a portion of the air volume within the lung with each breath causing further time delay as content of the total lung volume does not instantaneously reach an equilibrium that reflects the oxygen and carbon dioxide content of the blood. The dynamics of the human metabolic system can be modeled as a first order system with a time constant of approximately 40 seconds during walking. Exact time constant values vary on a subject-specific basis [118].

$$y_i = \left(1 - \frac{h_i}{\tau}\right) y_{i-1} + \frac{h_i}{\tau} x(\mathbf{p}_i). \quad (2.6)$$

In this representation,  $y_i$  is the metabolic power estimated from breath measurement  $i$ ,  $h_i$  is the elapsed time since the previous breath,  $\tau$  is a subject-specific time constant, and  $\mathbf{p}_i$  is the parameter configuration enforced during breath  $i$ .

## 2.2.4 Metabolic Cost Mapping Analyses

In the following sub-sections we have defined the mathematics behind the steady-state cost mapping (SSCM) and instantaneous cost mapping (ICM) analyses using the aforementioned notation of basis functions. We have expressed each analysis in the form of a single matrix equation so we can apply generalized confidence analyses to each as described in the following section.

### 2.2.4.1 Steady-State Cost Mapping Analysis

A SSCM analysis relies solely on steady-state measurements of metabolic power to fit the best  $\bar{x}(\boldsymbol{\lambda}, \mathbf{p})$ . Therefore a SSCM analysis can only be used with a parameter exploration protocol that holds a parameter configuration constant long enough for metabolic measures to stabilize before moving onto another configuration. The best  $\bar{x}(\boldsymbol{\lambda}, \mathbf{p})$  is one that represents steady-state energy consumption with as little error as possible. This is described mathematically as minimizing the sum of squared error between  $\bar{x}(\boldsymbol{\lambda}, \mathbf{p})$  and actual breath measurements,  $\hat{y}_i$ , over  $n$  steady-state breaths,

$$\min_{\boldsymbol{\lambda}} \sum_{i=1}^n (\bar{x}(\boldsymbol{\lambda}, \mathbf{p}_i) - \hat{y}_i)^2. \quad (2.7)$$

We can solve Eq. (2.7) using linear regression techniques. We begin by expanding out Eq. (2.1) into a matrix format where each row is an individual steady-state breath recorded during the parameter exploration

$$\begin{bmatrix} g(\mathbf{p}_1)_1 & g(\mathbf{p}_1)_2 & \cdots & g(\mathbf{p}_1)_m \\ g(\mathbf{p}_2)_1 & g(\mathbf{p}_2)_2 & \cdots & g(\mathbf{p}_2)_m \\ \vdots & \vdots & & \vdots \\ g(\mathbf{p}_n)_1 & g(\mathbf{p}_n)_2 & \cdots & g(\mathbf{p}_n)_m \end{bmatrix} \begin{bmatrix} \lambda_1 \\ \lambda_2 \\ \vdots \\ \lambda_m \end{bmatrix} = \begin{bmatrix} \bar{x}(\boldsymbol{\lambda}, \mathbf{p}_1) \\ \bar{x}(\boldsymbol{\lambda}, \mathbf{p}_2) \\ \vdots \\ \bar{x}(\boldsymbol{\lambda}, \mathbf{p}_n) \end{bmatrix}, \quad (2.8)$$

or simplified to the matrix equation

$$\mathbf{A}_{\text{SSCM}} \boldsymbol{\lambda} = \bar{\mathbf{x}}. \quad (2.9)$$

In this notation,  $\mathbf{A}_{\text{SSCM}}$  is a  $n \times m$  matrix where  $n \geq m$ , and  $\bar{\mathbf{x}}$  is a  $n \times 1$  vector of  $\bar{x}(\boldsymbol{\lambda}, \mathbf{p}_i)$  values for  $i = 1 \dots n$ . By considering all  $\hat{y}_i$  as the  $n \times 1$  vector  $\hat{\mathbf{y}}$ , we can substitute  $\hat{\mathbf{y}}$  and  $\bar{\mathbf{x}}$  into equation Eq. (2.7) to solve for the vector  $\boldsymbol{\lambda}^*$  that minimizes the measurement residuals. This results in

$$\boldsymbol{\lambda}^* = \mathbf{A}_{\text{SSCM}}^+ \hat{\mathbf{y}}, \quad (2.10)$$

where  $\mathbf{A}_{\text{SSCM}}^+$  is the left pseudo-inverse of  $\mathbf{A}_{\text{SSCM}}$  defined as  $\mathbf{A}_{\text{SSCM}}^+ = (\mathbf{A}_{\text{SSCM}}^\top \mathbf{A}_{\text{SSCM}})^{-1} \mathbf{A}_{\text{SSCM}}^\top$ . By definition,  $\boldsymbol{\lambda}^*$  describes the optimal estimate of the cost landscape,  $\bar{x}(\boldsymbol{\lambda}^*, \mathbf{p})$ .

This process is slightly different than the standard in the field in which the steady-state metabolic data are post-processed by averaging breath measurements from each individual  $\mathbf{p}$  configuration prior to fitting a curve to these averaged points. This averaging process eliminates any notion of inter-breath variability; however, including this variability is imperative for establishing curve confidence. The SSCM analysis that we have presented here excludes this averaging step by considering each individual steady-state breath in the fitting of  $\bar{x}(\boldsymbol{\lambda}^*, \mathbf{p})$  and thus includes inter-breath variability in the matrix equation. If each parameter configuration being considered in a SSCM analysis contains the same number of breath measurements, then the standard of averaging the data results in the same  $\bar{x}(\boldsymbol{\lambda}^*, \mathbf{p})$  as considering each individual breath as presented here.

### 2.2.4.2 Instantaneous Cost Mapping Analysis

An ICM analysis takes into consideration the dynamic model of the human metabolic system when estimating a metabolic cost landscape. Therefore an ICM analysis can be used with any continuous parameter exploration protocol without the explicit need of ever reaching steady-state energy consumption [43, 118]. By substituting Eq. (2.1) into Eq. (2.6), we derive a function for estimated individual breaths,  $\bar{y}_i$ , that incorporates the underlying metabolic dynamics,

$$\bar{y}_i = \left(1 - \frac{h_i}{\tau}\right) \bar{y}_{i-1} + \frac{h_i}{\tau} \mathbf{g}(\mathbf{p}_i)^\top \boldsymbol{\lambda}. \quad (2.11)$$

A visual example of this model is shown in Fig. 2.2.

During an ICM analysis, we are seeking an  $\bar{x}(\boldsymbol{\lambda}, \mathbf{p})$  that minimizes the error between the estimate of each measure,  $\bar{y}_i$ , and the actual measure,  $\hat{y}_i$ , across a series of  $n$ , not necessarily steady-state, continuous breaths. This is described mathematically as minimizing the sum of squared error between the estimated and the actual measurements,

$$\min_{\boldsymbol{\lambda}} \sum_{i=1}^n (\bar{y}_i - \hat{y}_i)^2. \quad (2.12)$$

We can solve for Eq. (2.12) by expressing Eq. (2.11) in a matrix notation. If we expand out

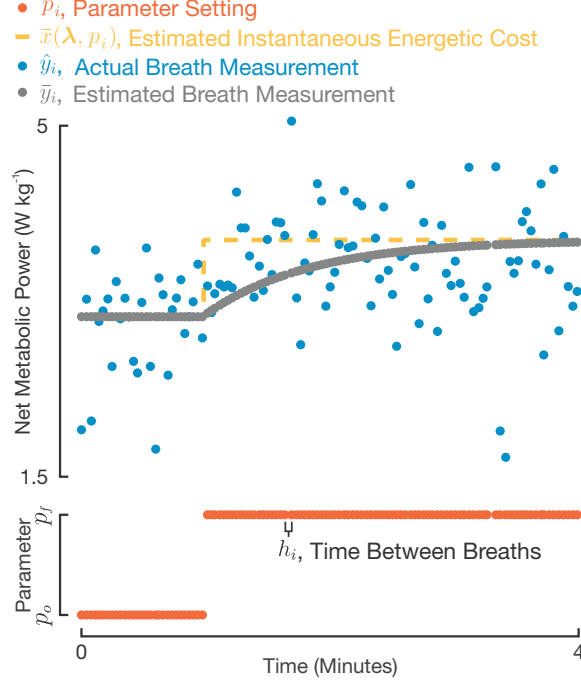


**Figure 2.2: Modeling the human metabolic system as a discrete, time-delayed first order system.** There is an inherent time delay between an instantaneous change in energetic demand by the body and the measured oxygen consumption at the mouth. We have considered these metabolic sensor dynamics as a first order system which allows us to use all recorded breath measures in an instantaneous cost mapping analysis, regardless of whether the measures are at a steady state or not. Here is a representative example of this model given a step change in actuation onset timing for a set of pneumatically powered ankle exoskeletons (change from  $p_o = 0.28$  normalized stride time to  $p_f = 0.58$  normalized stride time). The identified time constant  $\tau$  for this representative subject was 51.9 seconds. These exoskeletons are further described in later sections.

Eq. (2.11) for individual breaths it can be expressed as

$$\mathbf{A}_{\text{ICM}} \begin{bmatrix} \bar{y}_1 \\ \lambda_1 \\ \vdots \\ \lambda_m \end{bmatrix} = \begin{bmatrix} \bar{y}_1 \\ \bar{y}_2 \\ \vdots \\ \bar{y}_n \end{bmatrix}, \quad (2.13)$$

where  $\mathbf{A}_{\text{ICM}}$  is generated recursively as

$$\mathbf{A}_{\text{ICM}_{i,j}} = \begin{cases} 1 & i=1, j=1 \\ 0 & i=1, j>1 \\ \mathbf{A}_{\text{ICM}_{i-1,j}} \left(1 - \frac{h_i}{\tau}\right) & i>1, j=1 \\ \mathbf{A}_{\text{ICM}_{i-1,j}} \left(1 - \frac{h_i}{\tau}\right) + \frac{h_i}{\tau} g(\mathbf{p}_i)_{j-1} & i>1, j>1 \end{cases}. \quad (2.14)$$

Each row of  $\mathbf{A}_{\text{ICM}}$  corresponds to an individual breath estimate based upon previous breaths due to the architecture of Eq. (2.11). In the above notation,  $\mathbf{A}_{\text{ICM}}$  is a  $n \times m + 1$  matrix where  $n \geq m + 1$ . We can express this linear relationship more simply as the matrix equation

$$\mathbf{A}_{\text{ICM}} \begin{bmatrix} \bar{y}_1 \\ \boldsymbol{\lambda} \end{bmatrix} = \bar{\mathbf{y}}, \quad (2.15)$$

where  $\bar{\mathbf{y}}$  is a  $n \times 1$  vector of  $\bar{y}_i$  values for  $i = 1 \dots n$ . We can now solve for the optimal  $\bar{y}_1$  and  $\boldsymbol{\lambda}$  by substituting Eq. (2.15) into Eq. (2.12) and considering all  $\hat{y}_i$  as the  $n \times 1$  vector  $\hat{\mathbf{y}}$ . Solving for the optimum results in

$$\begin{bmatrix} \bar{y}_1^* \\ \boldsymbol{\lambda}^* \end{bmatrix} = \mathbf{A}_{\text{ICM}}^+ \hat{\mathbf{y}}, \quad (2.16)$$

where  $\mathbf{A}_{\text{ICM}}^+$  is the left pseudo-inverse of  $\mathbf{A}_{\text{ICM}}$  defined similarly to  $\mathbf{A}_{\text{SSCM}}^+$ . By definition,  $\boldsymbol{\lambda}^*$  describes the optimal estimate of the underlying cost landscape,  $\bar{x}(\boldsymbol{\lambda}^*, \mathbf{p})$ .

### 2.2.5 Confidence in the Curve

The described cost mapping analyses will always solve for the optimally estimated cost landscape,  $\bar{x}(\boldsymbol{\lambda}^*, \mathbf{p})$ , given the appropriately corresponding experimental data,  $\hat{\mathbf{y}}$ . However, these estimates alone say nothing about how well the optimal fit truly describes the collected data. This makes it difficult to conclude anything about the confidence in a fit or compare mapping analyses to one another. In the following, we present methodology that assesses confidence in the resulting curve of any mapping analysis on a *subject-specific basis* so long as the analysis can be described by a matrix equation that is linear with respect to the estimated underlying basis functions, much like Eq. (2.9) and Eq. (2.15). These methods solve for a confidence band about  $\bar{x}(\boldsymbol{\lambda}^*, \mathbf{p})$  and calculate a probability distribution of where the corresponding minimizing parameter configurations may lie. We first describe the confidence on our optimally estimated breaths and optimal linear coefficients before making the transition to confidence on  $\bar{x}(\boldsymbol{\lambda}^*, \mathbf{p})$  as these are the building blocks to establishing confidence on the fitted curve.

### 2.2.5.1 Confidence in Optimally Estimated Breaths

At the foundation of evaluating curve confidence is the confidence in the individual breath measurements. This is described by a fit's unbiased variance, or  $s^2$  [144]:

$$s^2 = \frac{1}{n-d} \|\hat{\mathbf{y}} - \bar{\mathbf{y}}^*\|_2^2. \quad (2.17)$$

Here,  $d$  represents the degrees of freedom in any given fit. In the context of this paper, the SSCM analysis has  $d = m$  (fitting  $\lambda$ ) while the ICM analysis has  $d = m + 1$  (fitting  $\lambda$  and  $\bar{y}_1$ ). In Eq. (2.17),  $\bar{\mathbf{y}}^*$  represents the optimally estimated breath measurements. These are the estimates that arise from evaluating an analysis' matrix equation using the identified optimal fitting parameters. For example, given a SSCM analysis,  $\bar{\mathbf{y}}^*$  would be the result of substituting the solved for  $\lambda^*$  into Eq. (2.9). Alternatively, for an ICM analysis,  $\bar{\mathbf{y}}^*$  would be the result of substituting the solved for  $\lambda^*$  and  $\bar{y}_1^*$  into Eq. (2.15). By considering the variance in estimated breaths versus real breaths, we are making the implicit assumption that respiratory measurements are characterized by Gaussian white noise. This is an assumption that has previously been established [91]. Because  $s^2$  is a measure of variance between the optimally estimated breaths and the actual recorded breaths, it is intuitive that data with larger noise content will lead to larger variance and thus less confidence in a given fit. Establishing confidence on  $\bar{\mathbf{y}}^*$  is a purely *linear* process since it is based on a linear fit.

### 2.2.5.2 Confidence in $\lambda^*$

Confidence in the optimally fitted linear coefficients,  $\lambda^*$ , is characterized by a covariance matrix,  $\Sigma$ :

$$\Sigma = s^2 \left( \mathbf{C} (\mathbf{A}^\top \mathbf{A})^{-1} \mathbf{C}^\top \right). \quad (2.18)$$

In this equation,  $\mathbf{A}$  is the matrix from a given mapping analysis' matrix equation, such as  $\mathbf{A}_{\text{SSCM}}$  or  $\mathbf{A}_{\text{ICM}}$ , and  $\mathbf{C}$  is a selection matrix used to indicate which fitted variables to consider in the confidence analysis [144]. It should be noted that Eq. (2.18) is dependent upon  $\mathbf{A}$  and  $s^2$ .  $s^2$  is a scalar value that only depends on the inter-breath variability for a given subject while  $\mathbf{A}$  is a matrix whose architecture is highly dependent upon the chosen parameter exploration. Therefore,  $\Sigma$  can be largely characterized based upon the parameter exploration chosen for a given mapping analysis.  $\mathbf{C}$  is only included in Eq. (2.18) so that fitted variables that may not be represented in the optimal curve  $\bar{x}(\lambda^*, \mathbf{p})$  can be omitted from the confidence analyses. In the case of the ICM confidence analysis, we do not wish

to consider  $\bar{y}_1^*$  in the analysis since it is not actually represented in  $\bar{x}(\boldsymbol{\lambda}^*, \mathbf{p})$ . In this scenario

$$\mathbf{C} = \begin{bmatrix} \mathbf{0}_{m \times 1} & \vdots & \mathbf{I}_{m \times m} \end{bmatrix}. \quad (2.19)$$

In the case of the SSCM analysis,  $\mathbf{C}$  is simply a  $m \times m$  identity matrix.

To establish a confidence region on  $\boldsymbol{\lambda}^*$ , we can consider the following [144]:

$$(\boldsymbol{\lambda} - \boldsymbol{\lambda}^*)^\top \mathbf{V} (\boldsymbol{\lambda} - \boldsymbol{\lambda}^*) \leq 1, \quad (2.20)$$

where

$$\mathbf{V} = (\mathcal{F}(M + 1)\boldsymbol{\Sigma})^{-1}. \quad (2.21)$$

In Eq. (2.21),  $\mathcal{F}$  is the F-statistic of the fit given some chosen critical point. For example, to establish a 95% confidence region, a 5% critical point should be used. In calculating  $\mathcal{F}$ , the numerator is defined as the degrees of freedom used in the given fit minus one,  $d - 1$ , while the denominator is defined as the number of data points minus the degrees of freedom used in the given fit,  $n - d$ . Geometrically, Eq. (2.20) can be thought of as a confidence ellipsoid in the  $\boldsymbol{\lambda}$  coordinate space centered about  $\boldsymbol{\lambda}^*$ . Any  $\boldsymbol{\lambda}$  that satisfies Eq. (2.20) is a point that lies within the ellipsoid and thus within the confidence region. The inverse square roots of the eigenvalues of  $\mathbf{V}$  describe the magnitude of the ellipsoid's principal axes and the corresponding eigenvectors describe the ellipsoid's orientation in space. Establishing a confidence region on  $\boldsymbol{\lambda}^*$  is a purely *linear* process.

### 2.2.5.3 A Confidence Band on $\bar{x}(\boldsymbol{\lambda}^*, \mathbf{p})$

From Eq. (2.1) we see that  $\boldsymbol{\lambda}^*$  directly shapes the optimally fitted curve,  $\bar{x}(\boldsymbol{\lambda}^*, \mathbf{p})$ . By establishing a confidence region on  $\boldsymbol{\lambda}^*$ , we have inherently established a confidence region on  $\bar{x}(\boldsymbol{\lambda}^*, \mathbf{p})$ . Despite the fact that the fitted curve can be nonlinear due to the basis functions, the curve is still linear with respect to  $\boldsymbol{\lambda}$  so we can map the confidence region between the two spaces in a purely *linear* fashion. To do so, we must consider the confidence band's upper and lower edges at individual parameter configurations across our parameter space. We will denote an individual query parameter configuration as  $\mathbf{p}^\circ$ . At each  $\mathbf{p}^\circ$  there exists a vector of linear coefficients,  $\boldsymbol{\lambda}^\circ$ , whose corresponding curve touches the upper or lower edge of the confidence band at that specific point. To solve for  $\boldsymbol{\lambda}^\circ$ , consider the following optimization problem:

$$\begin{aligned} & \max_{\boldsymbol{\lambda}^\circ} / \min_{\boldsymbol{\lambda}^\circ} \quad \mathbf{g}(\mathbf{p}^\circ)^\top (\boldsymbol{\lambda}^\circ - \boldsymbol{\lambda}^*) \\ & \text{subject to} \quad (\boldsymbol{\lambda}^\circ - \boldsymbol{\lambda}^*)^\top \mathbf{V} (\boldsymbol{\lambda}^\circ - \boldsymbol{\lambda}^*) \leq 1 \end{aligned} \quad (2.22)$$

This optimization aims to maximize or minimize the difference between  $\bar{x}(\boldsymbol{\lambda}^\circ, \mathbf{p}^\circ)$  and  $\bar{x}(\boldsymbol{\lambda}^*, \mathbf{p}^\circ)$  subject to  $\boldsymbol{\lambda}^\circ$  being within or on the surface of the defined confidence ellipsoid. The analytic solution to this extremal problem statement is

$$\boldsymbol{\lambda}_{max/min}^\circ = \boldsymbol{\lambda}^* \pm \frac{\mathbf{V}^{-1}\mathbf{g}(\mathbf{p}^\circ)}{\sqrt{\mathbf{g}(\mathbf{p}^\circ)^\top \mathbf{V}^{-1}\mathbf{g}(\mathbf{p}^\circ)}} \quad (2.23)$$

where the  $\pm$  accounts for a maximization and minimization of the presented optimization problem, respectively. A proof of this analytic solution is provided in the appendix. Geometrically, this solution is equivalent to establishing a line in the  $\boldsymbol{\lambda}$  coordinate space that points in the the direction of  $\mathbf{V}^{-1}\mathbf{g}(\mathbf{p}^\circ)$  and passes through the origin of the ellipsoid described by  $\mathbf{V}$ . The solutions for  $\boldsymbol{\lambda}_{max/min}^\circ$  are the two points where this line intersects with the ellipsoidal surface. This optimization only gives us a vector  $\boldsymbol{\lambda}^\circ$ ; however, evaluating  $\mathbf{g}(\mathbf{p}^\circ)^\top \boldsymbol{\lambda}^\circ$  will give us an  $\bar{x}$  point at the edge of the confidence band. Repeating this calculation for every  $\mathbf{p}^\circ$  along our parameter space of interest allows us to compute  $\bar{x}$  points that define the edges of the confidence band about  $\bar{x}(\boldsymbol{\lambda}^*, \mathbf{p})$ .

#### 2.2.5.4 Confidence in the Minimizing Parameter Configuration

We commonly estimate a metabolic cost landscape in order to identify the optimal parameter configuration that minimizes metabolic power. We will denote this optimal parameter configuration as  $\mathbf{p}^*$ . The process of mapping from the confidence on  $\bar{x}(\boldsymbol{\lambda}^*, \mathbf{p})$  to a probability distribution of where  $\mathbf{p}^*$  may lie is a *nonlinear* process as the fitted function may have more than one minimum location, a minimum location at negative infinity, or a minimum location that may lie outside of the evaluated parameter space. For this reason, we have developed a Monte Carlo approach to establishing a  $\mathbf{p}^*$ -probability distribution to overcome this nonlinearity.

Given  $\boldsymbol{\lambda}^*$  and  $\Sigma$ , we generate a multivariate random Gaussian distribution of linear coefficient vectors. Each of these randomly generated vectors,  $\boldsymbol{\lambda}$ , are then evaluated with Eq. (2.20) to see if they lie in the confidence region of  $\boldsymbol{\lambda}^*$ . Any  $\boldsymbol{\lambda}$  that violate Eq. (2.20) are disregarded as they lie outside of the confidence region. The remaining  $\boldsymbol{\lambda}$  are then used to generate their corresponding curves,  $\bar{x}(\boldsymbol{\lambda}, \mathbf{p})$ , and evaluated across the parameter space of interest. Once a curve is established across the parameter space, the curve's  $\mathbf{p}^*$  location is identified as the parameter configuration corresponding the minimum  $\bar{x}$  point and then binned accordingly. The final binned values are normalized such that the cumulative sum is 1 in order to establish a probability distribution. From this  $\mathbf{p}^*$ -probability distribution we calculate a mean and standard deviation.

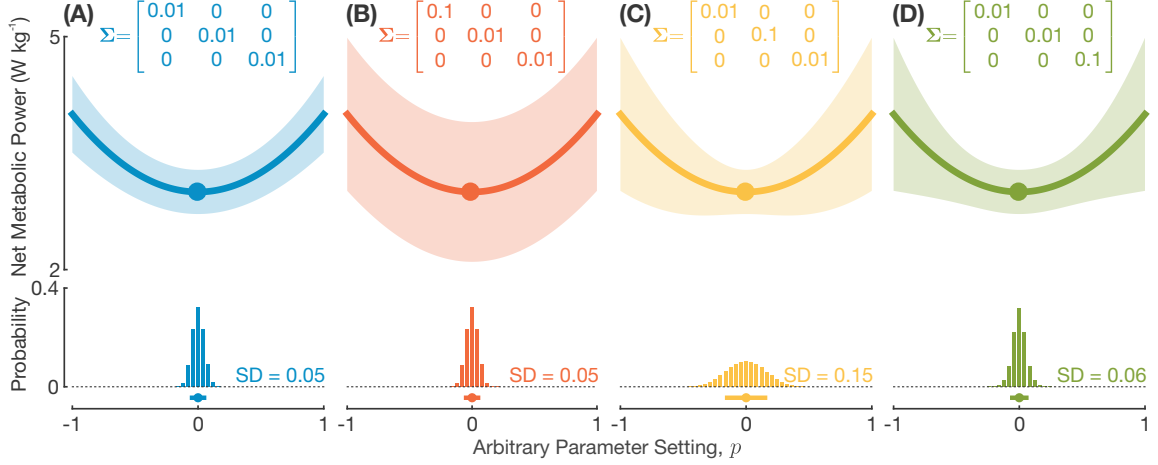


**Figure 2.3: Example of how the covariance matrix affects the confidence analysis.** To illustrate our methodology, these examples highlight the effects of the covariance matrix on the confidence analysis of a metabolic cost landscape. This is a cartoon example of a second order polynomial describing an arbitrary, but realistic, underlying metabolic cost landscape. The shaded region in each figure is the 95% confidence band about the optimally fitted polynomial. The point and bars below each  $p^*$ -probability distribution represent the mean  $\pm 1$  standard deviation of the distribution. In (A) the covariance matrix is a scaled identity matrix. All following sub-figures are depictions of small deviations from this covariance matrix. In (B) we increased the diagonal component that corresponds with  $\lambda_1$  (the vertical offset of the curve) by an order of magnitude. This widens the confidence band in the vertical direction but has no effect on the probability distribution of the minimum location. In (C) we increased the diagonal component that corresponds with  $\lambda_2$  (the slope of the curve) by an order of magnitude. This widens the confidence band at larger slopes and greatly expands the probability distribution of the minimum location. In (D) we increased the diagonal component that corresponds with  $\lambda_3$  (the convexity of the curve) by an order of magnitude. This widens the confidence band at parameter settings relatively far from the minimum location and has a small effect on the probability distribution of the minimum location.

### 2.2.5.5 Example of Confidence Techniques

Both the confidence band on  $\bar{x}(\boldsymbol{\lambda}^*, \mathbf{p})$  and the probability distribution of the minimizing parameter configuration are driven by the covariance matrix  $\boldsymbol{\Sigma}$ . To better show how  $\boldsymbol{\Sigma}$  affects the confidence of a fit, we present a simple example illustrated in Fig. 2.3. Suppose that we have predicted an underlying metabolic cost landscape as a second order polynomial. After performing the fit we found

$$\bar{x}(\boldsymbol{\lambda}^*, \mathbf{p}) = 3 + p^2, \quad (2.24)$$

meaning  $\boldsymbol{\lambda}^* = [3, 0, 1]^\top$ . Fig. 2.3 highlights different possible covariance matrices,  $\boldsymbol{\Sigma}$ , to show how each can affect the confidence of this fit in a different manner. It is important to note that in each scenario of this figure we always have the same  $\bar{x}(\boldsymbol{\lambda}^*, \mathbf{p})$ , yet very different

confidence results depending on the corresponding covariance matrix. For simplicity, we have only considered terms on the diagonal of  $\Sigma$  for this example. In calculating  $\mathcal{F}$ , we have arbitrarily chosen  $n = 100$  and used a critical point of 5%, thus illustrating the 95% confidence region. We computed  $10^5$  Monte-Carlo roll-outs using a multivariate Gaussian generator with  $\Sigma$  and  $\lambda^*$  as inputs to calculate the  $p^*$ -probability distributions.

## 2.2.6 Validation Study with Ankle Exoskeletons

To validate our mapping and confidence analyses, we tested 9 healthy male subjects using bilateral pneumatically powered ankle exoskeletons. We tested with only male participants due to the shoe size requirement of the exoskeleton design. We deemed one subject as an outlier due to inexplicably noisy respiratory measurements (a signal to noise ratio of approximately 2 where the healthy average is approximately 4 [139]). Data from the 8 remaining subjects are presented here (age:  $23 \pm 6$  years; body mass:  $72.2 \pm 5.3$  kg; height:  $179.4 \pm 7.7$  cm; mean  $\pm$  s.d.). All testing was in accordance to the University of Michigan Medical Schools Institutional Review Board and all subjects gave informed written consent to participate in the study prior to testing.

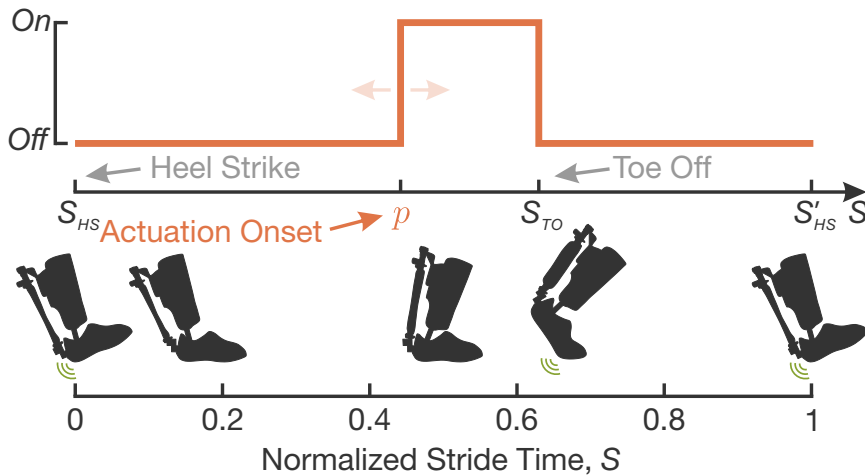


**Figure 2.4: Exoskeleton controller used for experimental validation of confidence analyses.**

The exoskeleton control was based on an “on-off” control law driven by the user’s normalized stride time,  $S$ . When the user’s normalized stride time surpassed the actuation onset threshold,  $p$ , a control signal was sent to the pressure valves to turn the pneumatic muscles on. The muscles were turned off again once the controller detected toe off,  $S_{TO}$ . The timing of actuation onset (encoded in  $p$ ) was the parameter that was explored during testing. Its impact on users’ metabolic power was characterized in the associated cost landscape.

The ankle exoskeletons used in this study had one degree of freedom to allow for users to move their ankles freely in plantar and dorsiflexion. The exoskeletons only assisted in

plantar flexion during the stance phase of the gait cycle. The pneumatic actuators were triggered into an *on* state by the users' normalized stride time,  $S$ , surpassing an actuation onset threshold,  $p$  2.4. We defined  $S$  such that  $S = 0$  represented heel strike while  $S = 1$  represented the following heel strike of the same leg. Actuation was triggered into an *off* state upon toe off detection. The actuation onset threshold,  $p$ , was the control parameter that was varied in exploration protocols in order to estimate its effect on the metabolic power of the user. The hardware for these devices was custom built and designed based upon previous work done by Ferris et al. [44] while the control scheme was based upon work done by Malcolm et al. [101]. Further information about the exoskeleton hardware and control was previously presented by Koller et al. [87, 89].

All subjects were tested with two different parameter exploration protocols, a *step exploration* and a *ramp exploration* (Fig. 2.5). The step exploration tested a number of discrete settings of  $p$  in a randomized order and stayed at each setting for 6 minutes. This type of exploration is the standard practice in the field to collect data for a SSCM analysis [28, 33, 51, 87, 101, 102, 119]. The ramp exploration varied  $p$  continuously over the course of 16 minutes in a bidirectional ramping profile. We conducted a SSCM analysis on the data from the step exploration and an ICM analysis on both data sets.

All participating subjects walked in the exoskeletons on two days. The first day served as a training day for subjects to adapt to the exoskeletons and followed the same protocol as the second day. The second day served as the actual data collection and the results presented here only contain data from this day of testing. During testing, each subject completed the step and the ramp parameter explorations in a randomized order. Subjects were given 5-10 minutes to walk in the exoskeletons at the start of each day to assess exoskeleton fit and allow subjects to familiarize themselves with the devices. Data were collected while walking at a constant speed of  $1.2 \text{ ms}^{-1}$  on an instrumented treadmill (Bertec Corporation, Columbus, OH) and subjects rested in a seated position for 10-20 minutes between exploration protocols. We used a portable open-circuit indirect spirometry system (CareFusion Oxycon Mobile, Hoechberg, Germany) to measure oxygen uptake and carbon dioxide output during testing. We used formulas from Brockway [19] to convert these measurements to metabolic power and normalized measures by subjects' individual mass. During testing, we monitored subject's respiratory exchange ratio (RER) to ensure that it remained in an aerobic state ( $\text{RER} < 1$ ). In addition to the parameter explorations, all subjects completed a 4 minute standing trial of which the final 3 minutes were averaged to calculate subject's standing metabolic power. All measures of metabolic power presented in this paper have the subject's standing metabolic power subtracted to represent their net metabolic power.

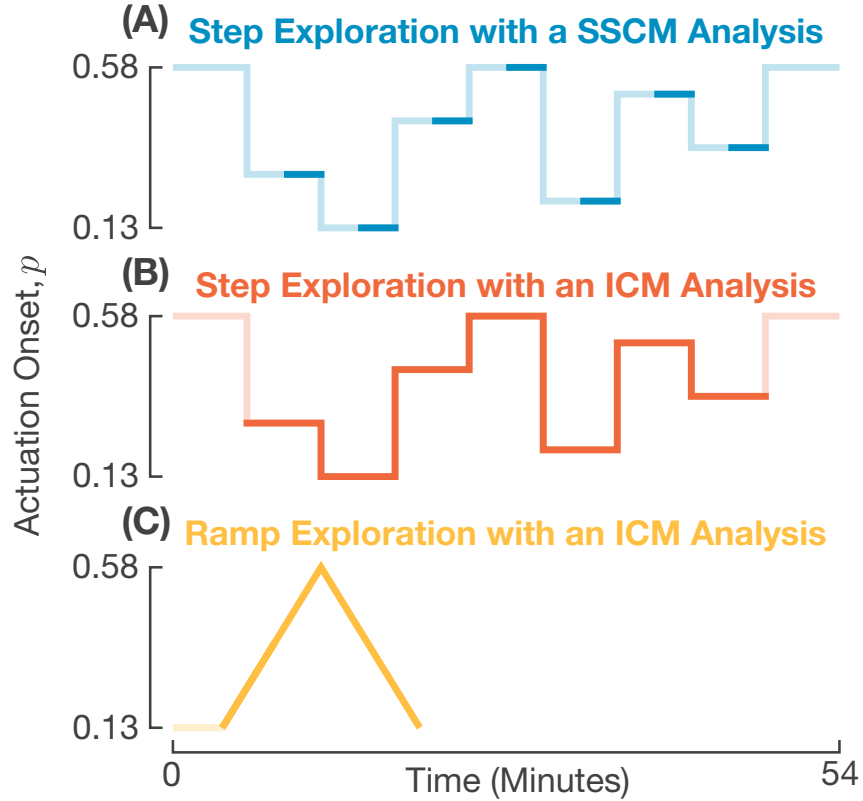


**Figure 2.5: Exploration and analysis protocols used in experimental validation of confidence analyses.** We considered three combinations of parameter exploration and data analysis. In all sub-figures, the bold lines represent data from the corresponding exploration that were used in the analysis. (A) is a step exploration with a SSCM analysis. This is the standard protocol for exploration and analysis in the field of assistive robotic devices. (B) is a step exploration with an ICM analysis. Although this is the same parameter exploration as the standard practice, the ICM analysis allows for the use of steady and non-steady-state data to estimate the metabolic cost landscape. (C) is a ramp exploration with an ICM analysis. During this exploration the parameter configuration is varied in a continuous ramping manner meaning no metabolic steady state is ever reached once the ramping has started.

### 2.2.6.1 Step Exploration

Subjects walked at 9 powered conditions during the step exploration. Each condition lasted for 6 minutes before transitioning to the next. We gave subjects verbal warnings before starting the treadmill, powering on the exoskeletons, and powering off the exoskeletons. There were 7 different parameter settings ( $p = 0.13, 0.21, 0.28, 0.36, 0.43, 0.51,$  and  $0.58$  normalized stride time) that subjects experienced during the 9 different powered conditions. The 1<sup>st</sup>, 5<sup>th</sup>, and 9<sup>th</sup> powered conditions were repeated as  $p = 0.58$  normalized stride time while intermediate powered conditions were randomly chosen from the remaining  $p$  values. We repeated the parameter setting for the 1<sup>st</sup>, 5<sup>th</sup>, and 9<sup>th</sup> powered conditions to

observe learning effects and fatigue in subjects throughout the protocol. For all subjects, the differences in these steady-state values were within the expected measurement noise of users' metabolic power and thus we have concluded that no significant learning or fatigue took place. We chose  $p = 0.58$  normalized stride time for this repeated parameter setting because this setting triggered the *on* state for the shortest amount of time. In doing so, we were able to ease subjects in and out of powered conditions in the safest and smoothest way possible.

The step exploration data was analyzed using both a SSCM analysis and an ICM analysis. For both analyses we only considered data from powered conditions 2-8. We excluded the 1<sup>st</sup> and 9<sup>th</sup> powered conditions from the analyses as to not overweight  $p = 0.58$  normalized stride time in the curve fitting process. We considered steady-state data collected in the final 3 minutes of each powered condition for the SSCM analysis. We considered all powered data for the ICM analysis. In total, the step exploration protocol required 54 minutes of powered walking time per subject. 21 minutes of data were used in the SSCM analysis while 42 minutes of data were used in the ICM analysis. Example time series plots of the powered conditions for the step exploration with corresponding analyses are shown in Figures 2.5A and 2.5B.

### 2.2.6.2 Ramp Exploration

For the ramp exploration, we had subjects begin by walking at a randomized extreme of the parameter space ( $p_0 = 0.13$  or  $p_0 = 0.58$  normalized stride time) for 4 minutes to allow them to reach a metabolic steady-state. The initial parameter setting was then ramped across the parameter space from  $p_0$  to the opposite extreme,  $p_{ext}$ , over the course of 8 minutes. After reaching  $p_{ext}$ , the parameter setting was then ramped back to  $p_0$  over the course of another 8 minutes. Therefore the parameter at breath  $i$ ,  $p_i$ , was a function of time  $t$  (in seconds) since the ramping procedure had begun:

$$p_i = \begin{cases} \frac{3t}{3200} + p_0 & \text{if } t \leq 480 \\ \frac{1440 - 3t}{3200} + p_{ext} & \text{if } t > 480 \end{cases}. \quad (2.25)$$

We chose to use a bidirectional ramping procedure as it has been shown to decrease error in the identified  $p^*$  location if there is an error in the estimated subject-specific time constant,  $\tau$  [75].

We analyzed the ramp exploration data with an ICM analysis using only data collected during the actual ramping procedure. Therefore, the protocol required 20 minutes of pow-

ered walking per subject, and 16 minutes of data were used in the analysis. A time series plot of the powered conditions for the ramp exploration with an ICM analysis is shown in Fig. 2.5C.

### 2.2.6.3 Estimating subject-specific $\tau$

The computation of  $\mathbf{A}_{\text{ICM}}$  requires a subject-specific time constant,  $\tau$ . There are a number of ways to estimate a subject-specific  $\tau$  [43, 118]. We chose to compute  $\tau$  from the readily available step exploration data. We averaged the data from the final 3 minutes of each powered condition and used this as an estimate of instantaneous metabolic cost at each corresponding parameter configuration,  $\bar{x}_i$ . Substituting  $\bar{x}_i$  for  $\mathbf{g}(\mathbf{p}_i)^\top \boldsymbol{\lambda}$  in Eq. (2.11), we used MATLAB’s Optimization Toolbox to determine the  $\tau$  and  $\bar{y}_1$  that resulted in the smallest sum of squared error between the estimated metabolic measurements,  $\bar{y}_i$ , and the actual measurements,  $\hat{y}_i$ ,

$$\min_{\tau, \bar{y}_1} \sum_{i=1}^N (\bar{y}_i - \hat{y}_i)^2. \quad (2.26)$$

We used all powered condition data for this optimization beginning from the steady state of the first powered condition.

### 2.2.6.4 Cost Mapping Analyses and Statistical Testing

For both the ICM and SSCM analyses, we estimated the cost landscape using a third order polynomial; therefore, we defined the vector of basis functions as

$$\mathbf{g}(p) = [1, p, p^2, p^3]^\top. \quad (2.27)$$

We used these basis functions in order to be consistent with work presented in [101]. We considered the 95% confidence region for all confidence band analysis by using a 5% critical point in calculating  $\mathcal{F}$ . We computed  $10^5$  Monte-Carlo roll-outs in calculating the  $p^*$ -probability distribution. We regarded the step exploration with a SSCM analysis as the current field standard and all reported comparisons are made relative to it. We used a paired t-test ( $\alpha = 0.05$ ) for all reported p values.

## 2.3 Results

From the 8 subjects presented here, we identified subject-specific time constants,  $\tau$ , of  $47.8 \pm 12.4$  (mean  $\pm$  s.d.) seconds. The fitted curve from the standard SSCM protocol

shows that subjects on average experience a  $0.808 \pm 0.184 \text{ W kg}^{-1}$  ( $19.6 \pm 3.3\%$ ) reduction in metabolic power between the worst case parameter setting and  $p^*$ . All major results comparing both explorations with an ICM analysis to the standard SSCM are shown in Fig. 2.6.

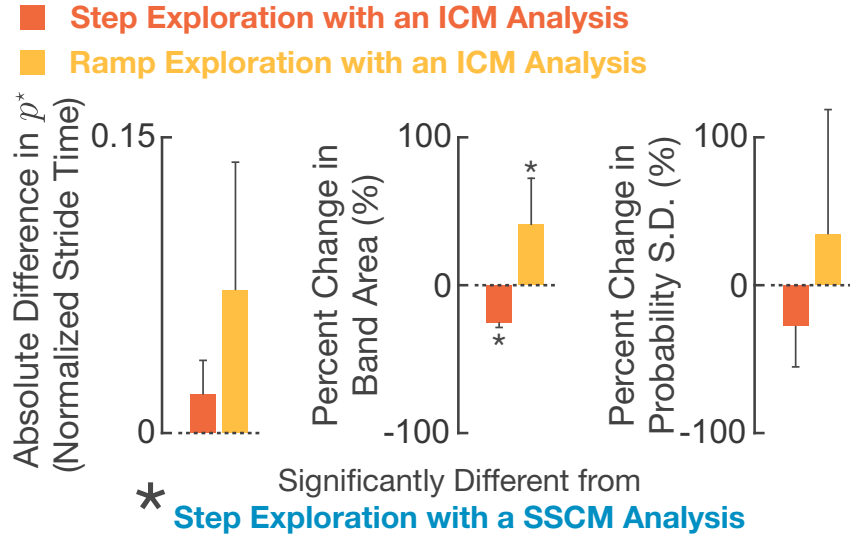


**Figure 2.6: Experimental results comparing parameter explorations and analyses against one another.** Experimental results compare the metabolic cost landscapes of both the step and ramp explorations with an ICM analysis to the standard practice of a step exploration with a SSCM analysis. The results show that neither protocol had a significant difference in identified  $p^*$  locations or standard deviations of the  $p^*$ -probability distributions when compared to the standard practice protocol. There was a significant difference in both protocols’ band area when compared to the standard practice.

### 2.3.1 Step Exploration with an ICM Analysis

The step exploration with an ICM analysis identified  $p^*$  configurations that were on average  $0.012 \pm 0.024$  normalized stride time away from that identified by the standard step exploration with a SSCM analysis. This is an absolute difference of  $0.020 \pm 0.017$  normalized stride time. The differences in  $p^*$  configurations predicted by the two protocols were not significantly different from zero ( $p = 0.187$ ).

The confidence analysis shows that the step exploration with an ICM analysis resulted in an area of the 95% confidence band about  $\bar{x}(\lambda^*, p)$  that was  $25.1 \pm 3.5\%$  less than that of the standard SSCM analysis. The differences in the two protocol’s band areas was significantly different from zero ( $p < 0.001$ ). However, when comparing the  $p^*$ -probability distributions, there was no significant difference in the mean or standard deviation ( $p = 0.132$ ).

and  $\mathbf{p} = 0.088$ , respectively) between the two protocols. The results of this protocol for a single representative subject are shown in Fig. 2.7.

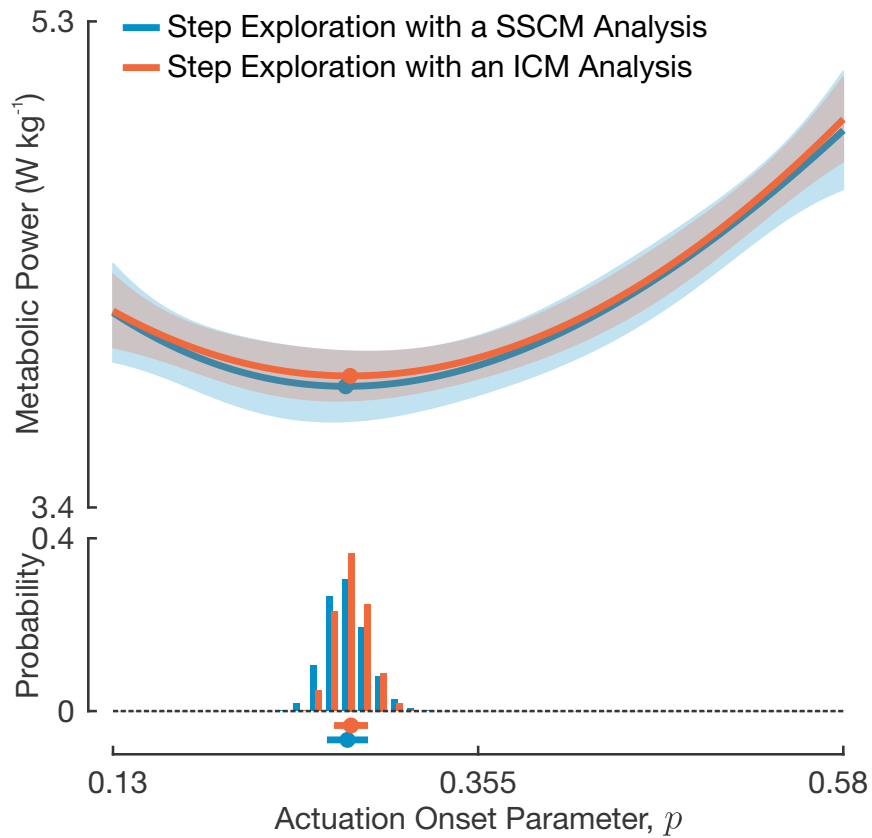


**Figure 2.7: Comparing a step exploration with a SSCM analysis to a step exploration with an ICM analysis for a single representative subject.** For this representative subject, the step exploration with an ICM analysis had a confidence band area about  $\bar{x}(\lambda^*, p)$  that was 28% less than that of the step exploration with a SSCM analysis. The  $p^*$ -probability distribution of the step exploration with an ICM analysis had a standard deviation 17% less than that of the step exploration with a SSCM analysis.

### 2.3.2 Ramp Exploration with an ICM Analysis

The ramp exploration with an ICM analysis identified  $p^*$  configurations that were on average  $0.016 \pm 0.020$  normalized stride time away from that identified by the standard step exploration with a SSCM analysis. This is an absolute difference of  $0.072 \pm 0.065$  normalized stride time. The differences in  $p^*$  configurations predicted by the two protocols were not significantly different from zero ( $\mathbf{p} = 0.661$ ).

The confidence analysis shows that the ramp exploration with an ICM analysis resulted in an area of the 95% confidence band about  $\bar{x}(\lambda^*, p)$  that was  $41.2 \pm 31.1\%$  greater

than that of the standard SSCM analysis. The differences in the two protocol’s band areas was significantly different from zero ( $p = 0.005$ ). However, when comparing the  $p^*$ -probability distributions, there was no significant difference in the mean or standard deviation ( $p = 0.350$  and  $p = 0.915$ , respectively) between the two protocols. The results of this protocol for a single representative subject are shown in Fig. 2.8.

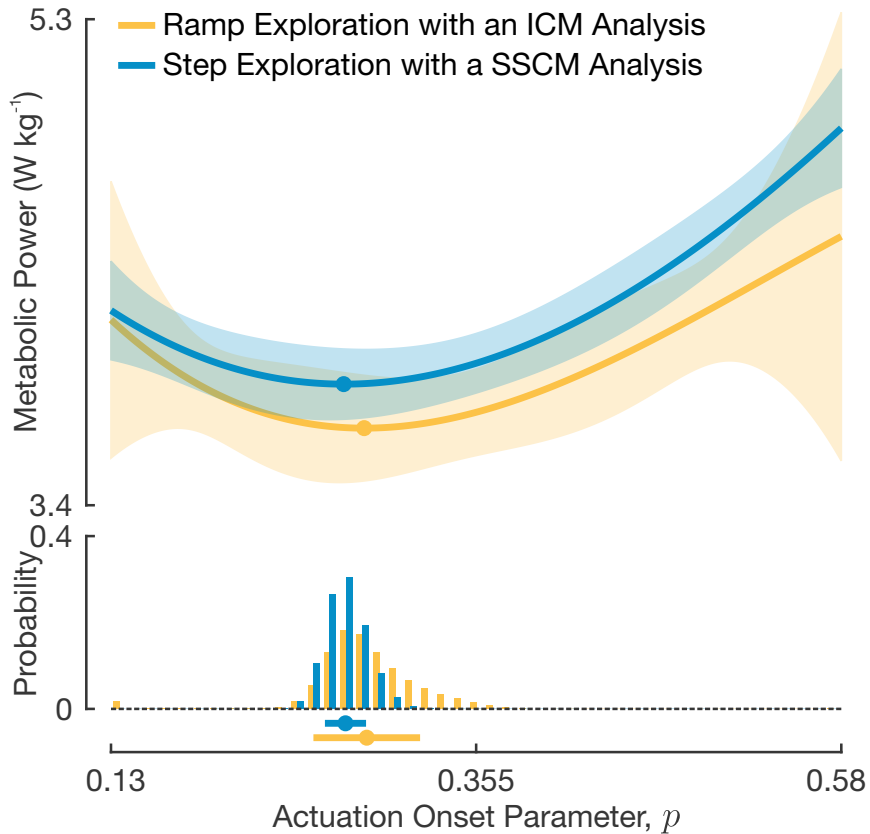


**Figure 2.8: Comparing a step exploration with a SSCM analysis to a ramp exploration with an ICM analysis for a single representative subject.** For this representative subject, the ramp exploration with an ICM analysis had a confidence band area about  $\bar{x}(\lambda^*, p)$  that was 86% greater than that of the step exploration with a SSCM analysis. The  $p^*$ -probability distribution of the step exploration with an ICM analysis had a standard deviation 159% greater than that of the step exploration with a SSCM analysis. This is the same representative subject as shown in Fig. 2.7.

## 2.4 Discussion & Conclusion

We presented a generalized instantaneous cost mapping (ICM) analysis that allows for the use of steady and non-steady-state measures in estimating metabolic cost landscapes of any dimensionality or order. Additionally, we derived novel confidence analyses that

allow for an in-depth evaluation of curve fits and a comparison of mapping protocols on a subject-specific basis. We demonstrated these techniques by mapping healthy subjects' metabolic cost landscapes as functions of the actuation onset for pneumatically powered bilateral ankle exoskeletons. We first showed how an ICM analysis can improve upon a steady-state cost mapping (SSCM) analysis, the current standard in the field, when using a step exploration. The results show that an ICM analysis can decrease the 95% confidence band area about  $\bar{x}(\lambda^*, p)$  by  $25.1 \pm 3.5\%$  with no significant change in the identified  $p^*$  configuration ( $\mathbf{p} = 0.187$ ) when compared to a SSCM analysis of the same parameter exploration. This significant decrease in band area ( $\mathbf{p} < 0.001$ ) indicates a more confident fit in an ICM analysis than a SSCM analysis when the same parameter exploration is used for both. This result is a consequence of the fact that the ICM analysis is able to include twice as much data as the SSCM analysis. This point illustrates that if the physical shape and absolute values of  $\bar{x}(\lambda^*, p)$  are of importance then it may be worth using an exhaustive step exploration with an ICM analysis to maximize the amount of data being considered in a fit.

Knowing that an ICM analysis can be used to include non-steady-state measurements in estimating a metabolic cost landscape, we then asked the question of “what is the penalty in estimating a metabolic cost landscape using a much shorter parameter exploration?” The ramp exploration with an ICM analysis included no steady-state data in the analysis and required less than half the time to conduct than the standard step exploration with a SSCM analysis. We found that the  $p^*$  configurations identified by the ramp exploration with an ICM analysis were not significantly different from that of the step exploration with a SSCM analysis ( $\mathbf{p} = 0.661$ ). The  $p^*$  configurations identified using the ramp exploration with an ICM analysis were on average  $0.016 \pm 0.020$  normalized stride time away from that identified by the standard step exploration with a SSCM analysis. This difference in  $p^*$  configurations would only result in an average increase of 1.2% in metabolic power when evaluated using the curve identified by the SSCM analysis. Additionally, there was no significant difference in  $p^*$ -probability distribution means or standard deviations between the ramp exploration with an ICM analysis and that of the step exploration with a SSCM analysis ( $\mathbf{p} = 0.350$  and  $\mathbf{p} = 0.915$ , respectively). These results suggest that a shortened parameter exploration with an ICM analysis can identify  $p^*$  configurations with no significant difference in accuracy to that of the field's standard step exploration with a SSCM analysis. However, there was a significant increase in the 95% confidence band area about  $\bar{x}(\lambda^*, p)$  identified using the ramp exploration with an ICM analysis compared to that of the step exploration with a SSCM analysis ( $\mathbf{p} = 0.005$ ). This increase in band area of  $41.2 \pm 31.1\%$  suggests that a short parameter exploration with an ICM analysis may not

be best when the overall shape and absolute values of the metabolic cost landscape are of interest. We would like to emphasize that we are not advocating that the ramp exploration presented here is the *optimal* means of traversing a parameter space in order to estimate a metabolic cost landscape, but it is just one of infinitely many possible continuous exploration patterns. Further investigation is needed to identify what exploration practices are best when using an ICM analysis. Additionally, the minimum time required for an ICM protocol to accurately identify a minimizing parameter configuration can vary from device to device depending on how many parameters need to be tuned and the level of impact those parameters have on the users' metabolic power.

A major take away of this work is that we can now consider subject-specific confidence on estimated cost landscapes and minimizing parameter configurations. We believe these methods play an important role in protocol validation and comparisons as alternative mapping protocols emerge in the field. In future work we hope to use curve confidence to better inform autonomous and “smart” explorations of parameter spaces when considering a multidimensional parameter space. For example, the elements of  $\Sigma$  can directly inform an algorithm which elements of  $\lambda^*$  it is least confident in identifying. Thus, the covariance matrix can indicate which direction of the parameter space is needed to be further explored to gain a more accurate estimate of the cost landscape or minimizing parameter configuration. This type of information could be very useful for directing ‘Body-in-the-Loop’ optimizations in future work [43,87].

The methods we have presented here have been formulated in a generalized notation such that they can be applied to any type of sensor that estimates a physiological measure so long as the sensor dynamics can be described as a linear equation. Alternative sensors may take measurements of limb dynamics, heart rate, or electrodermal activity [16,41,107]. Although none of these sensors alone can accurately estimate metabolic power, the combination of many sensors using sensor fusion can potentially improve this estimate [41]. Future work is aimed at developing methods for sensor fusion of these types of measures to better estimate real-time metabolic power. Furthermore, metabolic power is only a single objective function to consider when tuning a device. We believe that considering alternative cost landscapes will be necessary for applying these techniques to clinical populations where measures other than metabolic power may be of greater concern when tuning a device. Recent work has shown that users' perception of their biomechanics, or satisfaction in a given parameter configuration, does not always correlate with their measured metabolic power [110]. Measures of user satisfaction can be a combination of measures such as balance, comfort, stress, or perceived effort. Given that physiological objectives other than metabolic power contribute to user satisfaction, it may be necessary to consider these ob-

jectives during the tuning of devices in future work. The investigation of alternative sensors could allow for these other physiological objectives to be measured and considered as alternative cost landscapes. The sensors associated with these measures need to be more transparent and less cumbersome than a metabolics mask so they can be used on a daily basis. We believe the methods laid out here will be a key starting point for this ground work.

The presented methods are not constrained to control parameters on assistive robotic devices. A wide variety of experimental biomechanics studies aim to estimate metabolic cost landscapes as a function of biomechanical manipulations. For example, studies have looked at the effects of walking speed, walking incline, step frequency, or step width on metabolic power [39, 40, 63, 104, 133, 150]. These types of studies could greatly benefit from the techniques we have described here. The curve confidence methods could aid in the experimental design process by providing more information to the researchers about a given protocol and would allow for a more quantitative inter-subject analysis. Additionally, these studies could use ICM techniques to include more data in their analyses if they wish to improve curve confidence or they could use ICM techniques to significantly reduce testing time if they wish to only identify experimental parameters that minimize metabolic power.

## 2.5 Appendix: Proving an Analytic Solution to Solving the Confidence Band of a Curve

The analytic solution for the confidence band of a curve is the result of solving the extremal problem

$$\begin{aligned} \max/\min_{\lambda^\circ} \quad & \mathbf{g}(\mathbf{p}^\circ)^\top (\boldsymbol{\lambda}^\circ - \boldsymbol{\lambda}^*) \\ \text{subject to} \quad & (\boldsymbol{\lambda}^\circ - \boldsymbol{\lambda}^*)^\top \mathbf{V} (\boldsymbol{\lambda}^\circ - \boldsymbol{\lambda}^*) \leq 1 \end{aligned} \quad (2.28)$$

Here we will only solve for the minimization, but the maximization follows a similar proof. We can solve for the above minimization using a change in variables to simplify the problem statement. We first assume that  $\boldsymbol{\Sigma}$  is a positive definite matrix (as opposed to positive semi-definite) since there is guaranteed to be noise in our measurements. If  $\boldsymbol{\Sigma}$  is a positive definite matrix,  $\mathbf{V}$  is also a positive definite matrix. Therefore,  $\mathbf{V}$  has a positive definite principal square root,  $\mathbf{V}^{1/2}$ . Defining  $\tilde{\mathbf{z}} = \mathbf{V}^{1/2}(\boldsymbol{\lambda}^\circ - \boldsymbol{\lambda}^*)$  and  $\tilde{\mathbf{g}} = \mathbf{V}^{-1/2}\mathbf{g}(\mathbf{p}^\circ)$ , we can simplify Eq. (2.28) to

$$\begin{aligned} \min_{\tilde{\mathbf{z}}} \quad & \tilde{\mathbf{g}}^\top \tilde{\mathbf{z}} \\ \text{subject to} \quad & \tilde{\mathbf{z}}^\top \tilde{\mathbf{z}} \leq 1. \end{aligned} \quad (2.29)$$

We then can express the Lagrange equation for the above as

$$\mathcal{L}(\tilde{\mathbf{z}}, \alpha) = \tilde{\mathbf{g}}^\top \tilde{\mathbf{z}} + \alpha (\tilde{\mathbf{z}}^\top \tilde{\mathbf{z}} - 1) \quad (2.30)$$

where  $\alpha$  is the Lagrangian multiplier. The partial derivatives of the Lagrange equation are

$$\begin{aligned} \frac{\partial \mathcal{L}}{\partial \tilde{\mathbf{z}}} &= \tilde{\mathbf{g}} + 2\alpha \tilde{\mathbf{z}} \\ \frac{\partial \mathcal{L}}{\partial \alpha} &= \tilde{\mathbf{z}}^\top \tilde{\mathbf{z}} - 1. \end{aligned} \quad (2.31)$$

Setting the partial derivatives equal to zero and solving for  $\tilde{\mathbf{z}}$  results in

$$\tilde{\mathbf{z}}_{min} = \frac{-\tilde{\mathbf{g}}}{\|\tilde{\mathbf{g}}\|_2}. \quad (2.32)$$

Substituting for  $\tilde{\mathbf{z}}$  and  $\tilde{\mathbf{g}}$ , we can solve for the  $\lambda^\circ$  that corresponded to the analytic solution of the confidence band.

$$\lambda_{min}^\circ = \lambda^* - \frac{\mathbf{V}^{-1} \mathbf{g}(\mathbf{p}^\circ)}{\sqrt{\mathbf{g}(\mathbf{p}^\circ)^\top \mathbf{V}^{-1} \mathbf{g}(\mathbf{p}^\circ)}}. \quad (2.33)$$

## CHAPTER 3

# ‘Body-in-the-Loop’ Optimization of Assistive Robotic Devices

### 3.1 Introduction

The control of a typical assistive robotic device relies on *mechanically intrinsic* measurements. These are measurements that come from the device itself and they are used to estimate the state of the human-machine system. These state estimates allow for the controller to determine the user’s intent and the current phase of a given task. With this information, the controller allows the assistive device to aid the user in a variety of scenarios. Examples of mechanically intrinsic measurements include position, velocity, force, and impedance [6, 17, 64]. For example, in an upper extremity exoskeleton, force measurements between the user and the device can be used to predict the user’s intended reaching trajectory [100]. Or in a lower limb prosthesis, acceleration measurements of the device can be used to estimate what phase of the gait cycle the user is currently in. This same acceleration measurement can determine if the user is intending to climb stairs or walk on level ground [79].

While mechanically intrinsic measurements estimate the state of the human-machine system, *physiological* measurements such as pain, anxiety, effort, or energy consumption, are commonly used to evaluate the performance of the device. Conclusions based on these physiological measurements are then used to alter the design and to modify the shape of actuation to better assist the user. The process of using physiological measurements to shape actuation is an iterative, trial-and-error process. The measurements need to be taken during human subject testing and then analyzed by researchers or clinicians offline after testing. The results from this analysis are then used to drive future designs of actuation

---

The content of this chapter has been previously published and presented at Robotics: Science and Systems 2016 [87].

shape or tuning for a given device. This process is repeated until the desired results are achieved. For example, in an upper extremity prosthesis, measurements of user pain can be used to iteratively shape actuation such that users are most comfortable [103]. Or in a lower limb exoskeleton, measurements of energy consumption can be used to tune parameters that shape actuation profiles in an attempt to identify parameters that result in the largest reduction in the user’s metabolic effort [101].

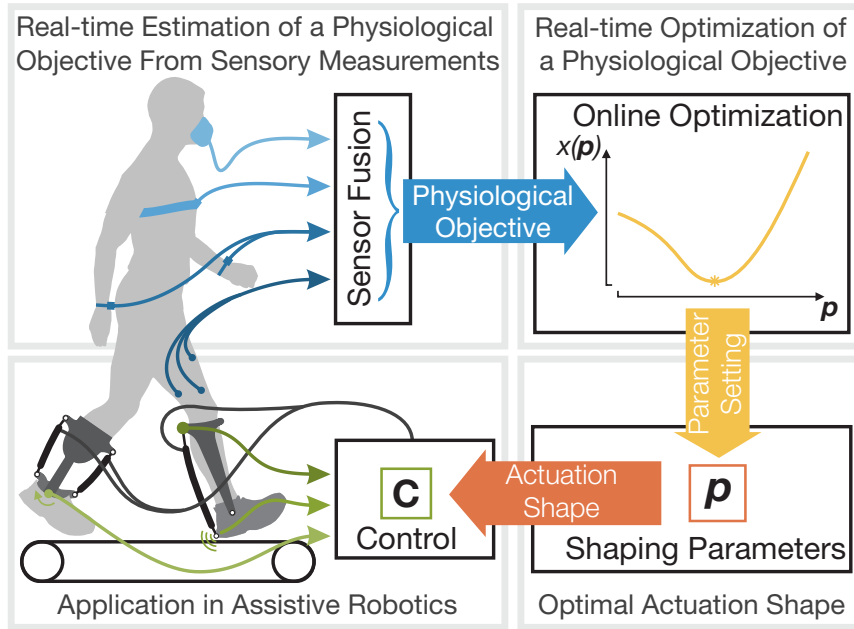


**Figure 3.1: An example of the generalized approach to the Body-in-the-Loop optimization of assistive robotic devices.** Here is an illustration of the proposed concept of Body-in-the-Loop optimization. While a user is wearing an assistive robotic device (shown are devices that aid locomotion), a number of sensor readings are fused to form an estimate of a physiological measure  $x$  (such as pain, anxiety, effort, or energy consumption). This physiological measure is used as the objective function in an online optimization that identifies optimal controller parameters  $p$ . These targeted controller parameters influence the shape of assistance that is provided by the assistive device to the user. Additional intrinsic measurements from the device are used to estimate user intent and phasing of the assistance to drive the output of the controller  $C$ . Optimization is done with a human body in the loop which is a radically new way of human-machine interfacing.

Clearly, both mechanically intrinsic measurements and physiological measurements are needed for the design and control of assistive robotic devices. However, in the current field of assistive robotic devices there is a divide between these measurements as they are not used concurrently in real-time control. We are proposing a new method of human-machine interfacing, one in which control parameters that shape assistance,  $p$ , are optimally tuned and adjusted in real-time to minimize a *physiological* objective function from the user,  $x(p)$ . By including physiological measurements,  $y$ , in the control scheme to estimate

$x(p)$  and drive optimization, we are bringing the human body into the control loop. This *Body-in-the-Loop* approach has the potential to open up a new realm of assistive robotic control.

By including quantitative physiological feedback in a real-time optimization of shaping parameters, we can create robotic devices that learn and adapt in order to continuously provide optimal subject-specific assistance. The optimization process can be performed during the development of a controller for a new assistive system, as well as every time a particular device is fitted to a user. This allows adaptation to unique attributes such as the user's size, weight, or preferred movements, and it will greatly improve and accelerate the tedious task of controller tuning. It will substantially enhance the performance of current assistive robotic devices by optimally utilizing potential synergies between user and machine. In the long run, the proposed automated tuning can be applied not only when a device is built or fitted, but on a continuous basis as the person uses it. For example, in the case of a lower limb prosthesis, the controller could adapt in real-time to the type of shoes that the person is wearing, the terrain that is being traversed, or additional loads that a user might be carrying.

Felt et al. proved such an optimization was possible by optimizing step frequencies during normal walking of healthy subjects as a proof of concept [43]; however, this type of optimization has never been demonstrated on an actual assistive device until now. Here we expand upon Felt's work by presenting the first ever example of *Body-in-the-Loop* optimization driven by objective physiological measurements to optimize the control of an assistive robotic device. We build upon Felt's algorithm by including an oscillatory perturbation pattern, a growing sample window, and statistical confidence checks of each gradient estimate. All of these additions were crucial for improving the performance of *Body-in-the-Loop* optimization when applying these techniques to assistive devices due to the cost landscape being much shallower compared to that of Felt's step frequency study.

In this paper we have demonstrated the utility of *Body-in-the-Loop* techniques for the optimization of bilateral pneumatically actuated ankle exoskeletons during level ground walking. These exoskeletons provided additional power to aid in push-off, reducing the metabolic effort required of the individual. We chose such a platform because devices targeting assistance at the ankle are commonly used in both a research and clinical setting due to the ankle's large contribution toward positive power generation during gait [9, 42, 77, 101]. Our designed exoskeletons were simply controlled by a single shaping parameter,  $p$ , which controlled the actuation onset of the device.  $p$  represents a normalized stride time threshold such that once a user's phase of normalized stride surpassed  $p$ , action was turned on. This is visualized in Figure 3.4 and has been a common control scheme used

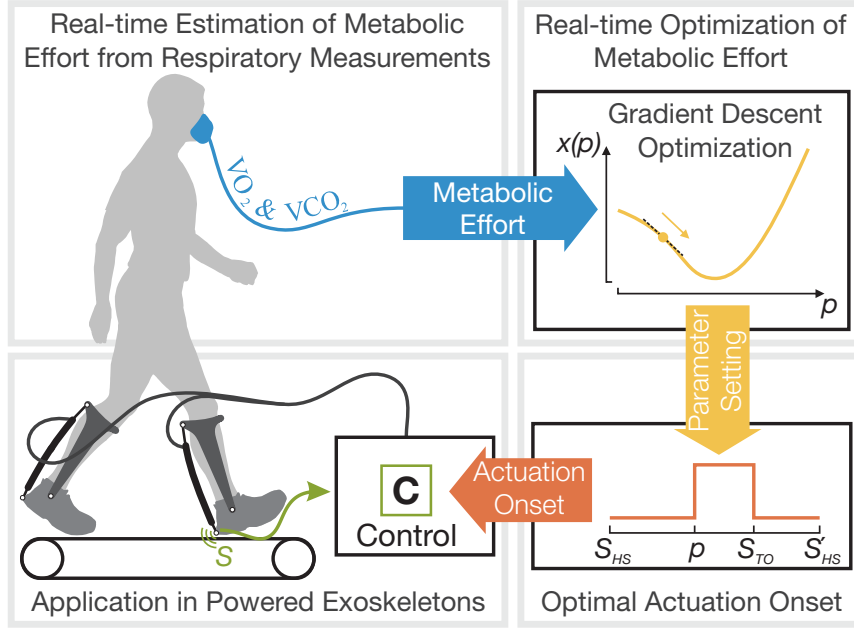


**Figure 3.2: Proposed experiment for Body-in-the-Loop optimization of bilateral robotic ankle exoskeletons.** In a validation study, we optimized the actuation onset (as parameter  $p$ ) of bilateral ankle exoskeletons to minimize user’s metabolic effort (as physiological objective  $x(p)$ ). The exoskeleton controller used normalized stride time between consecutive heel strikes ( $S_{HS}$  and  $S'_{HS}$ ) as the state estimate to drive actuation. Actuation was turned on when the normalized phase of the stride  $S$  was greater than the parameter setting  $p$  and off when toe off ( $S_{TO}$ ) was detected. We implemented gradient descent optimization techniques to autonomously move toward a setting of  $p$  that minimized  $x(p)$ . With this robotic device, we validated the Body-in-the-Loop techniques with eight healthy subjects, using a brute force mapping of subject specific cost landscapes as a ground truth for comparison.

for basic science research with robotic ankle exoskeletons [24, 101]. The Body-in-the-Loop optimization scheme tuned  $p$  using metabolic effort as the physiological objective. We were able to estimate the user’s metabolic effort in real-time via respiratory measurements using a mask as shown in Figure 3.3. Through the results from an extensive human subject study, we have shown that the proposed Body-in-the-Loop optimization techniques can autonomously move towards a metabolic minimum validating that Body-in-the-Loop optimization has the potential to be an impactful tool for future human-machine interactions.

### 3.2 A Pneumatically Actuated Robotic Ankle Exoskeleton

We used bilateral, single degree of freedom, pneumatically actuated ankle exoskeletons as a platform for testing the proposed Body-in-the-Loop optimization. We designed these exoskeletons based on previous work in the field [44].

### 3.2.1 Hardware

Each exoskeleton consisted of a shank and a foot component connected by a rotational joint. The shank diameter was adjustable via ratcheting straps to fit a variety of subject sizes. The shoes were customized orthotic shoes that had been outfitted with a stainless steel plate in the heel. This plate served to stiffen the heel of the shoe and provide attachment points for the actuators and rotational joints.

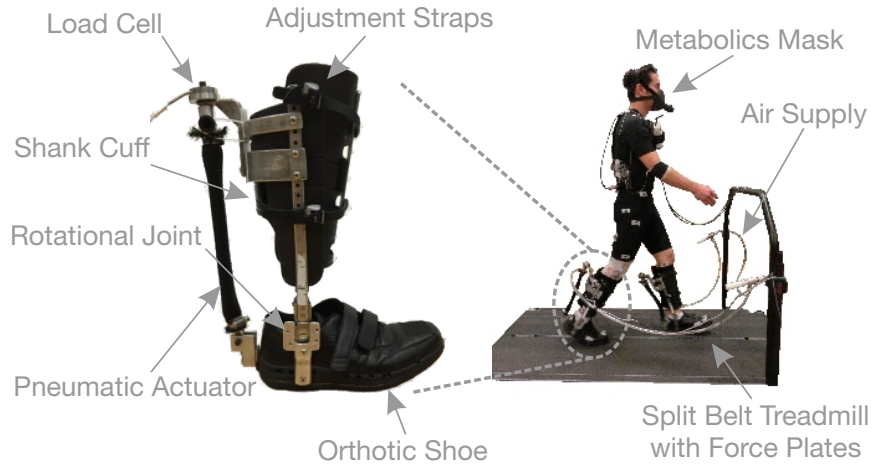


**Figure 3.3: Experimental setup for Body-in-the-Loop optimization of bilateral robotic ankle exoskeletons.** The ankle exoskeletons used in this study were pneumatically actuated with custom built artificial pneumatic muscles attached posteriorly to assist with push off. During testing, subjects walked on a split belt treadmill with incorporated force plates to register heel strike and toe off events. Respiratory measurements were recorded in real time with a metabolics mask. The air pressure in the actuators was regulated with off board proportional pressure control valves (not shown). Adjustment straps allow fitting the device to different users.

We actuated each exoskeleton with a custom made artificial pneumatic muscle [31] that had attachment points at the top-rear of the shank and at the back of the heel. The moment arm between the rotational joint and the actuation attachment point at the heel was 10.1 cm. The artificial muscle was connected to a proportional pressure control valve (MAC Valves, Wixom, MI) with a mechanical quick release valve (Parker Legris, Mesa, AZ) connected in series. Additionally, we attached a load cell (Omega Engineering, Stamford, Connecticut) in series with the artificial muscle to record actuation kinetics. This actuation configuration had an electromechanical delay of 28 ms. In optimal controller configurations, this exoskeleton can provide approximately 50% of the torque required at the ankle during normal walking. Each exoskeleton, artificial pneumatic muscle, and load cell had a combined weight of 2.02 kg. This weight was slightly larger than other state of the art exoskeletons in the field, yet it was within the weight range of exoskeletons that have

previously shown significant reductions in metabolic effort (0.67 - 2.30 kg [101, 106]).

### 3.2.2 Control

We controlled the exoskeleton using a simple state-based control strategy that has been presented in previous ankle exoskeleton work [24, 101]. The controller was simply an ‘on-off’ control scheme that was triggered by a single state,  $S$ , crossing a threshold value,  $p$ .  $p$  is the shaping parameter that we optimized for during validation testing.  $S$  was a measure of normalized stride time where  $S = 0$  and  $S = 1$  corresponded to consecutive heel strikes of the same leg. We used vertical ground reaction forces on the treadmill to detect heel strike,  $S_{HS}$ , and toe off,  $S_{TO}$ , of each stride. We calculated stride times from the time between consecutive heel strikes of the same leg and then normalized them by an average stride time to calculate  $S$ . We calculated the average stride time using a finite impulse response filter with a tap size of five.

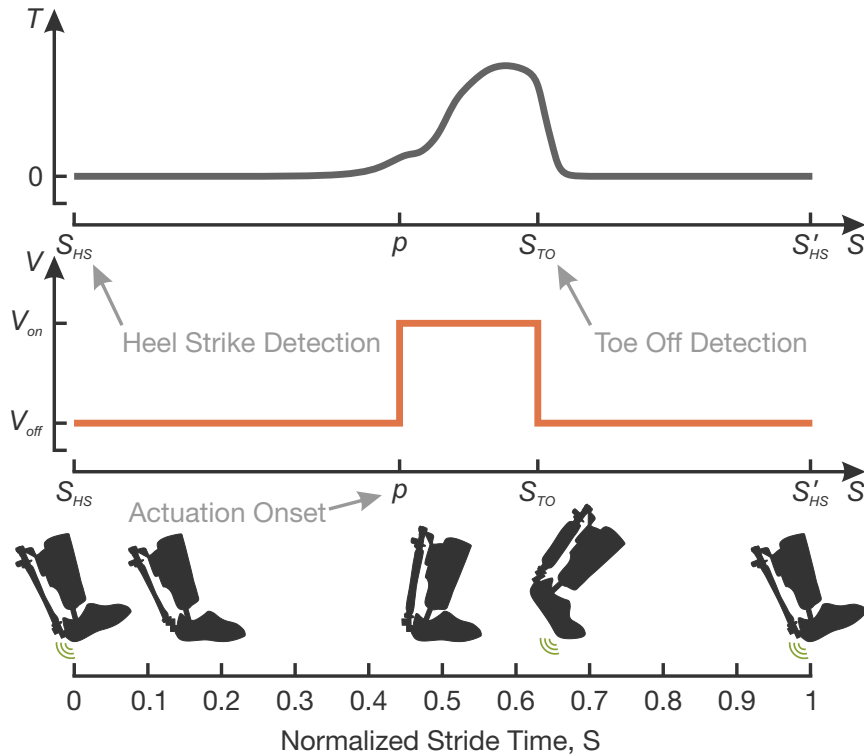


**Figure 3.4: Controller to be optimized during the Body-in-the-Loop optimization.** The control signal that was sent to the pressure control valves was based upon normalized stride time,  $S$ . The bottom graph shows a single stride of the exoskeleton where  $S_{HS} = 0$ ,  $S_{TO} \approx 0.63$ , and  $S'_{HS} = 1$ . The middle graph shows how actuation is turned on once  $S \geq p$  and off once  $S \geq S_{TO}$ . The top graph shows an example of the expected torque output of the exoskeleton. This profile will change dependent upon what  $p$  is set to and as a function of user specific ankle kinematics during walking.

When  $p \leq S \leq S_{TO}$ , actuation was turned *on*. Actuation was turned *off* otherwise. When the controller was in the *on* state, we pressurized the artificial pneumatic muscles with 600 kPa of pressure and when in the *off* state with 150 kPa of pressure. The reason for a non-zero *off* state pressure was to deplete any dead space in the tubing and muscle. This allowed for a quicker actuation response and limited electromechanical delay in our control system. The *off* pressure of 150 kPa did not result in any inflation of the artificial pneumatic muscle and thus no tension was registered by the load cells during the *off* state due to actuation pressure.

### 3.3 Metabolic Effort as a Physiological Cost Function

For this study we used metabolic effort as the physiological cost function,  $x(p)$ , to minimize. In relation to metabolic effort,  $x(p)$  is also known as the *instantaneous energetic cost* [118]. Metabolic effort is a measure of how much energy the human body is expending during any task and can be estimated from a variety of physiological measurements such as oxygen consumption, heart rate, oxygen saturation in the blood, or muscle activity [19,54,71,84]. Most commonly, metabolic effort is estimated from oxygen consumption via respiratory measurements,  $y$ , and is a primary method for evaluation of assistive robotic devices [38]. In collecting respiratory measurements, subjects wear a mask that samples the oxygen and carbon dioxide content of each individual breath. Using equations from Brockway [19] and normalizing by subject mass, we convert these respiratory measurements ( $\frac{mL}{sec}$ ) to measurements of energy consumption ( $\frac{W}{kg}$ ).

Although respiratory measurements give us a fairly accurate estimate of metabolic effort, there are significant sensor dynamics that prevent measuring  $x(p)$  directly. Respiratory measurements are ideally meant for long testing trials at steady state conditions due to a long delay between the instantaneous energetic demand and the physical respiratory measurements. When muscles need instantaneous energy they pull from local energy storage in the form of adenosine triphosphate (ATP). These local storages of ATP are then replenished through a number of processes that require oxygen pulled from the blood stream. It takes time for this oxygen depleted blood to travel from the muscle location to the lungs, so there is a delay between this initial recruitment of energy and the observation of increased oxygen consumption via respiratory measurements. Because of this delay, the dynamics of the human metabolic system are commonly modeled as a first order system, having a time constant  $\tau$  of approximately 40 seconds during walking [91, 118, 139]. It is common practice to have subjects walk at a given condition for at least three minutes to allow for metabolic effort to stabilize prior to collecting measurements for analysis due to this large

time constant. Additionally, respiratory measurements are very sparse because only one measurement is made per breath. During normal walking subjects take approximately 19 breaths per minute which results in a sample rate of 0.32 Hz [18]. On top of all that, respiratory measurements are incredibly noisy, having a signal to noise ratio of approximately four [91, 139]. Given this sparse sample rate and high noise level, it is typical to average respiratory measurements across multiple minutes to achieve a single data point estimate of  $x(p)$ .

Dynamic delay, sparse sampling, and large inter-breath variability all make for using respiratory measurements to drive an online optimization increasingly difficult. In order to use this information in a real-time optimization, we need to establish a suitable sensor model of respiratory measurements. The input to this sensor is the instantaneous energetic cost  $x(p_i)$ . The output are individual breath measurements of energy consumption  $y_i$ .  $i$  is the breath number and replaces a notion of time in this discrete breath-by-breath process. Approximating the metabolic dynamics as a discrete linear first order system, we relate respiratory measurements,  $y_i$ , of each breath  $i$ , to metabolic effort,  $x(p_i)$ :

$$y_i = \left(1 - \frac{h_i}{\tau}\right) y_{(i-1)} + \frac{h_i}{\tau} x(p_i). \quad (3.1)$$

In this equation,  $h_i$  is the time since the previous breath and  $\tau$  is the time constant of the metabolic system [43].

## 3.4 Optimization of Metabolic Effort

Based on this sensor model, we developed an algorithm for the real-time optimization of metabolic effort. Please note that the figures in this section are representing exemplary data from a single pilot subject. Data from the complete validation study is presented in Section 3.5.2.

### 3.4.1 Establishing a Ground Truth

In order to objectively evaluate the proposed Body-in-the-Loop optimization techniques, we first established a ground truth of the cost landscape. To this end, we mapped subject’s energetic cost landscapes using a *steady state cost mapping* (SSCM) protocol similar to Felt et al. [43]. This SSCM protocol is a type of parameter study common in assistive robotics to brute force map  $x(p)$  [28, 33, 101].

The SSCM protocol that we implemented had subjects standing in place for four min-

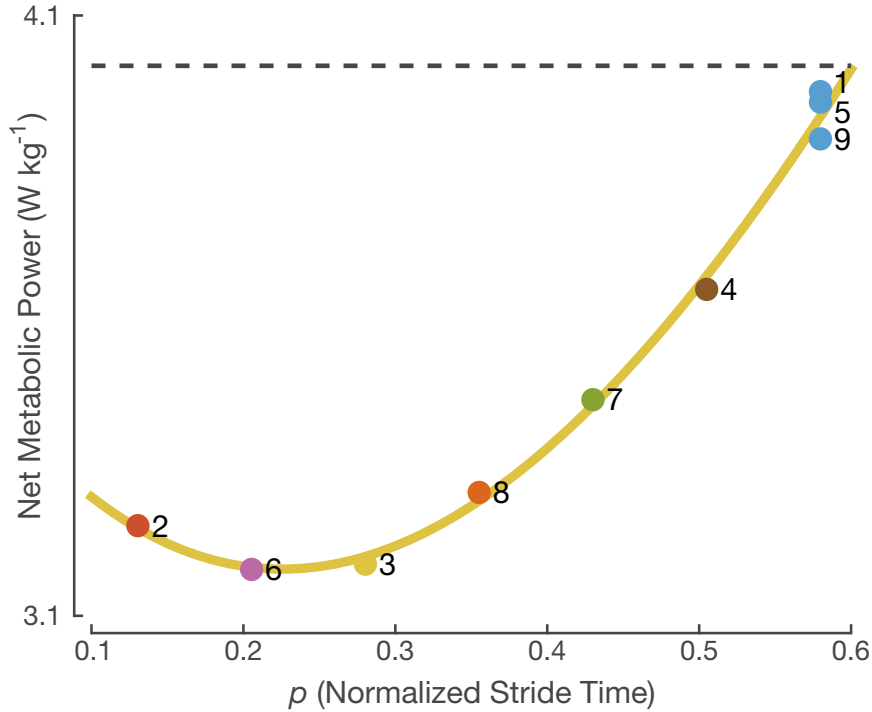


**Figure 3.5: Establishing a ground truth cost landscape to compare the optimized results to.**

To provide a ground truth for comparison, the cost landscape for each individual subject was found by averaging the final three minutes of metabolic data from each powered condition during a steady state cost mapping trial. Each average (shown here for a pilot subject) is represented by a colored dot and numbered according to the testing sequence. The subject’s standing metabolic power has been subtracted from all shown values. A third order polynomial was fit to these steady state values (shown in yellow). For comparison, the dashed line shows the subject’s metabolic power when walking in the unpowered exoskeletons. The highest parameter setting was repeated three times (1, 5, 9) to test for learning and fatigue effects.

utes to measure their standing metabolic effort. We then had subjects walk with the exoskeleton in an unpowered condition followed by nine powered conditions. Subjects walked for six minutes in each condition. This process was performed continuously where subjects were only given verbal warnings before starting the treadmill, powering on the exoskeletons, and powering off the exoskeletons. Subjects walked at seven different powered parameter settings ( $p = 0.13, 0.21, 0.28, 0.36, 0.43, 0.51, \text{ and } 0.58$ ) for nine different powered conditions. The first, fifth, and ninth powered conditions were always  $p = 0.58$ . All intermediate powered conditions were randomized. The repeated  $p = 0.58$  allowed us to analyze learning effects and fatigue in subjects. If we saw significant differences in the first, fifth, and ninth parameter’s steady state values, we could assume that the subject was still learning and adapting to the device, or that they were becoming fatigued. We chose the parameter of  $p = 0.58$  for this repetition, because this setting turns actuation on for

the shortest amount of time. Since  $S_{TO} \approx 0.63$  [101], the device was only powered for  $\sim 60$  ms at this setting. By starting and ending with this parameter setting, we were able to ease subjects in and out of powered conditions in the smoothest and safest way possible.

After data collection, we averaged the final three minutes of data from each powered condition in the SSCM data set to generate an estimate of the instantaneous energetic cost,  $\bar{x}(p)$ . In the realm of assistive devices, it is common practice to estimate  $\bar{x}(p)$  with a third order polynomial fit [33, 65, 101]. This representation of  $\bar{x}(p)$  versus  $p$  is shown in Figure 3.5.

### 3.4.2 Online Optimization

---

#### Algorithm: Body-in-the-Loop Optimization

---

**Data:** Respiratory measurements of metabolic power,  $\hat{y}$

**Result:** Minimizing  $x(p)$

**Initialize:**

$f = 0$

$n_0 = 0$

$n_1$  = initial number of respiratory measurements to evaluate

$p^1$  = initial guess of the optimal  $p$

**while**  $t < t_{end}$  **do**

**for**  $i = (n_f + 1) : n_{f+1}$  **do**

$$p_i = \begin{cases} p^k - (-1)^{f_c} & i \leq \frac{n_{f+1} + 2n_f}{3} \\ p^k + (-1)^{f_c} & i > \frac{2n_{f+1} + n_f}{3} \\ p^k & \text{otherwise} \end{cases}$$

  Collect corresponding  $\hat{y}_i$

  Calculate best linear fit,  $\bar{x}(\lambda_{(1)}^*, p)$ , from measurements  $i = 1 : n_{f+1}$

  Compute Akaike weight,  $w_1$

**if**  $w_1 > w_{thresh}$  **then**

    Set  $f = 0$

$p^{k+1} = p^k - \alpha^k \nabla \bar{x}(\lambda_{(1)}^*, p)$

**else**

    Set  $f = f + 1$

    Define  $n_{f+1} = n_1(1 + \delta f) + n_f$

Our proposed online optimization scheme is based upon gradient descent methods [13]. We allowed the algorithm to run for a set amount of time ( $t_{end}$ ) during which it was fully autonomous meaning there was no human intervention once the algorithm had begun. An

overview of our algorithm is presented above as pseudo-code with the variables defined in the proceeding subsections.

### 3.4.2.1 Parameter Exploration about $p^k$

To obtain an estimate of the gradient of the physiological objective at  $p^k$ , we systematically explored parameter settings surrounding  $p^k$ . We did this by initially evaluating below, at, and above  $p^k$  for a total of  $n_1$  breaths. If we were not confident in the gradient estimate of  $p^k$  after  $n_1$  breaths (ie it failed a statistical test of confidence) more data was collected. In these additional evaluations we collected data about  $p^k$  in the reverse order of the previous exploration for a total of  $n_1(1 + \delta f)$  more breaths. The variable  $f$  counted the number of evaluations, and a larger number of breaths was collected in each subsequent evaluation. We reevaluated the gradient for all measurements collected about  $p^k$  and repeated as necessary.

This oscillatory sampling pattern about  $p^k$  was defined as follows such that  $n_f$  and  $n_{f+1}$  were breath numbers,  $i$  was the breath count at  $p^k$ ,  $c$  was the perturbation size, and  $f$  was the number of failed statistical tests at  $p^k$ .

$$p_i = \begin{cases} p^k - (-1)^f c & i \leq \frac{n_{f+1} + 2n_f}{3} \\ p^k + (-1)^f c & i > \frac{2n_{f+1} + n_f}{3} \\ p^k & \text{otherwise} \end{cases} \quad (3.2)$$

We initialized  $n_0$ ,  $n_1$ ,  $f$ , and  $p^1$  before the algorithm began.  $n_1$  was a user defined input for the initial number of respiratory measurements to consider per oscillation and  $p^1$  was an initial guess of the optimal  $p$  location. If the gradient fit failed a statistical test of confidence then we incremented  $f$  and calculated  $n_{f+1}$  as

$$n_{f+1} = n_1(1 + \delta f) + n_f \quad (3.3)$$

where  $\delta$  represents a user defined growth factor.

### 3.4.2.2 Gradient Estimate

Based on the measurements  $y_i$  at the known parameter settings  $p_i$ , we estimated a linear representation of  $x(p)$  and extracted the gradient from this representation. This linear representation was defined by a set of coefficients  $\lambda$ .

$$\bar{x}(\lambda_{(1)}, p) = \lambda_0 + \lambda_1 p \quad (3.4)$$

In this notation, the gradient of the linear function,  $\nabla \bar{x}(\boldsymbol{\lambda}_{(1)}, p)$ , is simply  $\lambda_1$ . By running this linear approximation through Eq. (3.1), we produce an estimate of metabolic effort  $\bar{y}_i$  as a function of  $\boldsymbol{\lambda}$  and  $p_i$ :

$$\bar{y}_i = \left(1 - \frac{h_i}{\tau}\right) \bar{y}_{(i-1)} + \frac{h_i}{\tau} \bar{x}(\boldsymbol{\lambda}_{(1)}, p_i). \quad (3.5)$$

Starting from an initial value  $\bar{y}_1$ , the series of estimated breath measurements  $\bar{y}_i$  can be obtained by recursively evaluating Eq. (3.5). The resulting expression is linear with respect to a  $\bar{y}_1$  and  $\boldsymbol{\lambda}$ :

$$\begin{pmatrix} \bar{y}_1 \\ \vdots \\ \bar{y}_n \end{pmatrix} = \mathbf{A} \begin{pmatrix} \bar{y}_1 \\ \lambda_0 \\ \lambda_1 \end{pmatrix}. \quad (3.6)$$

$\mathbf{A}$  is a  $n \times 3$  matrix whose elements are calculated recursively based upon  $\tau$ ,  $h_i$ , and  $p_i$  [43].

$$\mathbf{A}_{i,j} = \begin{cases} 1 & i = 1, j = 1 \\ 0 & i = 1, j > 1 \\ \mathbf{A}_{i-1,j} \left(1 - \frac{h_i}{\tau}\right) & i > 1, j = 1 \\ \mathbf{A}_{i-1,j} \left(1 - \frac{h_i}{\tau}\right) + \frac{h_i}{\tau} \frac{\partial \bar{x}(\boldsymbol{\lambda}_{(1)}, p_i)}{\partial \lambda_{j-2}} & i > 1, j > 1 \end{cases} \quad (3.7)$$

For a given set of breath measurements  $\hat{y}_i$ , we employ the pseudo-inverse of  $\mathbf{A}$  (denoted as  $\mathbf{A}^+$ ) to solve for the optimal initial breath,  $\bar{y}_1^*$ , and optimal linear fit,  $\boldsymbol{\lambda}_{(1)}^*$ , that yield a least-square fit between  $\hat{y}_i$  and  $\bar{y}_i$ :

$$\begin{pmatrix} \bar{y}_1^* \\ \lambda_0^* \\ \lambda_1^* \end{pmatrix} = \mathbf{A}^+ \begin{pmatrix} \hat{y}_1 \\ \vdots \\ \hat{y}_n \end{pmatrix}. \quad (3.8)$$

That is, we identified model coefficients that provide a best fit between the linear model  $\bar{x}(\boldsymbol{\lambda}_{(1)}, p)$  and the true underlying relationship  $x(p)$ . Through this process, a new gradient  $\nabla \bar{x}(\boldsymbol{\lambda}_{(1)}, p)$  was established every time a total of  $n_{f+1}$  measurements had been taken about  $p^k$ .

In addition to fitting a linear model (as per Eq. (3.8)), we used the same process to simultaneously identify a purely constant (zeroth order) model,  $\bar{x}(\lambda_{(0)}, p)$ :

$$\bar{x}(\lambda_{(0)}, p) = \lambda_0. \quad (3.9)$$

We used this model to evaluate confidence in the gradient fit. In this model  $\mathbf{A}$  was a  $n \times 2$  matrix.

### 3.4.2.3 Confidence in the Gradient

Due to the poor signal to noise ratio of respiratory measurements, we implemented a statistical test to evaluate how confident we were in any given linear fit prior to acting upon it in the gradient descent algorithm. To this end, we compared the optimal first order fit to data about  $p^k$  to the optimal zeroth order fit to the same data. If the first order fit was statistically better at describing the data than the zeroth order fit (that is, when a gradient fit the data better than a flat line) the gradient was used to update  $p^k$ . The implemented statistical test used Akaike weights and a user defined threshold to establish confidence in a gradient estimate. From simulations of the Body-in-the-Loop optimization, we found this method to be more conservative in nature compared to other statistical tests.

The Akaike Information Criterion,  $AIC_l$ , is a measure used when comparing model  $l$  to multiple other model fits and is meant to determine which model in a given set is the best fit [2, 22]. In this framework,  $AIC_l$  can be calculated as

$$AIC_l = n_{f+1} \ln \left( \frac{e_l}{n_{f+1}} \right) + 2(m + 1). \quad (3.10)$$

where  $e$  is the sum of squared error between  $\bar{y}$  and  $\hat{y}$  (defined in Eq. (3.14)), and  $m$  is the number of elements of  $\lambda$ . By traditional standards, the lowest  $AIC_l$  value from the set of models,  $\min AIC$ , is the best model fit of the group; however, the  $\min AIC$  value alone does not give a sense as to how much better the best fit truly is. We used Akaike weights,  $w_l$ , to give us a sense of confidence in the model fits.  $w_l$  can range from 0 to 1 and can be interpreted as the probability that model  $l$  is the best model within a group of  $R$  total model fits [22, 23].  $w_l$  is defined as

$$w_l = \frac{\exp \{-0.5\Delta_l\}}{\sum_{r=1}^R \exp \{-0.5\Delta_r\}} \quad (3.11)$$

where  $\Delta_l = AIC_l - \min AIC$ .

In the described optimization scheme we used the Akaike weights to compare a first order fit,  $\bar{x}(\lambda_{(1)}^*, p)$ , to a zeroth order fit,  $\bar{x}(\lambda_{(0)}^*, p)$ , meaning  $R = 2$  in Eq. (3.11). Only if the Akaike weight associated with  $\bar{x}(\lambda_{(1)}^*, p)$ ,  $w_1$ , was greater than a user defined threshold,  $w_{thresh}$ , the gradient descent algorithm took a step. Otherwise, more data was collected at the current parameter setting  $p^k$ .

#### 3.4.2.4 Updating $p^k$

If  $w_1 > w_{thresh}$  then the evaluation parameter was updated as

$$p^{k+1} = p^k - \alpha^k \nabla \bar{x} (\lambda_{(1)}^* \cdot p). \quad (3.12)$$

In this equation,  $\alpha^k$  is a scheduling gain [13,43] defined as

$$\alpha^k = \frac{A_0 \alpha_0}{A_0 + k\gamma}. \quad (3.13)$$

where  $\alpha_0$ ,  $A_0$ , and  $\gamma$  are user defined constants with  $\gamma = (0, 1]$ .  $k$  was only incremented if a step was taken at which point  $f$  was set to zero. If  $w_1 \leq w_{thresh}$ , then no step was taken and  $f$  was incremented while  $k$  remained constant.

### 3.4.3 Implementation

The presented optimization algorithm was implemented in Python. The Python scripts took in measures of  $\hat{y}_i$  and communicated  $p_i$  values via serial connection to a real-time control board (dSPACE, Inc., Northville, MI) that ran the control loop described in Section 3.2.2. This real-time control board also received measures of vertical ground reaction force from the instrumented treadmill and determined instances of heel strike or toe off. Based on these gait events, the controller calculated appropriate actuation control signals and sent them to the pressure valves. The valves regulated the pressurized artificial pneumatic muscles proportional to the received control signals. A list of parameter values used during actual data collection can be found in Table 3.1. We chose these values based upon simulation results of the optimization routine. These simulations assumed a Gaussian distribution in respiratory measurement noise, an average metabolic time constant, and a hypothetical physiological objective function. For safety reasons, we bound  $p^k$  between 0.21 and 0.50 in implementation, yet these limits were never needed to be enforced during actual subject testing.

An important parameter in the algorithm is the time constant  $\tau$  of the metabolic dynamics. There are a number of ways to estimate  $\tau$ , and it was shown in prior work that it could simply be approximated by a constant value of 40 seconds [43]. For this work, we chose to use the SSCM data to estimate subject specific estimates of  $\tau$  as this data was readily available. We averaged the final three minutes of each powered condition to establish a breath dependent estimate of the instantaneous metabolic cost,  $\bar{x}(p_i)$ . Using  $\bar{x}(p_i)$  and Eq. (3.1), we estimated metabolic cost for a given  $\tau$  and  $\bar{y}_1$ . Constraining  $\tau$  and  $\bar{y}_1$  to

**Table 3.1:** Variables used in the Body-in-the-Loop optimization

Variable	Definition	Units	Value
$t_{end}$	Termination Time	Minutes	50
$c$	Perturbation Size	-	0.08
$n_1$	Initial Breath Evaluation Size	Breaths	90
$p^1$	Initial Evaluation Parameter	-	Randomized
$\delta$	Evaluation Growth Factor	-	0.5
$w_{thresh}$	Akaike Weight Threshold	-	0.7
$A_0$	Gain Scheduling Parameter	-	1
$\alpha_0$	Gain Scheduling Parameter	$\frac{1}{Wkg^{-1}}$	500
$\gamma$	Gain Scheduling Parameter	-	0.75

positive values, we used MATLAB’s Optimization Toolbox (The MathWorks, Inc., Natick, MA) to determine the  $\tau$  and  $\bar{y}_1$  that resulted in the smallest sum of squared error between actual metabolic measurements,  $\hat{y}_i$ , and estimated metabolic measurements,  $\bar{y}_i$ . That is to say,

$$\min_{\tau, \bar{y}_1} e = \sum_{i=1}^n (\hat{y}_i - \bar{y}_i)^2. \quad (3.14)$$

We only used powered condition data for this fit beginning from the steady state of the first parameter as shown in Figure 3.6. An example of the optimization being performed with this subject specific  $\tau$  and the variable values presented in Table 3.1 is shown in Figure 3.7.

### 3.5 Experimental Evaluation

To validate the Body-in-the-Loop optimization techniques, we tested the presented algorithm on healthy subjects wearing the bilateral ankle exoskeletons described in Section 3.2. All testing was in accordance to the University of Michigan’s Medical School’s Institutional Review Board (HUM00070022), and all subjects gave informed written consent to participate in the study prior to testing.

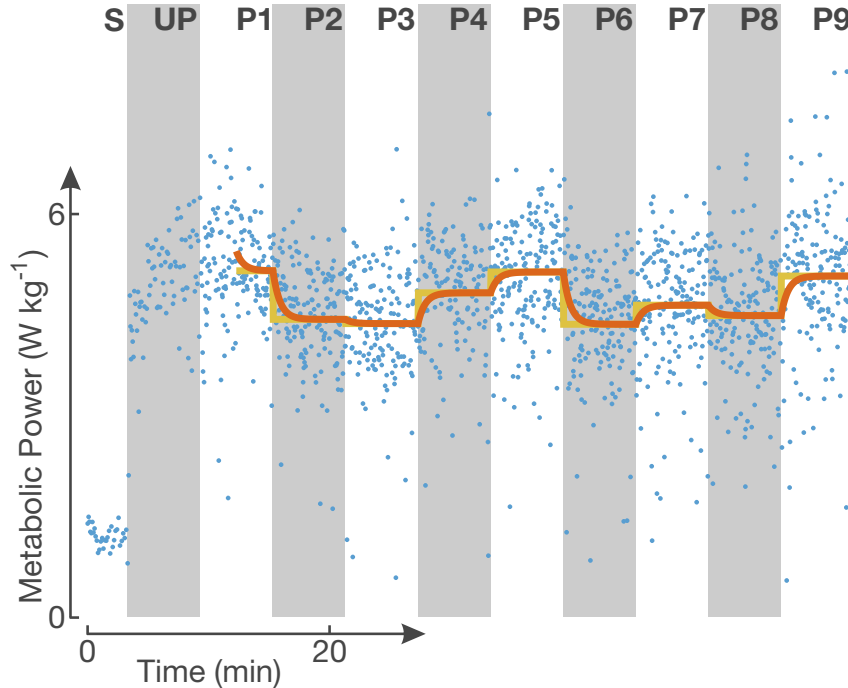


**Figure 3.6: Fitting subject specific  $\tau$  values.** We used the SSCM data to estimate subject specific  $\tau$ 's. The raw metabolic data ( $\hat{y}_i$ ) is shown in blue, the instantaneous metabolic cost ( $\bar{x}(p_i)$ ) is shown in yellow, and the metabolic estimate ( $\bar{y}_i$ ) is shown in orange. During the SSCM we recorded standing metabolics from the subject for four minutes (S), unpowered walking in the device for six minutes (UP), and nine different powered conditions for six minutes each (P1-P9). The data shown here is from a pilot subject that had a metabolic time constant of 36.6 seconds. This graph also illustrates the sparse data and high noise levels that are typical for respiratory measurements.

### 3.5.1 Experimental Protocol

We tested the proposed optimization techniques on nine healthy participants. Of these nine participants, four had never walked in a powered exoskeleton before. Only male participants were tested due to the large shoe size requirement of the exoskeleton design. One subject (Subject 2) was deemed an outlier due to inexplicably noisy respiratory measurements (a signal to noise ratio  $\sim 2$ ). The eight remaining subjects presented here (age:  $23 \pm 6$  years; body mass:  $72.2 \pm 5.3$  kg; height:  $179.4 \pm 7.7$  cm; mean  $\pm$  SD) walked in bilateral robotic ankle exoskeletons during three separate testing days.

On the first two days of testing, we performed the SSCM protocol explained in Section 3.4.1 to establish subject specific ground truths. Day one was used as a training day for subjects to learn and adapt to walking in the device. The data from day one has therefore been disregarded in this analysis. We used the SSCM data from the second day to establish a ground truth and to estimate subjects' time constants  $\tau$ . All differences in steady

state metabolic measurements of the repeated first, fifth, and ninth parameters were within the expected levels of measurement noise. On the third day of testing, we tested the proposed optimization scheme on each subject starting from a randomized start position,  $p^1$ . The optimization algorithm was run for 50 minutes before terminating. All walking took place on a split belt treadmill (Bertec Corporation, Columbus, OH) at  $1.2 \text{ ms}^{-1}$  and all measurements of metabolic effort were taken using a portable open-circuit indirect spirometry system (CareFusion Oxycon Mobile, Hoechberg, Germany).

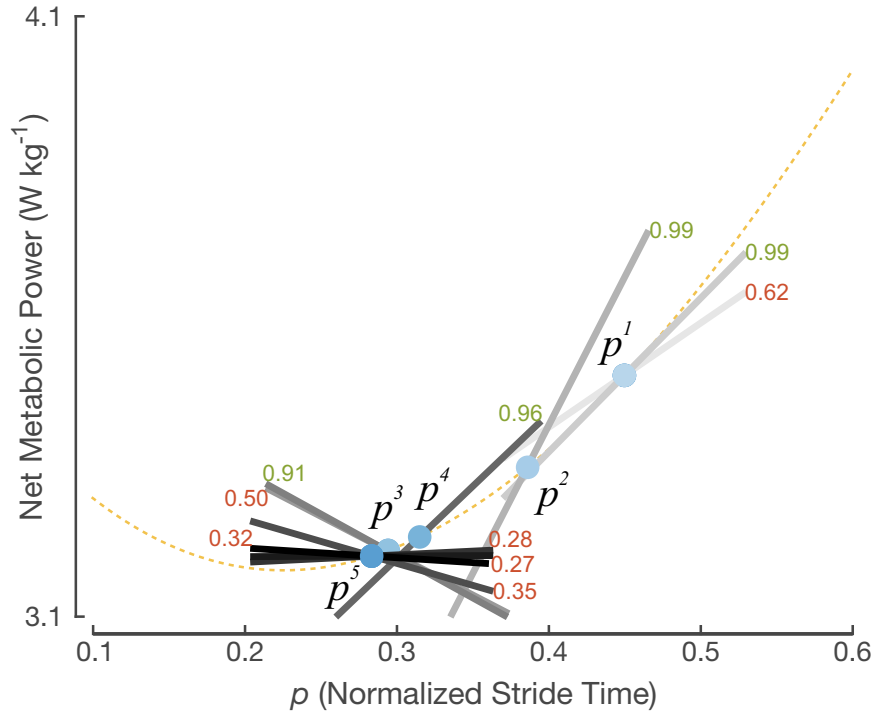


**Figure 3.7: A single representative subject’s optimization trial with the gradient descent algorithm.** Here is an example of a gradient based online optimization run that was started from  $p = 0.45$ . The presented data is from the same pilot subject as the data in Figures 3.5 and 3.6. Gradient estimates darken to represent progress through the optimization routine. The gradients are overlaid on the ground truth for visualization purposes.  $w_1$  values that correspond to the confidence in a gradient estimate are written touching their corresponding fits with green representing  $w_1 > w_{thresh}$  and red representing  $w_1 \leq w_{thresh}$ . In this particular case the optimizer finished at  $p = 0.28$  where the minimum identified from the SSCM was  $p = 0.23$ . According to the SSCM polynomial fit, this error resulted in an increase of  $0.023 \text{ W kg}^{-1}$  in metabolic power for this pilot subject.

### 3.5.2 Results

Table 3.2 shows the average results from all eight subjects. On average our optimization techniques terminated at a parameter setting 0.097 away from the optimal parameter setting

identified from the SSCM protocol. According to the established subject specific ground truth curves, this parameter error would result in an average increase of  $0.056 \text{ W kg}^{-1}$  in metabolic power. This increase is well within the range of sensor noise for respiratory measurements. However, to put this increase of  $0.056 \text{ W kg}^{-1}$  into perspective, subjects experienced a  $0.80 \pm 0.18 \text{ W kg}^{-1}$  (mean $\pm$ SD) decrease in metabolic power between the maximum and minimum values of the established ground truth curves. This accounts for an average reduction of  $19.6 \pm 3.2\%$ . In comparison, the parameters found by the optimizer resulted in an average reduction of  $18.0 \pm 4.6\%$  in accordance to the established ground truth curves.

**Table 3.2:** Average results from the Body-in-the-Loop optimization

	<b>Mean</b>	<b>Standard Deviation</b>
<b>Time Constant <math>\tau</math> (Seconds)</b>	47.8	$\pm 12.4$
<b>Absolute Error in Minimum <math>p</math> (Unitless)</b>	0.097	$\pm 0.077$

### 3.6 Discussion & Conclusion

The experimental work presented in this paper shows that Body-in-the-Loop optimization can be a viable tool in the development and tuning of controllers for assistive robotic devices. For all subjects, the presented algorithm was able to autonomously minimize a physiological objective function in real-time. The key novelty in this context was that the optimization was based on *physiological* measurements of human effort. These are measurements that provided direct and objective feedback about the performance of the assistive device. From the perspective of a roboticist, this is a radically new way of human-robot-interaction. This interaction was neither based on a physical exchange between the robot and the user through forces and velocities (which are, however, used in the controller of the exoskeleton) nor was it based on the exchange of information through a designated user interface or a neuro-interface. Instead, the proposed methods allowed a robot to directly react to the physiological state of the user, a state which may not always be obvious or may not even be consciously known to the users themselves. With the development of more unobtrusive sensing technologies, such as skin conductance, heart rate, oxygen saturation, etc., this will allow a continuous and seamless adaptation of robots to their users. While the methods presented in this paper have focused on metabolic effort as the objective function, other physiological states might prove interesting candidates for optimization. This includes pain, comfort, training effort, and others. Of course, there is an even greater challenge of quantifying these states than of measuring metabolic effort.

Additionally, the proposed Body-in-the-Loop optimization techniques allow for parameter exploration of actuation shapes that may not be considered using traditional shaping methods. Currently, researchers shape actuation profiles of assistive devices to match actuation profiles of healthy, unassisted joints [61]. However, it has been shown that when using an adaptive controller, subjects may drive the controller adaptation to use abnormal actuation profiles that still appear to minimize a physiological objective [89]. Due to the inherent parameter exploration of optimization, Body-in-the-Loop optimization could potentially find optimal actuation shapes that may be disregarded by traditional shaping methods because they do not resemble healthy joint actuation profiles.

We fully acknowledge that at this stage, the presented concept of Body-in-the-Loop optimization is still limited. For one, the model we used to estimate metabolic effort combines any time constants associated with learning effects with the estimated time constant of the subject's metabolic system,  $\tau$ . For this initial study we felt that modeling learning effects would over complicate the methodology, so we attempted to wash out any learning effects by training subjects on the assistive devices for an adequate amount of time prior to data collection (day one of testing) [52]. Also, at this point the proposed sensor choice to estimate the physiological objective of metabolic effort from respiratory measurements is not practical for daily use outside of the lab setting. For Body-in-the-Loop optimization to be applicable for continuous use on assistive robotics, more discrete and transparent sensors and estimation methods need to be developed. Furthermore, we assessed the metabolic effort under deterministic conditions, being that subjects were walking with constant speed and on level ground. This ensured that changes in metabolic effort were strictly related to changes in the timing parameter. For the proposed methods to work outside the laboratory, we will have to extend the algorithms to control for any changes in the subjects locomotion pattern that might influence the physiological cost function. Such disturbances (such as varying walking speed or ground slope) must be either detected and compensated for, or data must be averaged over longer periods of time. Lastly, the devices used in this study are not an accurate representation of the current state of the art in ankle exoskeletons [101, 106]. Our devices were tethered to an air supply which constrained them to only being used in a lab setting. Also, these exoskeletons were bulkier and heavier than the current state of the art, resulting in a larger increase in metabolic effort when comparing unpowered walking in the exoskeletons to walking with no exoskeletons at all. From pilot data, we saw that our exoskeleton design can reduce metabolic effort slightly below that of walking without the device when at an optimal parameter setting, yet this reduction was small. However, these exoskeletons were solely meant to perform as a platform to test the Body-in-the-Loop optimization techniques on and they greatly served that purpose.

Though we have validated that Body-in-the-Loop optimization is a viable option for the control of assistive robotic devices, we have only scratched the surface on the possible applications. We plan to expand upon the presented techniques to include alternative physiological objectives and sensing techniques to allow for discrete and continuous optimization during daily routines. Additionally, we plan to expand the techniques to include multidimensional optimization as most assistive devices can have upwards of ten shaping parameters [1]. This expansion into multidimensional space could have major implications to the field as the time required for brute force mapping of physiological objective functions grows exponentially with increased dimensionality.

## CHAPTER 4

# An Adaptive Gain Proportional Myoelectric Controller for a Robotic Ankle Exoskeleton

### 4.1 Background

In order to achieve optimal assistance, the controller of an active prosthetic or orthotic device must accomplish three tasks. It must reliably determine the user's *intent*, precisely coordinate the *timing* of assistance with the user, and provide actuation profiles of a suitable *shape*. Only if the controller succeeds in all three tasks, the robotic device can achieve its assistive goal. For example, many robotic assistive devices aim to minimize the energetic cost for the user to perform a given task. Any amount of error in the controller's intent recognition, timing, or actuation shape can result in motion that is energetically costly, unnatural, or potentially dangerous for the user [38].

Without direct access to the human nervous system, many lower-limb assistive robotic devices detect intent and timing from estimates of the user's motion. These measurements are called *mechanically intrinsic* as they are taken from the mechanical device itself. These measurements are used to estimate intent and trigger the timing of predefined actuation profiles whose shapes correspond to estimates of intended motion [79]. Controllers that rely on mechanically intrinsic measurements often use joint angles, impedances, gait events, or force measurements from the device to control actuation [10, 17, 69, 82, 97]. Recent exoskeleton controller designs relying on this type of sensing have shown promise in reducing the user's metabolic cost during walking [101, 106]. However, using mechanically intrinsic measurements for control has fundamental limitations. Because mechanically intrinsic measurements are outcomes of physical motion, they are prone to mechanical delays. The desired movement has already started by the time the controller senses it. This delay

---

The content of this chapter has been previously published in the Journal of NeuroEngineering and Rehabilitation [89].

can cause the control timing to lag behind the user and result in the user fighting the device [47]. Furthermore, the measurements are subject to complex interactions between the user’s musculoskeletal system and the mechanical structure of the device. If the combined human-machine dynamics are not well understood it can be difficult to reliably estimate intent. Additionally, it is impossible for the user to receive appropriate assistance for motion outside of the controller’s intent laws since all actuation profile shapes are predefined for specific movements.

The drawbacks of relying on mechanically intrinsic measurements can potentially be overcome by a direct access to the user’s nervous system. One approach using bioelectrical signals for control is proportional myoelectric control. A proportional myoelectric controller sends a control signal to the actuators that is proportional to the muscle recruitment of the user [46,68]. In these controllers muscle recruitment is measured using electromyography (EMG). The controller makes no assumptions about the human-machine dynamics because the measurements used to determine intent come straight from the user instead of the device. This puts the user in direct control of the exoskeleton and allows for intent recognition to be accurate and consistent. Additionally, proportional myoelectric control has the potential for zero lag in timing behind the user due to the electromechanical delay of EMG [30]. EMG signals are produced before muscle tension develops which allows a proportional myoelectric controller to have a buffer of time between sensor measurement and actuation. The control signal shape of these controllers is proportional to the user’s EMG signal meaning there is inherent human-machine synchronization. Additionally, this proportionality implies that the device is not limited to predefined actuation profiles. Our research group has shown that proportional myoelectric control is a viable control method for lower-limb robotic exoskeletons that produces a relatively natural and economical gait [59,60,80,81,86,116].

A proportional myoelectric control scheme can be illustrated as follows and is graphically represented by Figure 4.1. Suppose  $\mathbf{X}_{Tot}$  represents the total actuator activation at the assisted joint including both biological muscles and the exoskeleton’s mechanical actuators. When walking in an exoskeleton, we can apportion the activity from the biological joint as  $\mathbf{X}_{Bio}$  and the activity from the exoskeleton as  $\mathbf{X}_{Exo}$ . The biological activity can be thought of as muscle activity about the assisted joint measured via EMG and the exoskeleton activity can be thought of as the control signals being sent to the exoskeleton actuators.

$$\mathbf{X}_{Tot} = \mathbf{X}_{Bio} + \mathbf{X}_{Exo} \quad (4.1)$$

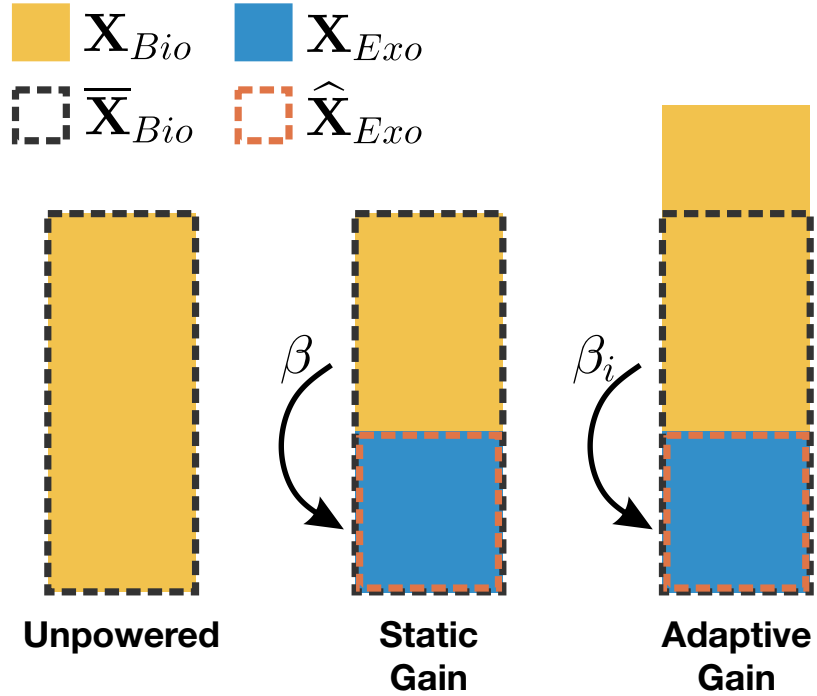


**Figure 4.1: Graphical representation of total ankle activity contributions with a proportional myoelectric controller.** The above figure is a graphical representation to compliment the mathematical theory that describes proportional myoelectric control. In all of the bar graphs,  $X_{Tot}$  is represented by the summation of  $X_{Bio}$  and  $X_{Exo}$ .

In a proportional myoelectric controller, the activity from the exoskeleton is proportional to the biological activity by some gain  $\beta$ .  $\beta$  maps biological activity to exoskeleton activity. This mapping is scaled by the ratio  $c = \hat{X}_{Exo}/\bar{X}_{Bio}$ , where  $\hat{X}_{Exo}$  is the maximum unsaturated exoskeleton activity and  $\bar{X}_{Bio}$  is the normal unassisted joint activity.

$$\mathbf{X}_{Exo} = \beta \left( \frac{\hat{X}_{Exo}}{\bar{X}_{Bio}} \right) \mathbf{X}_{Bio} = \beta \cdot c \cdot \mathbf{X}_{Bio} \quad (4.2)$$

The exoskeletons presented here and in our previous research can provide about half the power of the normal unassisted joint, so  $c$  has been estimated as  $c \approx 0.5$  [59, 116].

In the past, the proportional myoelectric controllers developed by our group created a control signal for actuation by using a *constant* gain of  $\beta = 2$  to map the EMG linear envelope to an actuation voltage. This gain was chosen with the assumption that during powered walking total joint activity should be equal to the unassisted joint activity:  $\mathbf{X}_{Tot} = \bar{X}_{Bio}$ . Additionally, this gain was meant to allow maximal assistance ( $\mathbf{X}_{Exo} = \hat{X}_{Exo}$ )

during steady state operation. With this, we got from Equation Eq. (4.1):

$$\bar{\mathbf{X}}_{Bio} = \mathbf{X}_{Bio} + \hat{\mathbf{X}}_{Exo} = \mathbf{X}_{Bio} + \bar{\mathbf{X}}_{Bio} \cdot c, \quad (4.3)$$

and thus a reduction in biological joint activity:  $\mathbf{X}_{Bio} = (1 - c) \bar{\mathbf{X}}_{Bio}$ . For  $\mathbf{X}_{Exo} = \hat{\mathbf{X}}_{Exo}$ , we can solve Equation Eq. (4.2) for the necessary  $\beta$ :

$$\beta = \frac{\bar{\mathbf{X}}_{Bio}}{\mathbf{X}_{Bio}} = \frac{1}{1 - c} = \frac{1}{1 - 0.5} = 2. \quad (4.4)$$

In previous work, this choice of  $\beta$  resulted in large reductions in metabolic cost. Our studies have also shown that subjects indeed attempted to adapt to  $\mathbf{X}_{Bio} \approx \frac{1}{\beta} \bar{\mathbf{X}}_{Bio}$ , in accordance with Equation Eq. (4.4) [116].

Yet walking in an exoskeleton is different than unassisted walking and we might prefer more or less total joint activity than  $\bar{\mathbf{X}}_{Bio}$ . In these previous studies, subjects had the ability to adapt  $\mathbf{X}_{Bio} < \frac{1}{\beta} \bar{\mathbf{X}}_{Bio}$  and deliberately chose not to. This result suggests that  $\mathbf{X}_{Tot} < \bar{\mathbf{X}}_{Bio}$  is not energetically economical since we generally adapt to move with as little energy as possible [3, 39, 48, 126, 133]. However, subjects were somehow constrained when attempting  $\mathbf{X}_{Bio} > \frac{1}{\beta} \bar{\mathbf{X}}_{Bio}$  as they would saturate the exoskeleton. Previous work has shown that subjects avoided this saturation limit, but we do not know the exact reason why. Perhaps subjects avoided saturation due to discomfort or possibly they chose to avoid the increased cognitive complexity that comes with learning a highly nonlinear task. Whatever the reason, we know that subjects naturally chose to avoid operating the exoskeleton within the saturation range. From Equation Eq. (4.2) it follows that

$$\mathbf{X}_{Exo} = \beta \left( \frac{\hat{\mathbf{X}}_{Exo}}{\bar{\mathbf{X}}_{Bio}} \right) \mathbf{X}_{Bio} > \hat{\mathbf{X}}_{Exo}, \text{ for } \mathbf{X}_{Bio} > \frac{1}{\beta} \bar{\mathbf{X}}_{Bio}, \quad (4.5)$$

so it is unclear whether  $\mathbf{X}_{Tot} = \bar{\mathbf{X}}_{Bio}$  is truly the optimal value, or if subjects would prefer a larger  $\mathbf{X}_{Tot}$  if saturation were avoidable.

Therefore, we saw the need for a proportional myoelectric controller that allows users to explore higher magnitudes of total joint activity. Such a controller would allow users to adapt to find the most energetically economical gait on their own. This adaptation could potentially answer whether or not  $\bar{\mathbf{X}}_{Bio}$  is the energetically optimal total joint activity for walking in an exoskeleton. In designing such a proportional myoelectric controller, we wanted to keep the exoskeleton performing at maximum potential regardless of biological activity (i.e.,  $\mathbf{X}_{Exo} = \hat{\mathbf{X}}_{Exo}$ ). This design would allow for the user to vary the total joint activity by just varying their biological activity. We made this possible by designing a

proportional myoelectric controller in which the gain was free to *dynamically* adapt on a stride by stride basis. In other words,  $\beta$  was no longer held constant but adapted itself on each stride  $i$  to maintain maximal exoskeleton output. If we set  $\mathbf{X}_{Exo} = \widehat{\mathbf{X}}_{Exo}$  in Equation Eq. (4.2), we can express  $\beta_i$  as follows:

$$\beta_i = \frac{\overline{\mathbf{X}}_{Bio}}{\mathbf{X}_{Bio,i}}. \quad (4.6)$$

Combining Equations Eq. (4.1), Eq. (4.2), and Eq. (4.6) shows that this adaptive proportional myoelectric controller could allow users to vary their amount of total joint activity:

$$\mathbf{X}_{Tot} = \frac{\overline{\mathbf{X}}_{Bio}}{\beta_i} + \widehat{\mathbf{X}}_{Exo}. \quad (4.7)$$

It is notable that lower gains  $\beta_i$  (a consequence of larger  $\mathbf{X}_{Bio,i}$ ) result in larger values for  $\mathbf{X}_{Tot}$ . A time series representation of this controller dynamically adapting to the user is shown in Additional file 1: Figure A1 of [89].

The purpose of this study was to test the performance of an adaptive proportional myoelectric controller on a robotic ankle exoskeleton. This controller allowed users to explore a greater possible parameter space of walking in an exoskeleton compared to walking with traditional proportional myoelectric controllers. We were interested in what  $\beta$  gain user's choose when provided an adaptive controller. We tested young healthy subjects walking with the adaptive gain proportional myoelectric controller on bilateral robotic ankle exoskeletons. We predicted that the adaptive controller would allow users to walk with reduced energetic cost and a  $\beta$  gain less than that of our previous work with a constant gain controller. A  $\beta$  gain less than that of our previous work would indicate that subjects have adapted to using more total ankle activity than that of unassisted walking.

## 4.2 Methods

### 4.2.1 Subjects

We tested eight healthy subjects for this study (male,  $21 \pm 1$  years,  $74.0 \pm 2.7$  kg,  $180.0 \pm 2.8$  cm; means  $\pm$  s.e.m.). All subjects were prescreened for exoskeleton hardware fit prior to testing. Subjects exhibited no gait abnormalities and had no prior experience walking in a powered exoskeleton. Prior to testing, all subjects gave informed written consent to participate in the study in accordance to the University of Michigan's Medical School's Institutional Review Board (HUM00070022).

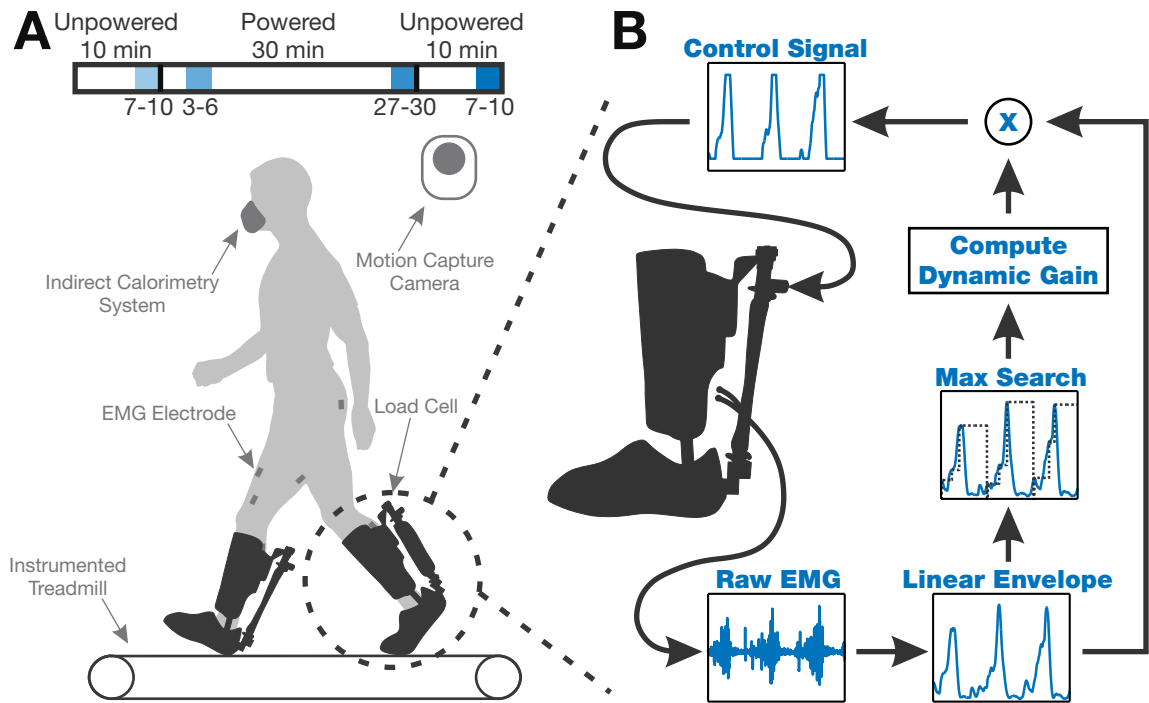


**Figure 4.2: Testing protocol and the adaptive proportional myoelectric controller.** (A) All eight subjects walked at  $1.2 \text{ ms}^{-1}$  with the exoskeletons on during three separate training sessions. Each session consisted of 50 minutes of walking where the first 10 minutes were unpowered, the following 30 minutes were powered, and the last 10 minutes were unpowered. Four time intervals from each session were analyzed in the analysis: minutes 7-10 of the 1<sup>st</sup> unpowered section, minutes 3-6 of the powered section, minutes 27-30 of the powered session, and minutes 7-10 of the 2<sup>nd</sup> unpowered section. (B) For control we processed the soleus linear envelope in real time and then conducted a maximum search on a stride by stride basis. We used these max values to calculate the mapping gain that the linear envelope was multiplied by to create the actuation control signal.

## 4.2.2 Exoskeleton Hardware

We custom fabricated bilateral ankle exoskeletons for this study similar to those used in previous studies from our research group [44,45,59,116]. The exoskeletons consisted of a shank component and a shoe component that were joined by a rotational joint. This joint constrained the exoskeleton motion to plantar flexion and dorsiflexion. The shank was made from stainless steel rods and plastic cuffs. The shoe was a standard orthotic shoe that was outfitted with attachments for actuation. The exoskeleton could accommodate subjects that wore between a 9 and 11 U.S. men’s shoe size.

We actuated the exoskeletons using custom built artificial pneumatic muscles attached posteriorly allowing for plantar flexion assistance when actuated [44]. We attached a load cell in series (Omega Engineering, Stamford, Connecticut) with the actuator to record ac-

tuation kinetics. The shoe, shank, actuator, and load cell combined to a total mass of 2.08 kg (approximately 0.81 kg at the foot and 1.27 kg at the shank).

### 4.2.3 Exoskeleton Control

The exoskeleton controller was a dynamically adaptive proportional myoelectric controller. We used the wearer’s soleus EMG for the input signal to the controller in order to maintain biological synergy with the exoskeleton.

We designed the controller to process the user’s raw soelus EMG into its linear envelope in real time. The processing consisted of a high-pass filter (2nd order Butterworth, cutoff frequency 80 Hz) to remove motion artifacts, followed by full wave rectification. We then low-pass filtered the rectified signal (2nd order Butterworth, cutoff frequency 4 Hz) to get the linear envelope. In a traditional proportional myoelectric controller, this linear envelope would then be multiplied by a static mapping gain to calculate the control signal [46, 68]. In the current study, this mapping gain was dynamically adjusted by the controller using the following methodology (Figure 4.2B).

For each stride  $i$ , we determined the maximum voltage of the linear envelope,  $x_i$ , in real time. We then calculated the gain,  $g_i$ , necessary for this value to reach a desired peak actuation voltage,  $V_{peak}$ .

$$g_i = \frac{V_{peak}}{x_i} \quad (4.8)$$

We calculated the dynamic gain,  $G_i$ , using a finite impulse response (FIR) filter with a tap size,  $N = 50$ , and unity weighting.  $G_i$  was then used to proportionally scale the EMG linear envelope to the actuation control signals.

$$G_i = \frac{1}{N} \left( \sum_{j=i-N}^{i-1} g_j \right) \quad (4.9)$$

The actuation control signals were sent to proportional pressure control valves (MAC Valves, Wixom, MI). These valves regulated the pressure in the artificial pneumatic muscles to be proportional to the user’s amplified linear envelope. This pressure roughly corresponded to the exoskeleton torque output with some nonlinearities induced by actuator dynamics and a changing moment arm. We ran our controller on a desktop and real-time control board (dSPACE, Inc., Northville, MI) during all testing. All software was composed in Simulink (The Mathworks, Inc., Natick, MA) and then converted to ControlDesk (dSPACE, Inc., Northville, MI) using commercial dSPACE software.

#### 4.2.4 Testing Protocol

The following protocol is largely adapted from [116]. All subjects participated in three identical training sessions with the device (sessions 1-3). We conducted these training sessions over the course of 7-14 days for each subject, allowing at least one day rest between sessions for motor consolidation [59, 121]. Each training session consisted of 50 continuous minutes of level ground walking in the exoskeleton. Subjects walked on a split belt treadmill at  $1.2 \text{ ms}^{-1}$  (Bertec Corporation, Columbus, OH) for all tests. The first 10 minutes of each walking session were with the device unpowered (i.e., no actuation). We gave subjects a verbal warning before actuation was turned on for the following 30 minutes. The FIR filter was initialized with zeros, so a peak control signal was not reached until 50 strides or approximately 60 seconds of powered walking. After the full 30 minutes of powered walking, we gave subjects a verbal warning before actuation was turned off for another 10 minutes.

We analyzed data from four time windows of each session: minutes 7-10 of the 1<sup>st</sup> unpowered condition, minutes 3-6 of the powered condition, minutes 27-30 of the powered condition, and minutes 7-10 of the 2<sup>nd</sup> unpowered condition (Figure 4.2A). Respiratory data was averaged over each three minute time window. Gait data was averaged over the last 25 strides of each time window. From this gait data, we calculated muscle recruitment, inverse kinematics, inverse dynamics, and exoskeleton mechanics. Strides were defined as heel-strike (0% gait cycle) to heel-strike (100% gait cycle). Data from all session's 1<sup>st</sup> unpowered condition were averaged to get the *Average Unpowered* values. These values are compared to data from the end of powered conditions of each session in Figures 4.4 through 4.8.

#### 4.2.5 Metabolic Cost

We used a portable open-circuit indirect spirometry system (CareFusion Oxycon Mobile, Hoechberg, Germany) to measure  $\text{O}_2$  and  $\text{CO}_2$  flow rates. We used formulas from Brockway [19] to convert these measurements to metabolic power. Prior to walking trials, we recorded a three minute standing trial from each subject. We averaged over these three minutes to get each subject's standing metabolic power which was then subtracted from each walking trial to calculate the net metabolic power of each walking condition [63]. We analyzed each walking condition by averaging the metabolic power over a three minute interval then normalizing it by the subjects body mass. During testing, we monitored each subject's respiratory exchange ratio (RER) to ensure that it remained in the aerobic range ( $\text{RER} < 1$ ) [20].

## 4.2.6 Electromyography

We measured electromyography from the soleus, tibialis anterior, medial gastrocnemius, biceps femoris long head, vastus lateralis, and rectus femoris. All EMG recordings came from the subject's right side except for the soleus in which recordings came from both the left and right since they were used as control inputs. We used bipolar surface electrodes (sample rate: 1000 Hz; Biometrics, Ladysmith, VA) with an inter-electrode distance of 2.0 cm and electrode diameter of 1.0 cm to record all muscle activity. The EMG amplifier used for data collection had a bandwidth of 20-460 Hz. We placed all electrodes according to the procedure of Winter and Yack [141].

For post-processing the EMG data, we high-pass filtered all EMG signals with a 35 Hz cut-off frequency (3rd order Butterworth filter, zero-lag) and then full-wave rectified. We then low-pass filtered all rectified signals with a 10 Hz cut-off frequency (3rd order Butterworth filter, zero lag) to achieve the signal's linear envelope. Each linear envelope was then epoched by stride (heel-strike to heel-strike) and averaged. We normalized each muscle's linear envelope by its corresponding peak voltage from the end of the 1<sup>st</sup> unpowered walking portion of the session [141]. We additionally calculated the root mean square (r.m.s.) stride average for the rectified EMG signal. The r.m.s. calculations were normalized by the average r.m.s. from the end of the 1<sup>st</sup> unpowered portion of each session. All EMG normalization was done prior to averaging.

## 4.2.7 Kinematics

We measured joint kinematics during treadmill walking using a 10-camera motion capture system (sample rate: 100 Hz; Vicon, Oxford, UK). We used a 39 reflective marker set for each subject (34 on the pelvis and lower limbs, 4 on the torso, and 1 on the head). All joint kinematics were calculated from raw marker data using OpenSim 3.2 [34]. In OpenSim we scaled a generic model to subject specific marker placements. The model consisted of lower extremities and a trunk with 23 degrees of freedom and 54 actuators. We ensured that all subject model scaling and inverse kinematic r.m.s. values were within the range recommend by OpenSim during processing [67].

We calculated the Pearson product moment correlations between the mean joint kinematics from the end of powered conditions to the end of 1<sup>st</sup> unpowered conditions. We assessed similarities in powered verses unpowered joint kinematics by the coefficient of determination ( $R^2$ ) of these correlations [59].

## 4.2.8 Joint Mechanics

We imported all ground reaction force data into OpenSim 3.2 to use in conjunction with the calculated joint kinematics to perform inverse dynamics. We scaled each model’s mass anthropomorphically using the subject’s mass and then manually included additional mass at the shank and foot to account for the exoskeleton. We used OpenSim’s residual reduction algorithm (RRA) to iteratively adjust the model as needed to get residual forces and moments as low as possible. We used the adjusted model to calculate inverse dynamics. Our final residuals after using the RRA can be seen in Table 4.1. These residuals are within OpenSim’s recommended ranges with the exception of  $F_y$  maximum and  $F_z$  root mean square which are marginally outside of the recommended ranges [67]. We believe these values are acceptable and we attribute the larger residuals to the added complexity of the exoskeleton being present in the analysis.

To calculate all joint powers, we multiplied joint angular velocities by the joint torque. We took a simple derivative of the joint positions to get the joint angular velocities and filtered them with a 25 Hz cut-off frequency (3rd order Butterworth, zero-lag) to remove the amplified noise that resulted from taking the derivative. We calculated biological ankle power by subtracting the exoskeleton power from the total ankle power at each time instance. We calculated average joint power values by taking the time interval of the power time series data and dividing it by corresponding stride periods [33, 42]. Average positive and negative power values were computed by separating out the time integrals to periods of positive and negative power. Average net power was calculated using the time series of all power data. Following methodology from [42], we assessed total average positive power,  $\bar{P}_{Tot}^+$ , as the sum of average positive power from the ankle, knee, and hip ( $\bar{P}_{Ankle}^+$ ,  $\bar{P}_{Knee}^+$ ,  $\bar{P}_{Hip}^+$ , respectively).

$$\bar{P}_{Tot}^+ = \bar{P}_{Ankle}^+ + \bar{P}_{Knee}^+ + \bar{P}_{Hip}^+ \quad (4.10)$$

**Table 4.1:** Average residual values after final run of the RRA in OpenSim

	$F_x$	$F_y$	$F_z$	$M_x$	$M_y$	$M_z$	pErr <sub>x</sub>	pErr <sub>y</sub>	pErr <sub>z</sub>
	(N)	(N)	(N)	(Nm)	(Nm)	(Nm)	(cm)	(cm)	(cm)
Maximum	12.9	33.3	17.4	29.3	40.6	40.6	3.8	2.3	0.4
Root Mean Square	7.4	9.6	11.1	9.8	19.3	11.1	2.6	1.5	0.2

$F_x$ ,  $F_y$ , and  $F_z$  refer to the residual forces at the pelvis.  $M_x$ ,  $M_y$ , and  $M_z$  refer to the residual moments at the pelvis. pErr<sub>x</sub>, pErr<sub>y</sub>, and pErr<sub>z</sub> refer to the translational position error of the markers.

## 4.2.9 Exoskeleton Mechanics

The distance from the base of the actuator attachment to the exoskeleton joint center was 10.07 cm. Knowing the ankle joint angle from the inverse kinematics, we calculated the moment arm on the actuator at each time instance of collection. We filtered all load cell data with a 25 Hz cut-off frequency (3rd order Butterworth filter, zero-lag). We multiplied the filtered force data by the calculated moment arm to get the exoskeleton torques. The calculated exoskeleton torques were multiplied by the ankle angular velocities to calculate the exoskeleton power. We calculated average exoskeleton power values the same way as average joint power values. We calculated exoskeleton mechanics from one exoskeleton per subject.

## 4.2.10 Statistical Analyses

We performed two types of repeated-measures ANOVA analysis using SPSS Statistics 22 (IBM, Armock, NY) on all data of interest with a significance level set to 0.05. One ANOVA analysis compared across the four time windows of each training session. Another ANOVA analysis compared across the training sessions of each time window.

## 4.3 Results

### 4.3.1 Metabolic Cost

As subjects began to adapt to the exoskeleton, the amount of metabolic power required to walk in the device decreased (Figure 4.3). Subjects had a significant decrease in metabolic

**Table 4.2:** Resulting net metabolic cost from each time interval across sessions

	1 <sup>st</sup> Unpowered Minutes 7-10 ■	Powered Minutes 3-6 ■	Powered Minutes 27-30 ■	2 <sup>nd</sup> Unpowered Minutes 7-10 ■	Within Session <i>P</i> -Value
Session 1	3.94 ± 0.25	3.72 ± 0.18	3.30 ± 0.15	3.86 ± 0.24	0.002
Session 2	3.75 ± 0.18	3.31 ± 0.19	3.08 ± 0.14	3.75 ± 0.20	0.024
Session 3	3.66 ± 0.18	3.14 ± 0.11	3.01 ± 0.08	3.74 ± 0.15	0.006
Across Session <i>P</i> -Value	0.070	0.028	0.193	0.614	—

Net metabolic rates are all expressed in units of  $W\ kg^{-1}$  (mean ± s.e.m.).  $P < 0.05$  represents statistical significance.

power in every session (all  $P < 0.05$ ). By the end of powered walking in session 3, subjects were able to walk with a net metabolic power of  $3.01 \pm 0.08 \text{ W kg}^{-1}$  (mean  $\pm$  s.e.m., here and throughout). Compared to the first unpowered condition of that same session,  $3.66 \pm 0.18 \text{ W kg}^{-1}$ , this was a reduction of 17.8%. All net metabolic power values are listed in Table 4.2.

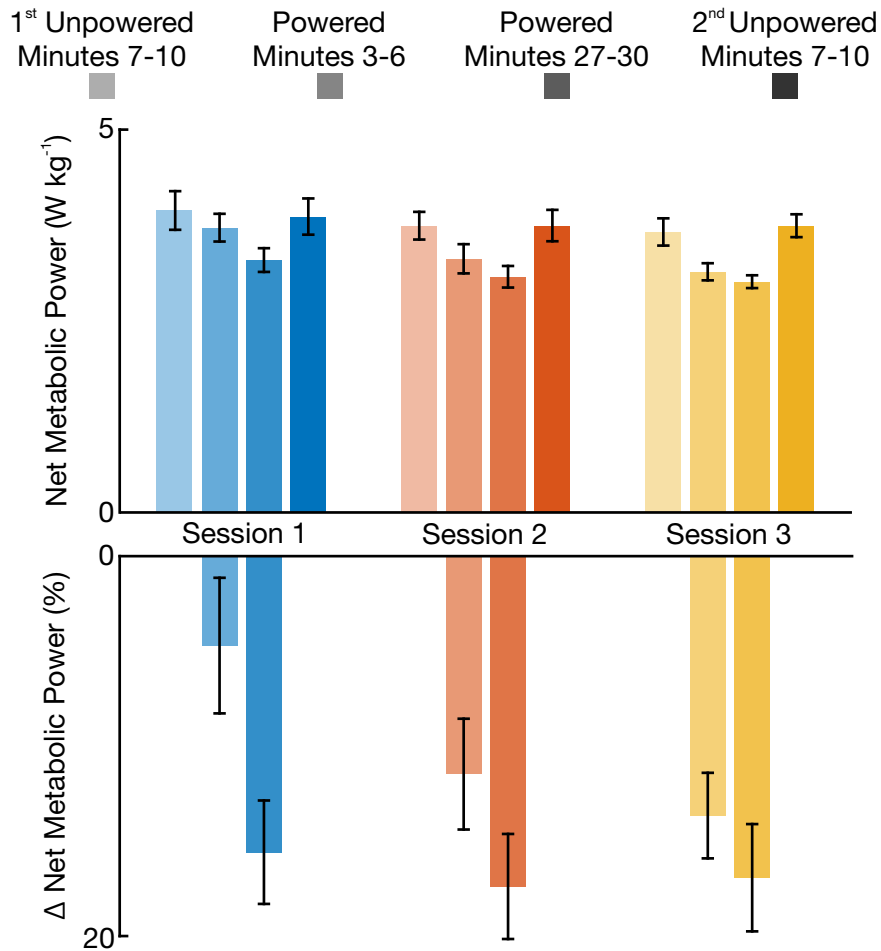


**Figure 4.3: Metabolic results from each training session.** The top axis shows the mean net metabolic power required by eight subjects to walk in the exoskeleton across the three training sessions. All net metabolic power values are normalized by subject mass. The bottom axis represents the powered conditions of this same data as a mean percent change in net metabolic power. Error bars represent  $\pm 1$  s.e.m.

There was a large change in metabolic power during powered minutes 3-6 across sessions. During session 1, subjects had a net metabolic power of  $3.72 \pm 0.18 \text{ W kg}^{-1}$ , a reduction of 5.6% compared to the 1<sup>st</sup> unpowered condition. By session 3, net metabolic power was  $3.14 \pm 0.11 \text{ W kg}^{-1}$ , a reduction of 14.2% compared to the 1<sup>st</sup> unpowered condition. Statistically, there was a significant reduction in net metabolic power during powered

minutes 3-6 across the three sessions ( $P=0.028$ ).

### 4.3.2 Dynamically Adjusted Gain

By the end of session 3, our adaptive controller chose gains that resulted in  $\beta = 1.50 \pm 0.14$  (mean  $\pm$  s.e.m. between subjects; we averaged  $\beta_i$  over the final three minutes of the powered session to calculate  $\beta$ ). The average gain values from the final three minutes of each session showed no significant difference across sessions ( $P=0.273$ ).

### 4.3.3 Electromyography

During session 1, subjects quickly reduced their soleus activation levels (Figure 4.4 and Additional file 2: Table A2 of [89]). At the beginning of the powered condition of session 1, subjects reduced their soleus r.m.s. EMG by  $13.8 \pm 3.8\%$  compared to the end of the 1<sup>st</sup> unpowered condition. By the end of that same session, subjects had achieved a soleus r.m.s. EMG reduction of  $20.3 \pm 8.2\%$  ( $28.0 \pm 6.8\%$  reduction in peak linear envelope). Contrary to previous studies, subjects preferred to increase their soleus recruitment with additional training sessions. By the end of session 3, subjects were walking with a soleus r.m.s. EMG reduction of only  $10.8 \pm 7.9\%$  ( $21.5 \pm 4.8\%$  reduction in peak linear envelope). The medial gastrocnemius EMG showed no significant change during testing.

Across testing sessions, subjects adapted to use less rectus femoris recruitment when walking in the powered exoskeleton (Figure 4.4 and Additional file 2: Table A2 of [89]). By the end of the powered condition of session 3, subjects had adapted to reduce their rectus femoris r.m.s. EMG by  $20.2 \pm 9.2\%$  compared to the 1<sup>st</sup> unpowered condition. As subjects learned to walk in the exoskeleton, their rectus femoris activity decreased across sessions during the powered minutes 3-6 ( $P=0.005$ ). The most noticeable change was the reduction in peak EMG activity shown by Figure 4.4. By session 3, subjects were able to reduce their peak rectus femoris activation level around toe off by  $43.8 \pm 13.8\%$  compared to the 1<sup>st</sup> unpowered condition. Unlike the rectus femoris EMG, the vastus lateralis EMG showed no r.m.s. reduction during powered walking. The biceps femoris long head EMG r.m.s. values showed significant reductions during each session (all  $P<0.05$ ), yet the reduction observed during the end of the powered condition lasted through the end of the 2<sup>nd</sup> unpowered condition (Additional file 2: Table A2 of [89]).

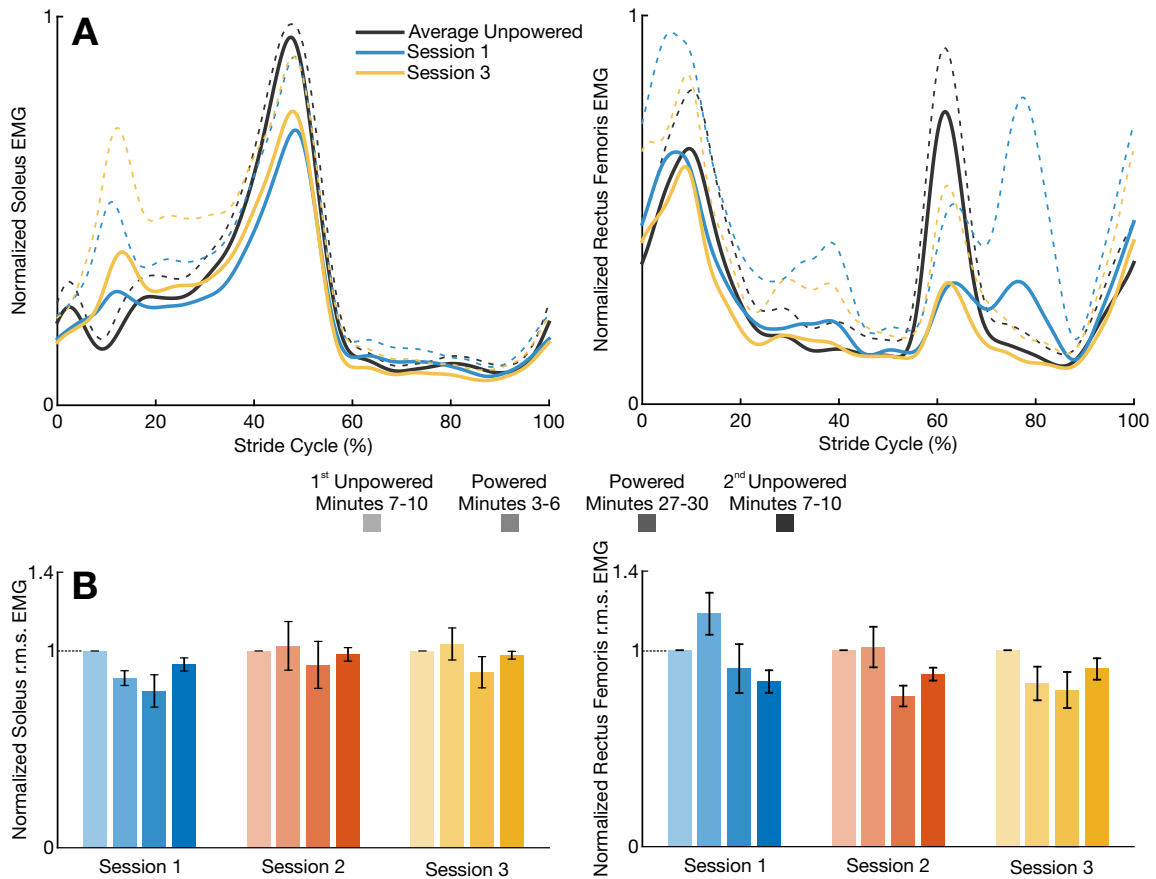


**Figure 4.4: Soelus and rectus femoris results from each training session.** (A) The mean soleus and mean rectus femoris EMG linear envelope (high-pass cutoff frequency of 35 Hz and low-pass cutoff frequency of 10 Hz) of eight subjects is represented by the solid lines and +1 s.d. is represented by the dashed lines. (B) The mean soleus and mean rectus femoris r.m.s. of rectified EMG for four time intervals is indicated by the colored bars across all three sessions. Error bars represent  $\pm 1$  s.e.m. Each subject's r.m.s. values were normalized to the corresponding session's 1<sup>st</sup> unpowered r.m.s. value prior to averaging.

#### 4.3.4 Joint Kinematics

Subjects had the largest change in joint kinematics at the ankle when comparing powered to unpowered conditions (Figure 4.5). A linear regression between ankle kinematics from the end of the powered condition in session 3 and the 1<sup>st</sup> unpowered condition of that same session had an  $R^2$  value of  $0.58 \pm 0.11$ . This lack of correlation between the two conditions is due to the fact that subjects plantar flexed  $\sim 8-9^\circ$  more throughout the mid and late stance phase (30-60% gait cycle). Subjects continued to increase peak plantar flexion from session 1 ( $23.5^\circ$ ) to session 3 ( $27.3^\circ$ ). The powered peak plantar flexion values are large compared to the 1<sup>st</sup> unpowered condition ( $12.9^\circ$ ).

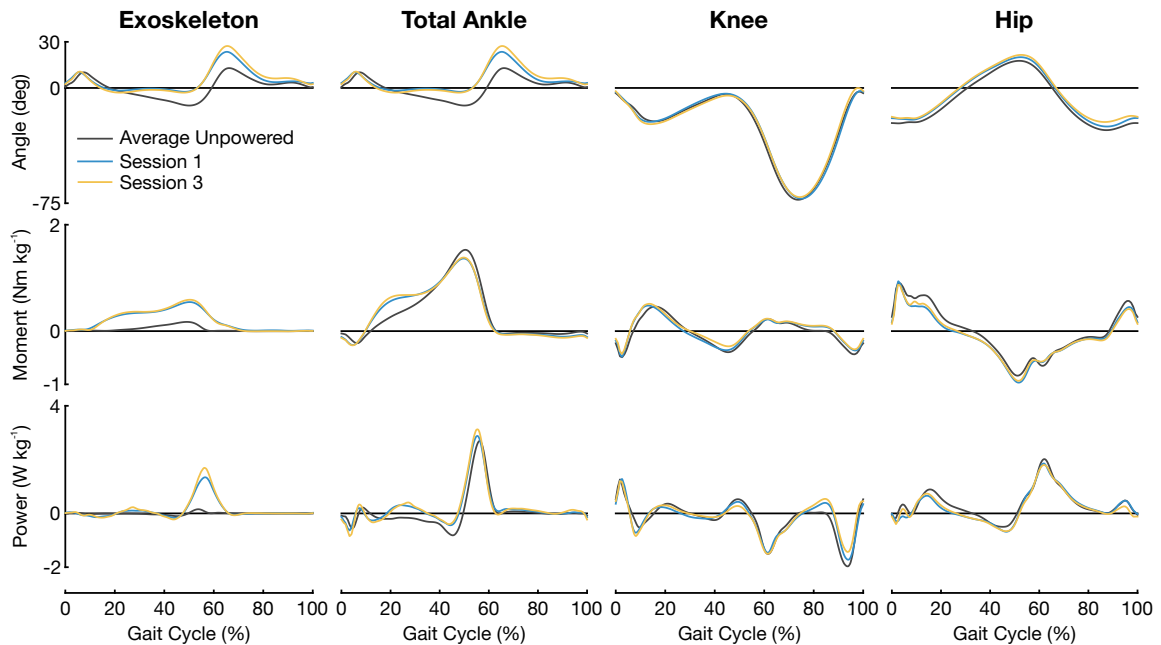


**Figure 4.5: Joint kinematics, dynamics, and power from the beginning and end of training.** Mean joint angles, moments, and powers from eight subjects. Joint dynamics and power have been normalized by subject mass. In the kinematics and dynamics plots all positive numbers represent extension while all negative numbers represent flexion.

Little change was observed in the knee and hip kinematics. All hip and knee linear regressions comparing the end of the powered condition to the 1<sup>st</sup> unpowered condition of each session had  $R^2$  values greater than 0.97.

### 4.3.5 Joint Mechanics

The relationship between subjects' actuation control signal magnitude and exoskeleton torque output was approximately linear with an  $R^2$  value of  $0.74 \pm 0.13$  by the end of session 3. The mean total moment at the ankle (biological and exoskeleton) increased  $\sim 0.16$ - $0.18 \text{ Nm kg}^{-1}$  ( $\sim 47.8\%$ ) during the early to mid stance phase (0-30% gait cycle) when comparing the end powered conditions to the average unpowered condition (Figure 4.5). This increase in total ankle plantarflexion moment during the early to mid stance phase corresponds with a decrease in hip flexion muscle moment. Subjects experienced a decrease in mean hip flexion muscle moment  $\sim 0.14$ - $0.15 \text{ Nm kg}^{-1}$  ( $\sim 31.7\%$ ) during this phase of the gait. There was little change in knee joint dynamics.

Subjects increased positive average total ankle power when the exoskeleton was powered ( $P=0.001$ ; Figure 4.6). Most noticeably, subjects walked with a  $0.13 \pm 0.01 \text{ W kg}^{-1}$

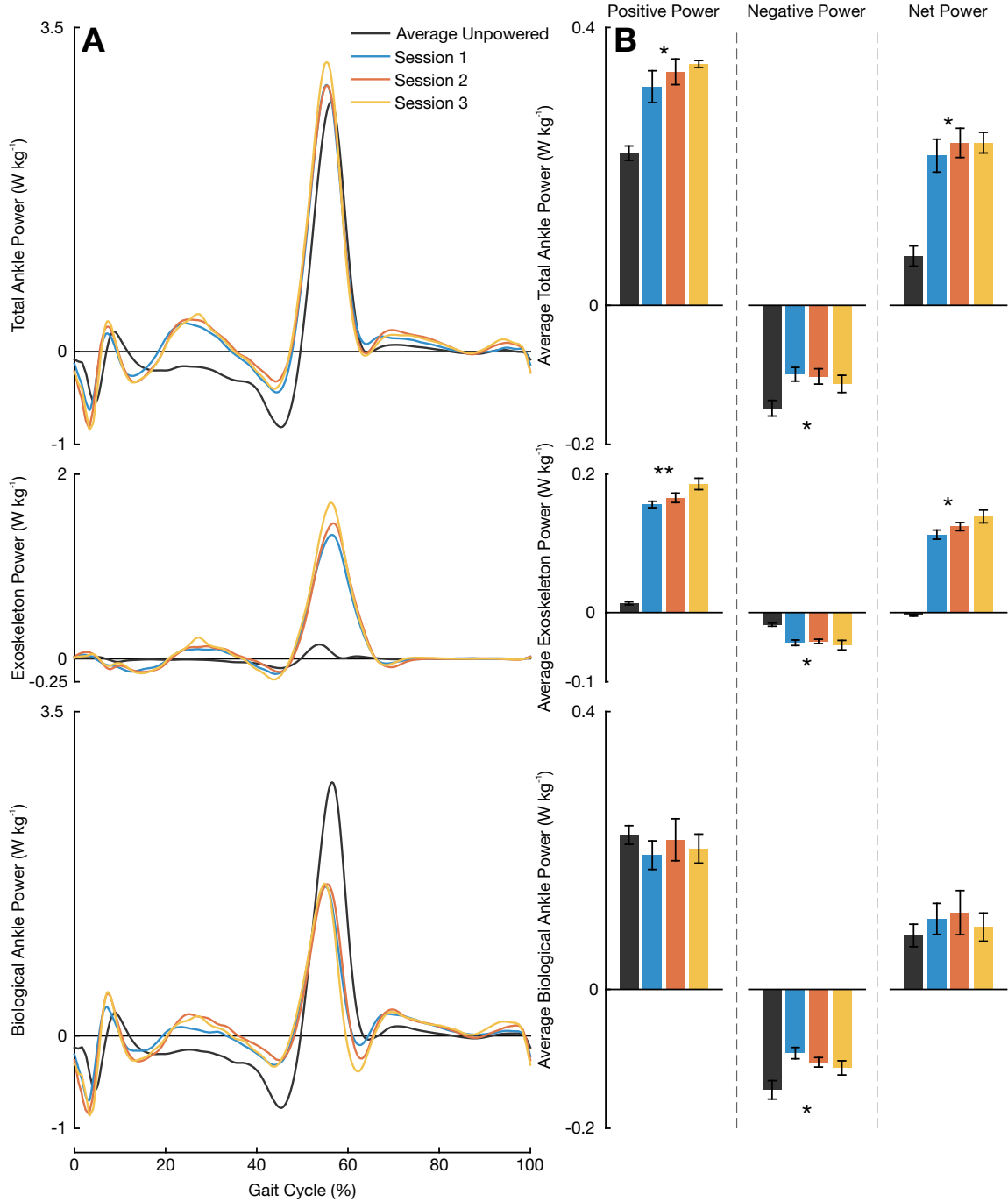


**Figure 4.6: A breakdown of ankle power contributions from each training session.** (A) Mean total ankle power, exoskeleton power, and biological ankle power from eight subjects across all three sessions. The exoskeleton power was calculated from ankle kinematics and force outputs. The biological power was calculated by subtracting the exoskeleton power from the total ankle power. (B) Average power plots of positive, negative, and net power for total ankle power, exoskeleton power, and biological ankle power. All error bars represent  $\pm 1$  s.e.m. An asterisk represents significance across all four conditions (ANOVA,  $P < 0.05$ ) and a double asterisk represents significance in both all four conditions as well as just across sessions 1-3 (ANOVA,  $P < 0.05$ ).

( $65.8 \pm 8.9\%$ ) increase in positive average total ankle power by session 3 relative to the average unpowered condition. Across training sessions, subjects increased their positive ankle exoskeleton power as they adapted to the device ( $P=0.019$ ). Subjects had no significant change in net biological power output between powered and average unpowered conditions ( $P=0.614$ ). There was no significant difference in average net knee power between powered and average unpowered conditions ( $P=0.195$ ), yet a decreasing trend of the magnitude was observed. Between the average unpowered condition and the end of session 3's powered condition, there was a 25.4% reduction in the magnitude of the average net knee power. There were significant differences in average positive hip power between powered and average unpowered conditions ( $P=0.003$ ). By session 3, subjects walked with an average positive hip power  $0.06 \pm 0.01 \text{ W kg}^{-1}$  ( $14.7 \pm 2.5\%$ ) less than that of the 1<sup>st</sup> average unpowered condition (Figure 4.7).

Subjects increased the amount of average total positive power,  $\overline{P}_{Tot}^+$ , from the average unpowered condition to the end of the powered sessions ( $P=0.009$ ). Additionally subjects altered percent contributions of the ankle and hip joint to  $\overline{P}_{Tot}^+$  ( $P=0.002$  and  $P=0.002$  respectively; Figure 4.8). There was no significant change in percent contributions from the knee between conditions ( $P=0.165$ ). Percent contributions from the ankle increased from  $27.7 \pm 1.9\%$  to  $41.2 \pm 1.0\%$  between the average unpowered condition and the end of the powered condition of session 3. Percent contributions from the hip decreased from  $52.8 \pm 1.6\%$  to  $41.3 \pm 0.9\%$  between the average unpowered condition and the end of the powered condition of session 3.

## 4.4 Discussion

The results from this study support our hypothesis that subjects would learn to reduce their energetic cost when walking in the robotic ankle exoskeletons. By the end of the session 3, subjects required  $3.01 \pm 0.08 \text{ W kg}^{-1}$  to walk in the powered device. This result is comparable to that of previous studies using a traditional proportional myoelectric controller [116]. An important difference between our metabolic results and that of previous studies is that all eight of our subjects experienced a metabolic reduction by the end of session 1's powered condition. In previous studies, the mean metabolic reduction by the end of session 1's powered condition was approximately zero. Additionally, in previous work subjects had to complete three full training sessions before additional training had no effect metabolic power reduction. In our current study there was no statistically significant difference in net metabolic power reduction at the end of the powered condition across sessions ( $P = 0.193$ ). Although the mean metabolic values at the end of each session's

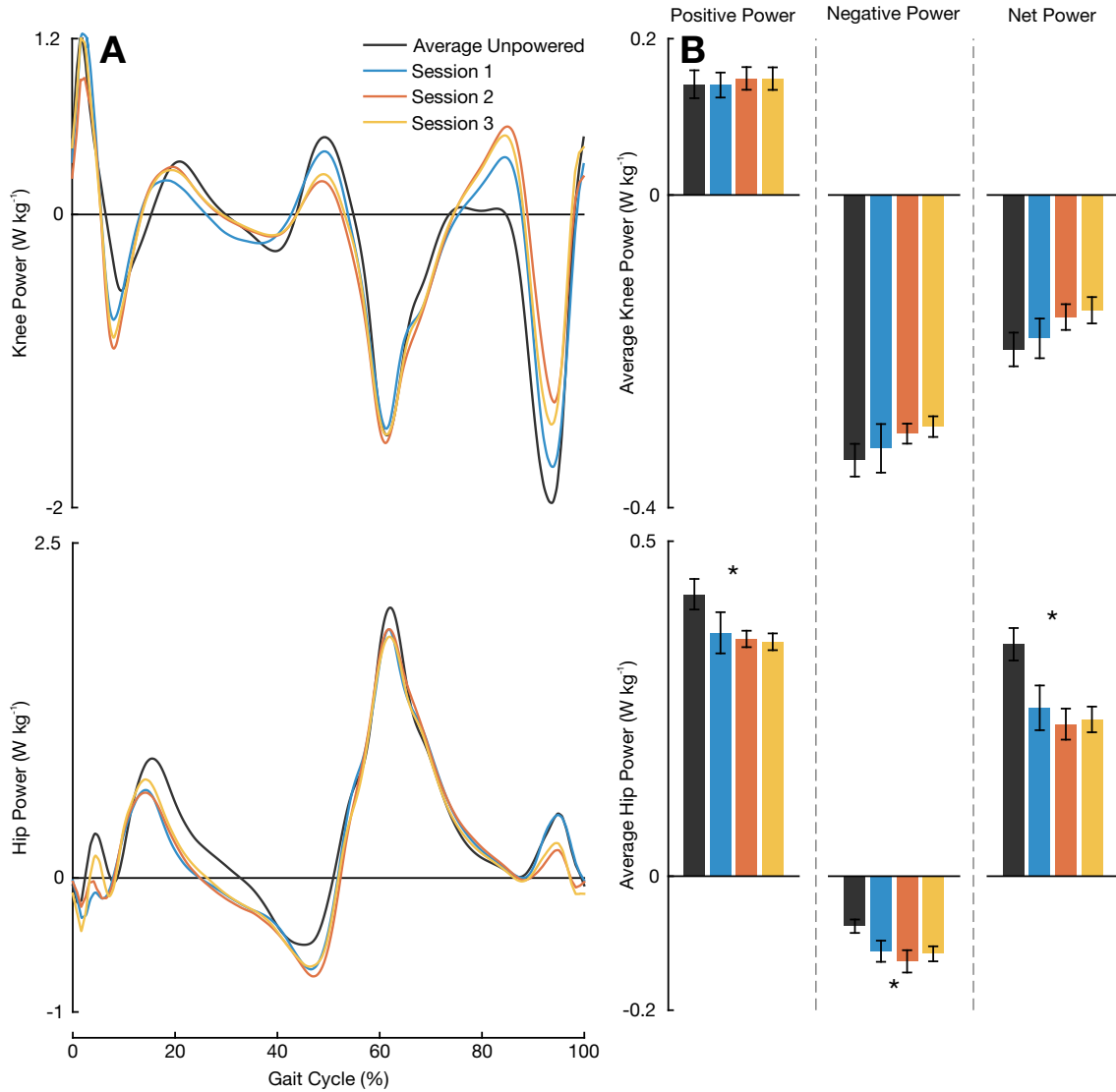


**Figure 4.7: A breakdown of knee and hip power contributions from each training session. (A)** Mean knee power and mean hip power from eight subjects. **(B)** Average power plots of positive, negative, and net power for knee and hip power. An asterix represent significance across all four conditions (ANOVA,  $P < 0.05$ ).

powered condition suggests slight training effects, the percent reduction between the first unpowered condition and end of the powered condition on session 1 was 16.2% were on session 3 it was 17.8%. These results suggests that the learning rate with an adaptive proportional myoelectric controller is faster than that of a traditional proportional myoelectric controller. Despite no significant difference in net metabolic power reduction at the end of the powered condition across sessions, the rate at which subjects reached this net metabolic power reduction increased with additional training sessions. This is made evident by the

significant differences in net metabolic power during the beginning of the powered condition across sessions ( $P=0.028$ ; Figure 4.3 and Table 4.2). These metabolic results show that an adaptive gain proportional myoelectric controller can positively assist users. It is important to note that the control scheme presented here is not the first variation on the traditional proportional myoelectric control algorithm [129]; however, to the best of our knowledge it is the first to implement an adaptive gain.

In addition to the metabolic reductions, our results also suggest that subjects preferred a  $\beta$  value *smaller* than that used in our previous work ( $\beta = 1.50 \pm 0.14$  versus a constant  $\beta = 2$ ). We found that subjects had no statistical difference in final  $\beta$  gains between sessions ( $P=0.273$ ) which suggests the gain converged to a steady state value after only one session. According to Equation Eq. (4.7), this smaller gain should lead to a *larger* total joint activity compared to unassisted walking ( $X_{Tot} > \bar{X}_{Bio}$ ). This relationship might seem unintuitive

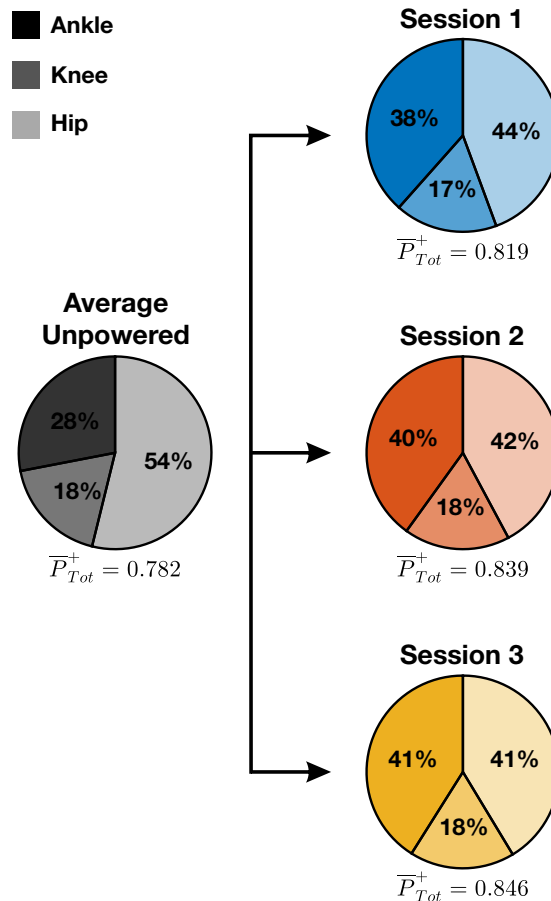


**Figure 4.8: Total positive power contributions from each joint.** Mean ankle (dark), knee (medium), and hip (light) percent contributions to total positive power from eight subjects during unpowered and powered walking.

at first, but it is important to note that in both cases the exoskeleton is operated close to its maximum capacity of  $\widehat{\mathbf{X}}_{Exo}$ . Given a smaller gain  $\beta$ , the user's contribution  $\mathbf{X}_{Bio}$  was larger than that of previous studies without oversaturating  $\mathbf{X}_{Exo}$ . It is this contribution from the user that leads to a larger total joint activity at the ankle. Our prediction of increased  $\mathbf{X}_{Tot}$  as a result of a smaller  $\beta$  manifested itself in this study by an increase in positive average total ankle power. Positive average total ankle power increased from 0.21 to 0.35 W kg<sup>-1</sup> between unpowered and powered conditions on session 3. The exoskeleton provided 0.17 W kg<sup>-1</sup> additional average positive power, while the biological average positive power was reduced by only 0.02 W kg<sup>-1</sup>. We did not observe an increase in total ankle power with our previous work using a static gain proportional myoelectric controller. Our methodology for tuning  $\beta$  in the past may have constrained users to using levels of total ankle power no larger than that of unassisted walking in the device.

This increase in positive average total ankle power led to significant changes in hip joint mechanics. Positive average hip power decreased from 0.41 to 0.35 W kg<sup>-1</sup> between unpowered and powered conditions on session 3. Additionally, our results show that subjects chose to increase ankle contribution to total positive power (27.7 to 41.2%) in exchange for a decrease in hip contribution (52.8 to 41.3%) between these conditions. We acknowledge that the baseline of the unpowered condition is shifted from walking without an exoskeleton most likely due to the added mass of the device. As a point of reference, Farris et al. showed that in healthy subjects walking without any exoskeleton at 1.25 ms<sup>-1</sup> (compared to 1.2 ms<sup>-1</sup> in this study) about 46% of the total average positive power comes from the ankle while 40% comes from the hip [42]. Although the percent contributions of power at the end of session 3 in this study look similar to those reported by Farris et al., we would not conclude that subjects adapted back to normal unassisted gait dynamics. We would not make this conclusion due to the large differences in power and moment profiles of each individual joint from this study compared to that of previously reported profiles of healthy unassisted walking [42, 142]. Our results emphasize that replicating unassisted joint mechanics with assistive devices may not be the best approach to lowering metabolic power. We also observed a trade-off in soleus EMG activity and rectus femoris EMG activity. This result agrees with previous studies such that ankle assistance can lead to decreases in activity at muscles not associated with the ankle [50, 53].

Research has shown that a trade-off between ankle and hip mechanics exists in unassisted locomotion. The possibility of redistributing joint powers has been shown for example by Lewis et al. [95]. When subjects were asked to walk with an increased ankle push off, the power at their hip decreased. However, little has been said about the energetic implications of this trade-off with human subject testing. In 2002, Art Kuo showed in sim-

ulation that increasing work at the ankle can be energetically economical in comparison to doing so at the hip [90]. He further hypothesized that it is only biological limitations that prevent us from using more ankle work in practice. Our results might point in the same direction. During unpowered walking, the ratio of hip to ankle contribution that we observe is larger than that reported in previous literature [42, 117]. This may be a consequence of the increase in required total positive joint power that results from the mass of the exoskeletons which is added distally to the legs. We believe that this additional power is primarily produced at the hip because there exists a biological limitation preventing the ankle from comfortably providing more positive power. With the added power of the exoskeleton, however, subjects were able to increase contributions from the ankle and reduce the effort put forth at the hip. Our findings that an ankle exoskeleton can reduce effort at the hip can potentially be applied to musculoskeletal hip rehabilitation. Given that subjects showed large reductions in average positive hip power, an ankle exoskeleton could be a viable option for those in need of hip assistance yet more testing is necessary to say for certain.

## 4.5 Conclusion

This study used an adaptive proportional myoelectric controller on bilateral ankle exoskeletons to test if users could adapt to the controller to reduce metabolic power and see what  $\beta$  gain they chose when given an adaptive controller. Subjects demonstrated that a significant metabolic reduction can be met after only one day of training. Subjects adapted to a  $\beta$  gain smaller than that used in previous work with traditional proportional myoelectric controllers. This smaller  $\beta$  gain allowed subjects increased amounts of total ankle power compared to unassisted walking and resulted in reduced power output at the hip.

More research is needed to be done in adaptive control of assistive devices to gain a better understanding of how subjects co-adapt with these systems. However, we believe that an adaptive nature of control parameters will be key to developing better assistive devices.

## CHAPTER 5

# Biomechanics and Energetics of Walking in Powered Ankle Exoskeletons Using Myoelectric Control versus Mechanically Intrinsic Control

### 5.1 Background

When it comes to designing the control of lower extremity assistive robotic devices, such as exoskeletons or prostheses, there are a wide variety of control strategies to choose from. Ideally, with the correct control architecture and proper tuning, these devices can work in parallel with the user to aid in their locomotion [77, 101, 106, 111, 152]. There have been many different control strategies explored in research, but there is a lack of knowledge in knowing what type of control to use for certain applications and why.

Lower extremity robotic devices have traditionally been separated into two main approaches for device control. The device assistance can either be driven by *neural signals* or *mechanically intrinsic signals*. Control driven by neural signals relies on the already existing control architecture of the human body. By tapping into physiological electrical signals, such as brain activity or muscle activity, these controllers can decode human intention and actuate the device accordingly [68, 83, 116]. Control driven by mechanically intrinsic signals relies on measures that are intrinsic to the device itself, such as detected gait events, joint angles, or forces [4, 49, 79, 97]. In doing so, these devices are trying to infer human intention from secondary information to drive actuation. For example, a joint angle may be used as a phasing variable for the onset of a predefined actuation signal [112].

Each of these control approaches has its own advantages and disadvantages. For example, control driven by neural signals is often argued to have better human-device synchronization over control driven by mechanically intrinsic signals [147]. Neural signals can

---

The content of this chapter has been submitted and is currently under review for publication in the Journal of NeuroEngineering and Rehabilitation.

be measured before force generation at the muscle has actually occurred due to the electromechanical delay of the body [30]. Therefore, there is a buffer of time between sensing of a neural signal and delivering actuation that is synchronous with the user's movement. In contrast, mechanically intrinsic signals can only be sensed after movement has already occurred. This creates an inherent lag behind the user when using control driven by mechanically intrinsic signals, yet if designed properly this lag may be indistinguishable by the user [36, 151]. Another advantage for control driven by neural signals is that it can allow for direct control by the user. With proportionality in the control scheme, users can directly control the timing and amplitude of actuation at any time instance using the same neurological control they would adjust their own muscle contraction timing and amplitude. This proportionality can lead to a more natural means of control and adaptation compared to a controller driven by mechanically intrinsic signals [25]. One big advantage of using mechanically intrinsic signals to drive control is the reduced complexity over neural signals. Sensors used to measure mechanically intrinsic signals can be self-contained in the device and produce consistent and repeatable measurements. With neural signals, the elec-

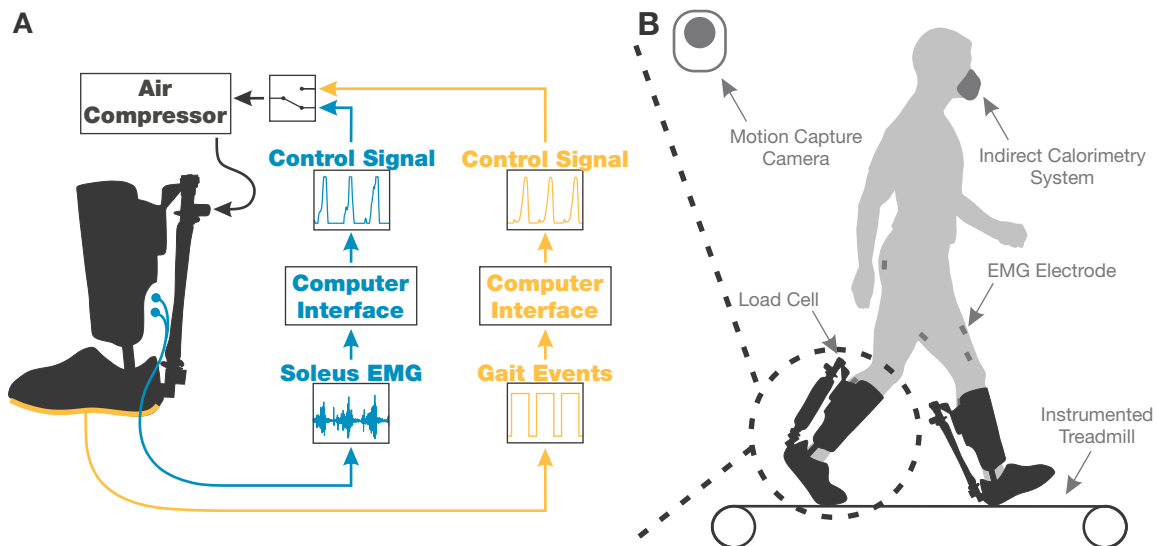


**Figure 5.1: Control algorithms used in testing and the experimental setup.** (A) All eight subjects completed separate 10 minute walking trials with two different control schemes. The dynamic gain proportional myoelectric controller (blue) created a actuation signal proportional to subject's soleus muscle recruitment. The timing-based mechanically intrinsic controller (yellow) sent through the same predefined actuation signal triggered by each heel strike. The two controllers were designed to have the same average actuation signal. (B) Subjects walked at  $1.2 \text{ ms}^{-1}$  with pneumatically powered bilateral ankle exoskeletons. During testing we measured subjects' joint kinematics and dynamics (motion capture and instrumented treadmill), muscle activity (EMG electrodes), exoskeleton kinetics (load cells), and energy consumption (indirect calorimetry).

trodes used for electroencephalography (EEG) or electromyography (EMG) can have large variability depending upon placement and skin conditions. With relatively high noise content, neural signals require extensive decoding or filtering before they can be used in real time.

Despite the prevalence of these two types of controller designs, to date, there does not exist any systematic and fair comparison of how they differently affect the biomechanics and energetics of individual users. In the work presented here, we designed an experiment to make a close comparison between a controller driven by neural signals (a proportional myoelectric controller based on soleus muscle recruitment) and a controller driven by mechanically intrinsic signals (a timing-based mechanically intrinsic controller based on gait events). We tested both controllers with healthy subjects wearing bilateral ankle exoskeletons and aimed to better understand users' biomechanical and energetic responses to each during steady-state treadmill walking (Fig. 5.1). We designed these two controllers to have the *same average* actuation signal such that the main difference between them was the way in which the actuation was driven. To ensure the same average actuation signal, we created the actuation profile for the timing-based controller directly from the average of control signals seen during use with the proportional myoelectric controller. In previous work, we have mathematically derived the inherent relationship between muscle activation and device output when using a proportional myoelectric controller [89]. The timing-based controller we are showing here does not have such dependency so the actuation signal was consistently the same regardless of the user's soleus muscle recruitment. Our primary hypothesis was that the human nervous system would identify this key difference between controllers and therefore use each in a distinct way, thus resulting in a difference in metabolic work rate between the two controllers. We have investigated where some of these differences in use may be by analyzing subject's muscle recruitment, joint kinematics, and joint dynamics.

## 5.2 Methods

### 5.2.1 Subjects

In this study we tested eight healthy subjects with no prior experience walking in powered exoskeletons (male,  $21 \pm 1$  years,  $74.0 \pm 2.7$  kg,  $180.0 \pm 2.8$  cm; mean  $\pm$  standard error of the mean). We pre-screened all participants for exoskeleton hardware fit prior to testing. All subjects gave informed written consent to participate in the study in accordance to the University of Michigan Medical School's Institutional Review Board.

## 5.2.2 Exoskeleton Hardware

The bilateral ankle exoskeletons that we used in this study were similar in design to our previous work [44, 45, 59, 116]; however, we designed these exoskeletons to be more adjustable and versatile to fit a number of subject sizes. These were the same exoskeletons as presented in [89].

The exoskeletons consisted of an adjustable shank component attached to a shoe component by a single degree of freedom rotational joint. The rotational joint constrained the exoskeleton's motion to plantar flexion and dorsiflexion. The shank component was made from stainless steel rods and plastic cuffs. We used ratchet straps on the cuffs to fit the shank to different subject sizes. The shoe component was a standard orthotic shoe that we outfitted with metal attachments for actuation and joint coupling. The exoskeleton could accommodate subjects that wore between a 9 and 11 U.S. men's shoe size.

We actuated the exoskeletons using custom built artificial pneumatic muscles attached posteriorly. These actuation units only provided plantar flexion assistance to the user [44]. We attached a load cell in series (Omega Engineering, Stamford, Connecticut) with the actuator to measure actuation kinetics. The shoe, shank, actuator, and load cell combined to a total mass of 2.08 kg (approximately 0.81 kg at the foot and 1.27 kg at the shank).

## 5.2.3 Exoskeleton Control

In this study we used two different controllers, a dynamic gain proportional myoelectric controller and a timing-based mechanically intrinsic controller, on the same exoskeleton hardware. We built both of these controllers in Simulink (The MathWorks, Inc., Natick, MA) and compiled them to run on a real-time control board (dSPACE, Inc., Northville, MI).

### 5.2.3.1 Dynamic Gain Proportional Myoelectric Control

The proportional myoelectric controller was driven by user's soleus EMG activity. We measured subjects' soleus activity in real time using EMG surface electrodes (sample rate: 1000 Hz; Biometrics, Ladysmith, VA). The designed controller then processed the recorded signal into its linear envelope by high-pass filtering (2nd order Butterworth, cutoff frequency 80 Hz), full-wave rectifying, and then low-pass filtering (2nd order Butterworth, cutoff frequency 4 Hz) the raw signal.

The controller multiplied the calculated linear envelope by a gain to linearly map the small voltage of the processed EMG signal into a larger control voltage that was sent to the pneumatic pressure control valves (MAC Valves, Wixom, MI). We applied a threshold

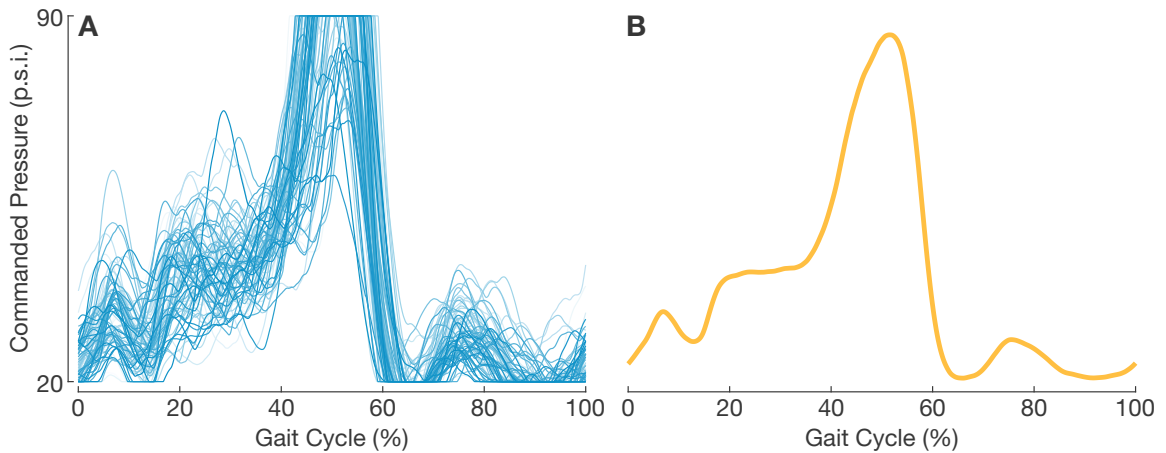


**Figure 5.2: Creating the timing-based control signal for a representative subject.** (A) The actuation signals from 80 of the final 100 strides of a subject’s walking bout with the dynamic gain proportional myoelectric controller were considered in creating the actuation signal for the timing-based controller. Those 80 strides are shown here for a single representative subject and from a single leg. The darker the color of the actuation signal, the later in the walking bout it occurred (B) The actuation signal for the timing-based mechanically intrinsic controller was generated from the average of the 80 strides considered from the walking bout with the myoelectric controller.

to this control signal such that the commanded pneumatic pressure needed to be greater than 20 pounds per square inch (p.s.i) in order to actuate as the pneumatic muscles were pretensioned with this pressure to allow for a faster response time. The maximum output pressure of our pressure source was 90 p.s.i. and control signals were saturated beyond this point. The controller was designed to continuously tune the linear mapping gain on a subject-specific basis using a dynamically adaptive algorithm as described in [89]. This algorithm tuned the gain such that the average peak EMG signal over the previous 50 strides mapped to a desired maximum control signal voltage. We chose a desired maximum control voltage that resulted in the peak of the average control signals to be the maximum output pressure of the valves (90 p.s.i.). This created a controller that, on average, supplied maximal peak actuation to the user at the same moment when they reached their maximal peak soleus activity for that given stride. In this control scheme, the user could adapt their own muscle activity to whatever level they felt comfortable with, while still receiving maximal peak power output from the device.

### 5.2.3.2 Timing-Based Mechanically Intrinsic Control

The timing-based mechanically intrinsic controller was driven by detected heel strikes as sensed by an instrumented treadmill (Bertec Corporation, Columbus, OH). We designed

this controller to have the same average actuation signal as that of the proportional myoelectric controller (Fig. 5.2). To generate the actuation profile for this timing-based controller, we first normalized the actuation signals from the final 100 strides of a subject’s walking bout using the proportional myoelectric controller by their percent gait cycle (heel strike to heel strike). We then averaged these 100 normalized actuation signals. We calculated the root mean squared error (RMSE) for each of the 100 individual stride’s actuation signal compared to this average and then discarded the 20 strides with largest RMSE values to safely remove any outliers. We then averaged the remaining 80 strides’ actuation signals to generate the actuation profile for the timing-based mechanically intrinsic controller. This whole process was performed separately for each individual subject and leg.

During walking, the timing-based controller would assist with plantar flexion upon each detected heel strike. This process was equivalent to pressing a “play” button on the pre-defined actuation signal with each heel strike. If a stride was shorter than the averaged control signal, the signal would start over immediately. If a stride was longer than the averaged control signal, the actuators remained at a pressure that resulted in zero force generation until the next detected heel strike occurred.

#### **5.2.4 Testing Protocol**

We trained all participating subjects in this study to walk with the powered ankle exoskeletons prior to the data collection presented here. All subjects had no experience with walking in a powered assistive device prior to this training. In recruiting a naive subject pool, we have ensured that all subjects were given the same amount of time to adapt and learn to walk in the exoskeletons. The training consisted of three separate days of walking with the exoskeletons using the dynamic gain proportional myoelectric controller. During these training sessions, subjects walked continuously on a treadmill at a fixed speed in the exoskeletons for 50 minutes, the middle 30 of which were powered. A more detailed description of these sessions and subjects’ adaptations is described in [89].

After completing the three training sessions, we tested subjects on a separate fourth day to collect the data presented here. During this final testing session, subjects participated in four walking bouts that were each 10 minutes long. Subjects were given a seated rest period of 5-10 minutes between bouts. First, subjects walked in the exoskeletons without any actuation. We will refer to this bout as the *unpowered* condition. Subjects then walked using the dynamic gain proportional myoelectric controller in order to re-familiarize themselves with the devices and to generate the data necessary to build the control signals for the timing-based mechanically intrinsic controller. This walking bout served purely as a

warm up for subjects and a calibration for the timing-based controller. As such, no results from this bout are presented here. After the warm up session, subjects walked using the timing-based mechanically intrinsic controller and then walked using the dynamic gain proportional myoelectric controller. We will refer to these bouts as the *timing-based* and the *proportional myoelectric* controller conditions, respectively. All walking bouts took place at 1.2 m/s on an instrumented treadmill. We considered the final three minutes of each walking bout for respiratory analysis and the final 25 strides of each walking bout for all gait analyses. We normalized all stride-related data from heel-strike (0% gait cycle) to heel-strike (100% gait cycle) of the same leg.

### 5.2.5 Metabolic Cost

We measured subjects'  $O_2$  and  $CO_2$  flow rates during walking using a portable open-circuit indirect calorimetry system (CareFusion Oxycon Mobile, Hoechberg, Germany). We converted these measurements to metabolic power using formulas from Brockway [19]. We recorded a three minute standing trial from each subject at the beginning of the testing session and averaged it to get subjects' standing metabolic work rate. This calculated standing metabolic work rate was then subtracted from each walking bout to calculate the net metabolic work rate [63]. We analyzed each walking bout by averaging the final three minutes of recorded walking metabolic data, and then normalized these averages by subjects' body mass. During all testing, subjects remained in the aerobic range of exertion as all respiratory exchange ratios were less than one [20].

### 5.2.6 Electromyography

We measured muscle activity from the soleus, tibialis anterior, medial gastrocnemius, biceps femoris long head, vastus lateralis, rectus femoris, and gluteus maximus using electromyography (EMG). All EMG recordings and analysis, except for the soleus, came solely from the subjects' right leg. Soleus activity was recorded and analyzed from both the left and right legs since soleus activity was used as a control input for the proportional myoelectric controller. We recorded all muscle activity using bipolar surface electrodes (sample rate: 1000 Hz; Biometrics, Ladysmith, VA) with an inter-electrode distance of 2.0 cm and electrode diameter of 1.0 cm. The EMG amplifier had a bandwidth of 20-460 Hz. We placed all electrodes on subjects' legs in accordance to the procedures of Winter and Yack [141].

During post processing, we high-pass filtered all raw EMG signals with a 35 Hz cut-off frequency (3rd order Butterworth filter, zero-lag) and then full-wave rectified the filtered

signals. To compute the signals' linear envelopes, we low-pass filtered the rectified signals with a 10 Hz cut-off frequency (3rd order Butterworth filter, zero lag). Each linear envelope was then parsed by stride (heel-strike to heel-strike), normalized to stride cycle, and averaged. We normalized each muscle's linear envelope amplitude by its corresponding average peak voltage from the unpowered walking bout on a subject-specific basis [141]. In addition to the linear envelopes, we calculated the root mean square (r.m.s.) stride average for the rectified EMG signals. We normalized each muscle's r.m.s. stride average by its corresponding average from the unpowered walking bout on a subject-specific basis. All EMG normalization was done prior to averaging.

### 5.2.7 Kinematics

All subjects wore a 39 reflective marker set during testing (34 on the pelvis and lower limbs, 4 on the torso, and 1 on the head). We tracked all marker positions using a 10-camera motion capture system (sample rate: 100 Hz; Vicon, Oxford, UK). We calculated joint kinematics from the raw marker data using OpenSim 3.2 [34]. In OpenSim we scaled a generic 23 degree of freedom, 54 actuator model to subject specific marker placements. During processing, we ensured that all subject model scaling and inverse kinematic root mean square values were within the range recommend by OpenSim documentation [67].

We calculated the Pearson product moment correlations between different joint kinematic measurements across different walking bouts. We assessed similarities in joint kinematics by the coefficient of determination ( $R^2$ ) of these correlations [59].  $R^2$  values approaching 1 indicate strong similarities in joint trajectories as an  $R^2$  value equal to 1 indicates a perfect match in trajectories.  $R^2$  values close to 0 indicate strong differences in trajectories.

We calculated all gait kinematic measures (step length, step width, step period, double support period) using motion capture data from the left and right calcaneus markers. All gait events were sensed using ground reaction force data from the instrumented treadmill. All raw motion data was first low-pass filtered using a 5 Hz cut-off frequency (3rd order Butterworth filter, zero-lag) to remove any motion artifact. Step length and step width were defined as the fore-aft and lateral distances, respectively, between the calcaneus markers at the time of detected heel strike. Step period was defined as the time between heel strikes of opposite feet, and double support period was defined as the time between heel strike of one foot and the toe off of the other.

## 5.2.8 Joint Mechanics

To perform inverse dynamics, we imported all ground reaction force data into OpenSim 3.2 and used it in conjunction with the calculated joint kinematics. Each subject model’s mass was scaled anthropomorphically with the manual addition of the mass at the shank and foot to account for the exoskeletons. We removed as much of the residual forces and moments of the inverse dynamics as possible by iteratively adjusting the model using OpenSim’s residual reduction algorithm (RRA). All of the final residuals after using the RRA were within OpenSim’s recommended ranges. They are presented in Table 5.1 [67].

We took the numerical derivative of the joint positions to calculate the joint angular velocities. We filtered these velocities with a 25 Hz cut-off frequency (3rd order Butterworth, zero-lag) to remove any amplified noise that may have resulted from the numerical differentiation. We then multiplied these calculated joint angular velocities by the joint torques resulting from the inverse dynamics to calculate joint power. Exoskeleton power was calculated in a similar fashion, using the calculated ankle angular velocity and the measured actuation torque from the load cell. We subtracted the exoskeleton power from the total ankle power at each time instance to calculate the biological ankle power. Average net joint power was computed by taking the time integral of the power time series data and dividing it by corresponding stride periods [33, 42]. We computed average positive and negative power values in the same way, but by separating out the time integrals to periods of positive and negative power, respectively.

**Table 5.1:** Average residual values after final run of the RRA in OpenSim

	$F_x$	$F_y$	$F_z$	$M_x$	$M_y$	$M_z$	pErr <sub>x</sub>	pErr <sub>y</sub>	pErr <sub>z</sub>
	(N)	(N)	(N)	(Nm)	(Nm)	(Nm)	(cm)	(cm)	(cm)
Maximum	9.7	9.4	12.5	27.0	43.4	34.7	2.8	1.8	0.6
Root Mean Square	5.3	2.8	7.4	8.6	21.2	9.7	1.9	1.1	0.3

$F_x$ ,  $F_y$ , and  $F_z$  refer to the residual forces at the pelvis, and  $M_x$ ,  $M_y$ , and  $M_z$  refer to the residual moments at the pelvis. pErr<sub>x</sub>, pErr<sub>y</sub>, and pErr<sub>z</sub> refer to the translational position error of the markers.

## 5.2.9 Exoskeleton Mechanics

We measured the distance of the exoskeleton joint center to the actuator attachment point as 10.07 cm. We were able to calculate the moment arm of the actuator at each time instance of collection from this distance measure and the calculated ankle kinematics. We filtered all load cell data with a 25 Hz cut-off frequency (3rd order Butterworth filter, zero-lag) and

then multiplied it by this calculated moment arm to compute the exoskeleton torques. To calculate exoskeleton power, we multiplied these torques by the ankle angular velocity. We calculated average exoskeleton power values in the same way as the average joint power values. We calculated exoskeleton mechanics from the left exoskeleton for half of the subjects and the right exoskeleton for the other half due to hardware capabilities during testing.

### 5.2.10 Statistical Analyses

For all statistical comparisons we performed a paired t-test ( $\alpha = 0.05$ ) between walking conditions with the timing-based controller and the proportional myoelectric controller. All reported values and measurements from here forward are presented as the mean  $\pm$  the standard error of the mean (s.e.m.).

## 5.3 Results

### 5.3.1 Metabolic Work Rate

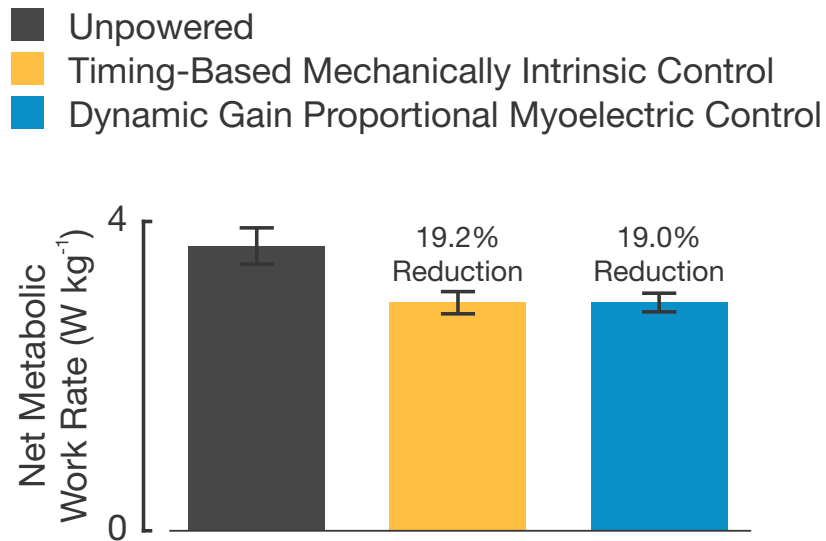


**Figure 5.3: Net metabolic work rate for each tested walking condition.** All net metabolic work rates are normalized to subject mass and represent the absolute changes in energetics for each walking condition. Error bars are  $\pm 1$  s.e.m. from the mean of each condition. The percentages above each powered condition represents the percent decrease in energetics compared to the unpowered condition.

Walking with the exoskeletons powered, regardless of controller used, resulted in large

decreases in metabolic work rate compared with the unpowered condition (Fig. 5.3). Net metabolic work rate of walking in the exoskeletons unpowered was  $3.68 \pm 0.23 \text{ W kg}^{-1}$  (mean $\pm$ s.e.m.). Net metabolic work rate of walking with the timing-based mechanically intrinsic controller was  $2.95 \pm 0.14 \text{ W kg}^{-1}$ , or a  $19.2 \pm 2.5\%$  decrease compared to the unpowered condition. Net metabolic work rate of walking with the dynamic gain proportional myoelectric controller was  $2.95 \pm 0.12 \text{ W kg}^{-1}$ , or a  $19.0 \pm 2.5\%$  decrease compared to the unpowered condition. There was no significant difference in metabolic work rates between the timing-based controller and the proportional myoelectric controller ( $P = 0.966$ ).

### 5.3.2 Electromyography

The largest change in muscle activity was observed at subjects' soleus muscle (Fig. 5.4). When walking with the timing-based controller, subjects achieved a soleus r.m.s EMG reduction of  $28.2 \pm 1.0\%$  and a peak linear envelope reduction of  $37.5 \pm 3.1\%$  compared to the

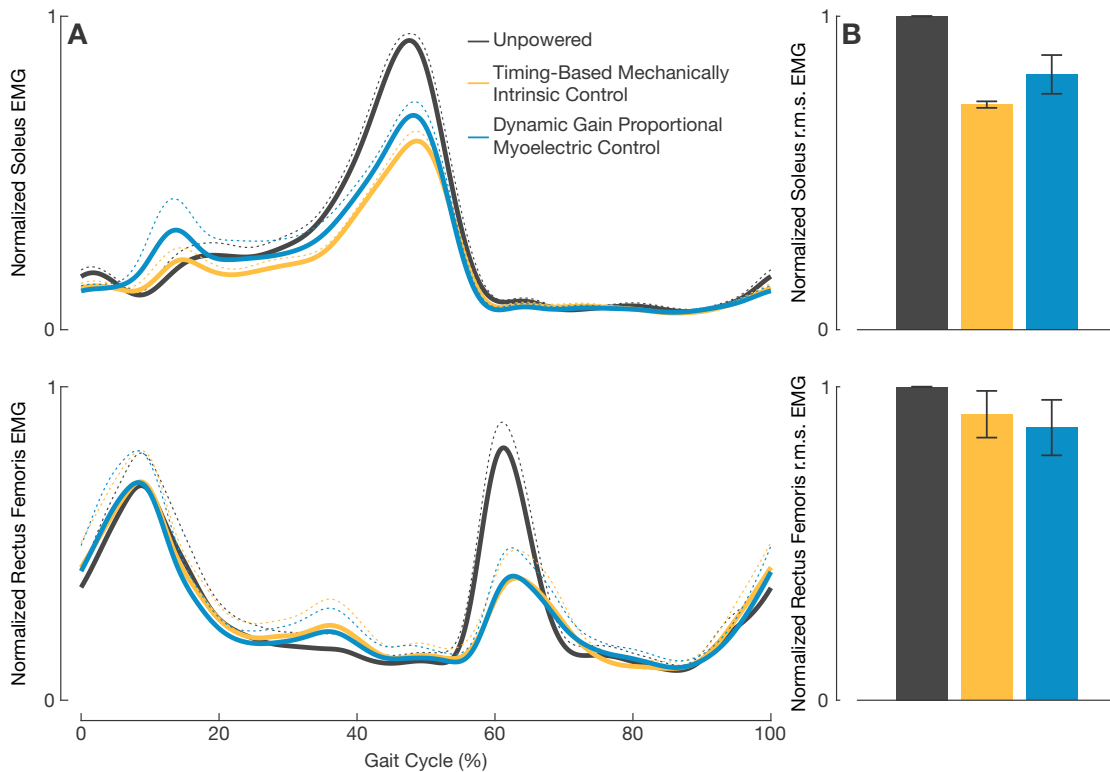


**Figure 5.4: Soleus and rectus femoris EMG results from each walking condition.** (A) The mean soleus and rectus femoris EMG linear envelope from each walking condition is represented by the solid lines and +1 s.e.m. is represented by the dashed lines. (B) The mean soleus and rectus femoris r.m.s. of rectified EMG across the three walking conditions. All error bars represent  $\pm 1$  s.e.m.

unpowered condition. When walking with the proportional myoelectric controllers, subjects achieved a soleus r.m.s. EMG reduction of  $18.6 \pm 6.2\%$  and a peak linear envelope reduction of  $28.8 \pm 4.7\%$  compared to the unpowered condition. Subjects soleus r.m.s. EMG was less when using the timing-based controller than when using the proportional myoelectric controller, yet it was not a statistically significant difference ( $P = 0.132$ ). There was a distinct qualitative difference in the shape of the two powered walking conditions' resulting linear envelopes (Fig. 5.4A). Subjects exhibited a significantly lower peak soleus linear envelope value when using the timing-based controller compared to the proportional myoelectric controller ( $P = 0.026$ ). Also, on average subjects showed  $11.0 \pm 4.9\%$  less muscle activity with the timing-based controller compared to the proportional myoelectric controller during the mid and late stance phases of gait (30-50% gait cycle).

Subjects also experienced large reductions in rectus femoris activity during the powered walking conditions compared to the unpowered condition. When walking with the timing-based controller, subjects achieved a rectus femoris r.m.s EMG reduction of  $8.8 \pm 7.5\%$  and a peak linear envelope reduction of  $35.2 \pm 20.3\%$  compared to the unpowered condition. When walking with the proportional myoelectric controllers, subjects achieved a rectus femoris r.m.s. EMG reduction of  $13.0 \pm 8.9\%$  and a peak linear envelope reduction of  $38.6 \pm 15.0\%$  compared to the unpowered condition. There was little to no difference in the resulting average rectus femoris linear envelopes between the two controllers (Fig. 5.4A). No statistically significant differences were observed between the two powered conditions resulting r.m.s. EMG values at the tibialis anterior, medial gastrocnemius, biceps femoris long head, vastus lateralis, and gluteus maximus (all  $P > 0.05$ ).

**Table 5.2:** Resulting mean gait kinematics of each walking bout

<b>Walking Condition</b>	<b>Step Length (Normalized)</b>	<b>Step Width (Normalized)</b>	<b>Step Period (ms)</b>	<b>Double Support Period (ms)</b>
Unpowered	$0.713 \pm 0.010$	$0.173 \pm 0.011$	$586.3 \pm 5.6$	$161.7 \pm 5.0$
Timing-Based	$0.704 \pm 0.007$	$0.190 \pm 0.016$	$591.6 \pm 6.9$	$167.2 \pm 2.8$
Prop. Myoelectric	$0.692 \pm 0.008$	$0.182 \pm 0.014$	$586.5 \pm 6.6$	$169.0 \pm 2.2$
<i>P</i> -Value	0.004	0.030	0.095	0.256

All values are reported as mean $\pm$ s.e.m. across subjects. All distance measurements have been normalized by leg length.  $P < 0.05$  represents a statistically significant difference between the proportional myoelectric controller and the timing-based controller.

### 5.3.3 Gait Kinematics

There were slight differences between walking conditions' mean gait kinematics (Table 5.2). Subjects exhibited slightly larger mean step lengths and step widths when using the timing-based controller than when using the proportional myoelectric controller ( $P = 0.004$  and  $P = 0.030$ , respectively). There was no statistically significant differences in gait kinematic variability between the two powered conditions (Table 5.3).

**Table 5.3:** Resulting gait kinematic variability of each walking bout

Walking Condition	Step Length (Normalized)	Step Width (Normalized)	Step Period (ms)	Double Support Period (ms)
Unpowered	$0.021 \pm 0.002$	$0.018 \pm 0.002$	$14.1 \pm 1.2$	$7.5 \pm 0.6$
Timing-Based	$0.023 \pm 0.002$	$0.021 \pm 0.002$	$17.6 \pm 1.5$	$9.2 \pm 0.7$
Prop. Myoelectric	$0.026 \pm 0.004$	$0.021 \pm 0.001$	$17.1 \pm 2.2$	$11.2 \pm 1.1$
<i>P</i> -Value	0.231	0.970	0.615	0.210

Variability has been defined as the average standard deviation across subjects. All values are reported as mean $\pm$ s.e.m. across subjects. All distance measurements have been normalized by leg length.  $P < 0.05$  represents a statistically significant difference between the proportional myoelectric controller and the timing-based controller.

### 5.3.4 Joint Kinematics

During powered conditions, subjects experienced the largest deviations from unpowered walking kinematics at the ankle. Subjects increased plantar flexion by an average  $\sim 14^\circ$  during the mid-to-late stance phase of gait when using both the timing-based and the proportional myoelectric controllers compared to the unpowered condition (Fig. 5.5). A linear regression between ankle kinematics of the timing-based controller and of the unpowered condition resulted in an  $R^2$  value of  $0.73 \pm 0.05$ . A linear regression between ankle kinematics of the proportional myoelectric controller and of the unpowered condition resulted in an  $R^2$  value of  $0.71 \pm 0.08$ . A linear regression between ankle kinematics of the timing-based controller and the proportional myoelectric controller resulted in an  $R^2$  value of  $0.98 \pm 0.01$ .

There were little to no changes in joint kinematics at every other joint between conditions. Linear regressions of knee and hip kinematics between powered and unpowered conditions all resulted in  $R^2$  values greater than 0.98. Linear regressions of knee and hip kinematics between the two controllers all resulted in  $R^2$  values greater than 0.99.

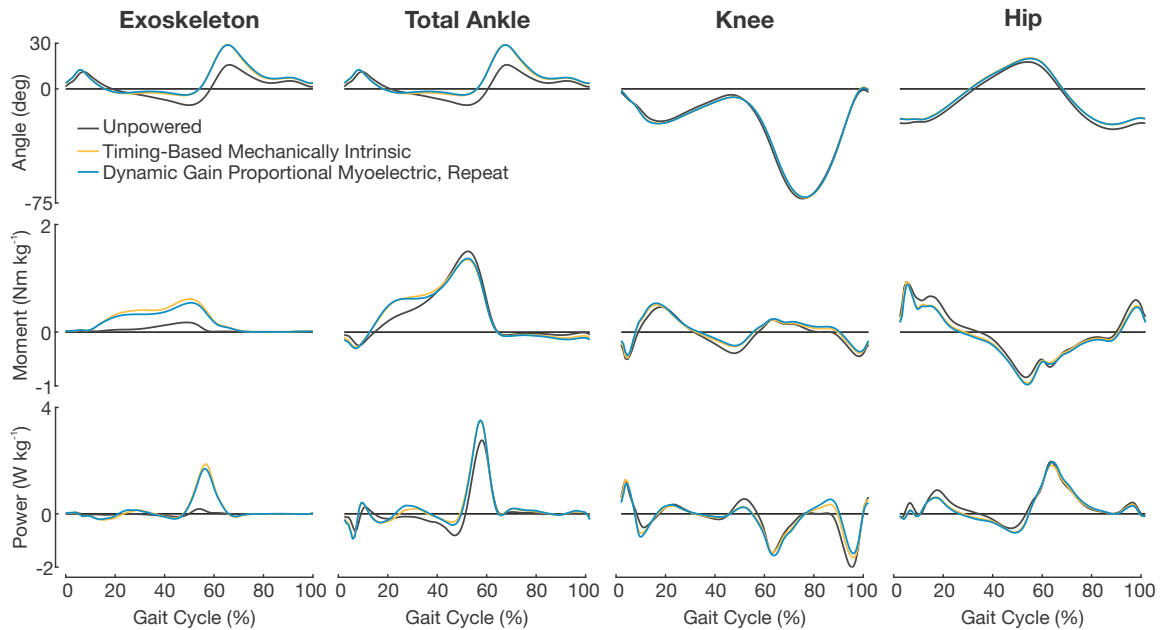


**Figure 5.5: Joint kinematics, dynamics, and power from each walking condition.** The mean joint angles, moments, and powers from the unpowered, timing-based mechanically intrinsic control, and second bout with the dynamic gain proportional myoelectric control conditions. Joint dynamics and power have been normalized by subject mass. In the kinematics and dynamics subplots all positive numbers represent extension while all negative numbers represent flexion.

### 5.3.5 Joint Kinetics

Subjects increased their mean total moment at the ankle (biological and exoskeleton) by  $\sim 0.14 \text{ Nm kg}^{-1}$  during the early-to-mid stance phase (0-30% gait cycle) when comparing either of the powered conditions to the unpowered condition (an increase of  $\sim 48.9\%$ , Fig. 5.5). The observed increase in total ankle plantar flexion moment during the early to mid stance phase corresponds with a decrease in hip flexion moment. Subjects decreased their mean hip flexion moment  $\sim 0.12\text{-}0.15 \text{ Nm kg}^{-1}$  during this phase of the gait cycle when comparing either of the powered conditions to the unpowered conditions (a decrease of  $\sim 25\text{-}31\%$ ). Subjects also decreased their mean knee extension moment  $\sim 0.08\text{-}0.10 \text{ Nm kg}^{-1}$  during the mid and late stance phase (30-50% gait cycle) when comparing the powered conditions to the unpowered condition (a decrease of  $\sim 31\text{-}42\%$ ).

Subjects showed large increases in positive and net average total ankle power when the exoskeletons were powered compared to unpowered (Fig. 5.6). When using the timing-based controller, subjects had an average positive total ankle power  $0.13 \pm 0.01 \text{ W kg}^{-1}$  and an average net total ankle power  $0.15 \pm 0.01 \text{ W kg}^{-1}$  larger than that when walking in the devices unpowered (an increase of  $55.2 \pm 4.0\%$  and  $213.0 \pm 38.5\%$ , respectively).

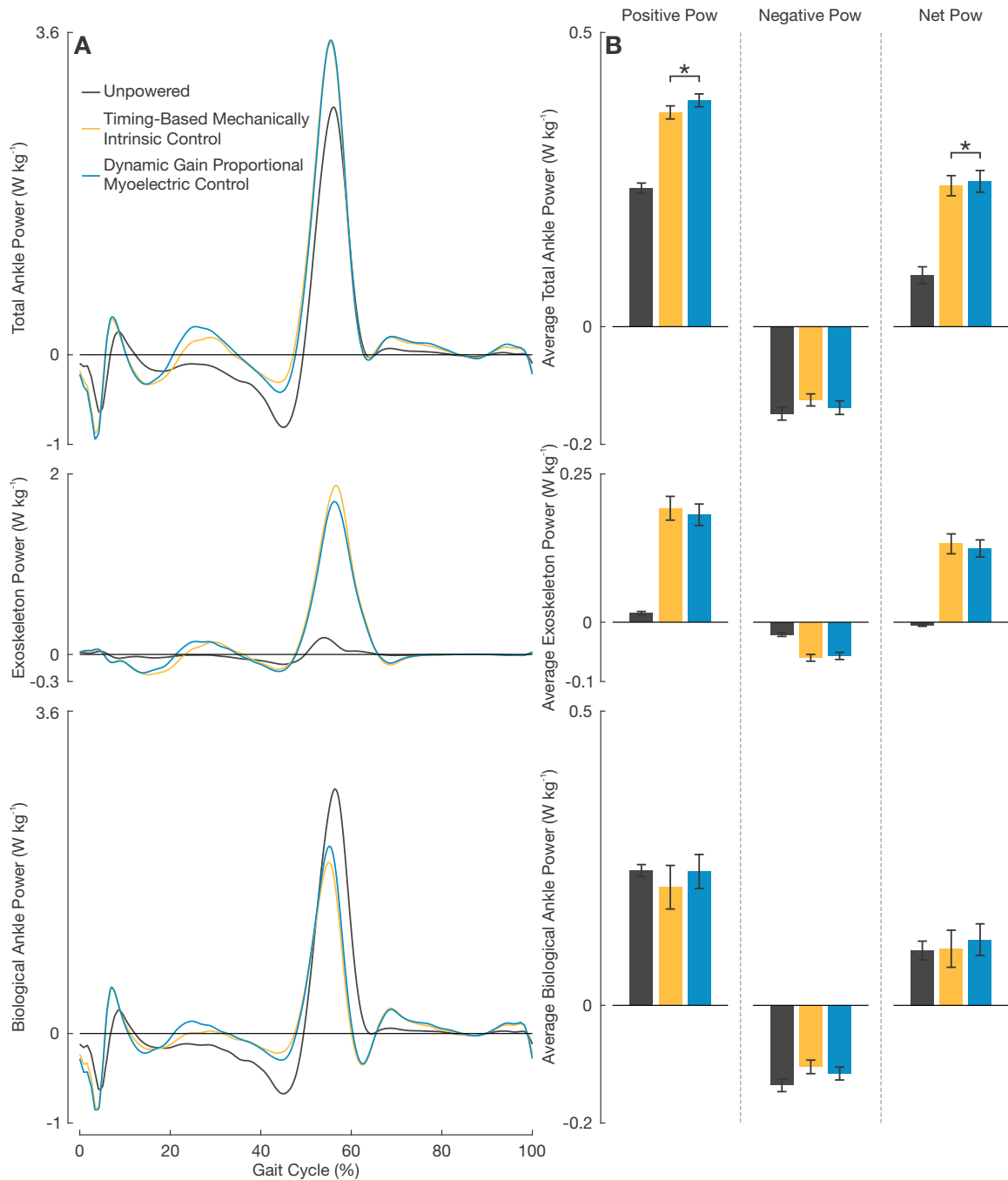


**Figure 5.6: A breakdown of ankle power contributions from each walking condition. (A)** Mean total ankle power, exoskeleton power, and biological ankle power across the three walking conditions. The exoskeleton power was calculated from ankle kinematics and force outputs recorded using the exoskeletons' load cells. The biological power was calculated by subtracting the exoskeleton power from the total ankle power. **(B)** Average power plots of positive, negative, and net power for total ankle power, exoskeleton power, and biological ankle power. All error bars represent  $\pm 1$  s.e.m. An asterisk above the plots represents a significant difference between the two powered walking conditions ( $P < 0.05$ ).

When using the proportional myoelectric controller, subjects had an average positive total ankle power  $0.15 \pm 0.01 \text{ W kg}^{-1}$  and an average net total ankle power  $0.16 \pm 0.01 \text{ W kg}^{-1}$  larger than that when walking in the devices unpowered (an increase of  $64.0 \pm 3.8\%$  and  $222.9 \pm 42.3\%$ , respectively). Subjects showed significantly larger average positive and negative total ankle power when using the proportional myoelectric controller compared to when using the timing-based controller ( $P = 0.005$  and  $P = 0.001$ , respectively). There was no statistically significant difference in average positive, negative, or net exoskeleton power out between the two controllers ( $P = 0.124$ ,  $P = 0.313$ , and  $P = 0.138$ , respectively). There was also no statistically significant difference in average positive, negative or net biological ankle power output between the two controllers ( $P = 0.056$ ,  $P = 0.102$ , and  $P = 0.057$ , respectively); however, the difference in average positive and net biological ankle power were near significant. Subjects on average achieved  $\sim 0.18 \text{ W kg}^{-1}$  greater exoskeleton peak power when using the timing-based controller than when using the proportional myoelectric controller (an increase of  $\sim 11.1\%$ ). There was a statistically significant difference between these peak power values ( $P = 0.048$ ). This increase in peak exoskeleton power corresponded with an average decrease in peak biological ankle power of  $\sim 0.11 \text{ W kg}^{-1}$  when using the timing-based controller compared to the proportional myoelectric controller (a decrease of  $\sim 8.3\%$ ). Due to large variability in subject data, this observations was not of a statistically significant difference ( $P = 0.439$ ).

Subjects put forth significantly greater positive average knee power when using the proportional myoelectric controller than when using the timing-based controller (Fig. 5.7,  $P = 0.003$ ). There were no statistically significant differences in negative or net positive power at the knee between the two controllers ( $P = 0.851$  and  $P = 0.063$ , respectively). Subjects showed large differences in average negative and net power at the hip between powered and unpowered conditions. When using the the timing-based controller, subjects had an average negative hip power  $0.04 \pm < 0.01 \text{ W kg}^{-1}$  and an average net hip power  $0.09 \pm 0.02 \text{ W kg}^{-1}$  larger than that when walking in the devices unpowered (an increase of  $52.3 \pm 5.0\%$  and  $28.1 \pm 4.1\%$ , respectively). When using the proportional myoelectric controller, subjects had an average negative hip power  $0.05 \pm 0.01 \text{ W kg}^{-1}$  and an average net hip power  $0.09 \pm 0.01 \text{ W kg}^{-1}$  larger than that when walking in the devices unpowered (an increase of  $66.4 \pm 9.8\%$  and  $28.0 \pm 2.5\%$ , respectively). There was no statistically significant difference in average positive, negative, or net hip power between controllers ( $P = 0.232$ ,  $P = 0.057$ , and  $P = 0.934$ , respectively).

## 5.4 Discussion

Our primary hypothesis was that metabolic work rate would differ between walking with the timing-based mechanically intrinsic controller and the dynamic gain proportional myoelectric controller. However, we found quite the opposite. Results show that there was no statistically significant difference in metabolic work rate between the two control strategies

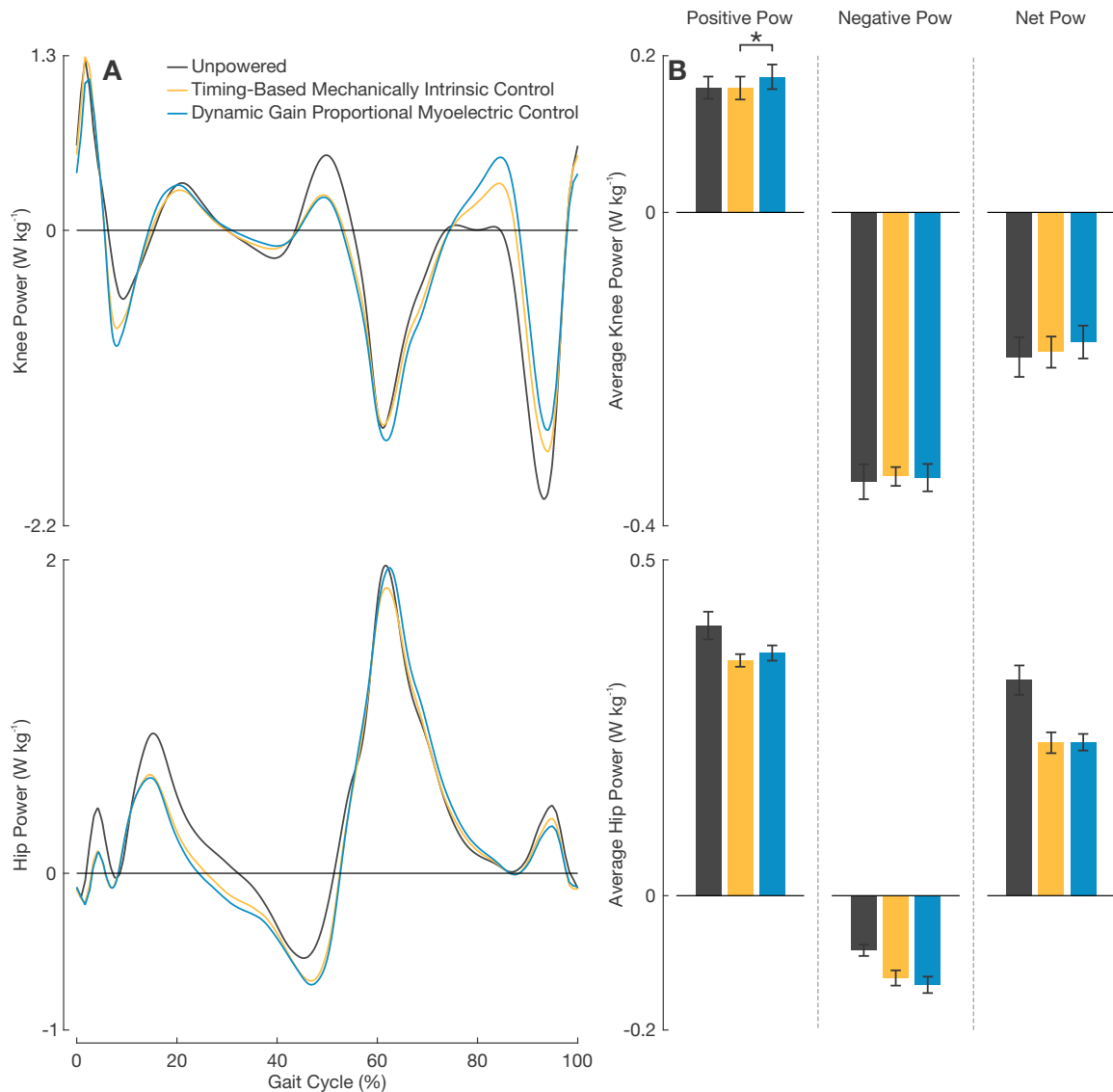


**Figure 5.7: A breakdown of knee and hip power contributions from each walking condition. (A)** Mean knee power and mean hip power across the three walking conditions. **(B)** Average power plots of positive, negative, and net power at the knee and hip. All error bars represent  $\pm 1$  s.e.m. An asterisk above the plots represents a significant difference between the two powered walking conditions ( $P < 0.05$ ).

in this experiment (Fig. 5.3). The reasoning for why we expected a different metabolic work rate between controllers was that we expected subjects to use each controller in a unique way due to the fact that one control strategy was dependent on muscle recruitment and the other was not. Although we did not observe a difference in metabolic work rate, we did observe differences in other biomechanical measures.

Soleus muscle recruitment differed between walking with the proportional myoelectric controller and with the timing-based controller. Although there was not a statistically significant difference in soleus r.m.s. EMG values between the two walking conditions, there was a strong trend in subjects using less soleus muscle recruitment when using the timing-based controller than when using the proportional myoelectric controller. This was made evident by the absolute values of the r.m.s. EMG calculations and the fact that subjects' resulting soleus linear envelopes when using the timing-based controller were 11% less than that of the proportional myoelectric controller during the mid and late stance phases of gait (Fig. 5.4A). Additionally, the peak value of subjects' soleus linear envelopes when using the timing-based controller was significantly less than that when using the proportional myoelectric controller. Similar trends were observed in medial gastrocnemius r.m.s. EMG calculations as well. We believe the reason we did not observe differences in metabolic work rate in this study despite this difference in muscle recruitment was that these devices targeted a relatively small muscle group. If repeated with an exoskeleton that targeted larger muscle groups, such as with a hip exoskeleton [5, 96, 120], it might be expected to see differences in metabolic work rate; however, further research is needed to make this conclusion.

The observed differences in recruitment of plantar flexor muscles had a direct effect on resulting ankle mechanics. We observed that subjects walked with significantly larger average positive and negative total ankle power when using the proportional myoelectric controller than when using the timing-based controller (Fig. 5.6). This increase in power magnitude at the ankle is due to the very slight differences in total ankle moment of the two controller conditions (Fig. 5.5). In looking at the breakdown of total ankle power contributions we see that subjects trended toward significantly larger peak exoskeleton power output when using the timing-based controller than the proportional myoelectric controller (an increase of 11.1%). This corresponded with a trend in decreased peak biological ankle power output (a decrease of 8.3%). Additionally, subjects used less average positive and net biological ankle power when walking with the timing-based controller than with the proportional myoelectric controller. These differences in average positive and net biological ankle power were near statistical significance ( $P = 0.056$  and  $P = 0.057$ , respectively). These ankle power results suggest that when using the timing-based controller subjects

were contributing less to locomotion at the biological ankle and are more so ‘along for the ride’ [143]. This makes sense given that active engagement and involvement at the ankle is not necessarily required when using the timing-based controller. So long as heel strike occurs, subjects will receive actuation. When using the proportional myoelectric controller, active involvement on a muscular level is necessary to directly control the actuation of the device. Additionally, these changes in ankle dynamics seemed to have had an effect on subjects average positive knee power as subjects walked with significantly more positive knee power when using with the proportional myoelectric controller than when using with the timing-based controller.

We attribute these differences in muscle recruitment, and thus the resulting observed differences in ankle power, to the theory of slacking. The idea behind slacking is that the human motor system is always trying to minimize its levels of muscle activation during repetitive tasks where movement error is small, such as walking [113, 143]. One hypothesis for interpreting the differences in soleus muscle recruitment between the two controllers is that when using the proportional myoelectric controller, users can only slack so far before signal quality affects walking stability. This is an inherent technical limitation of using measures of muscle activity to drive a controller. As mentioned prior, neural signals, such as muscle activity, often have large noise content. Therefore as subjects decrease their muscle activity, the signal-to-noise ratio of the measurement decreases making it difficult to separate the signal from the noise. In this specific experiment, the dynamically adjusting gain of the proportional myoelectric controller increases to compensate for decreases in muscle activity. This larger gain will amplify any noise that makes it through the filtering process along with the intended control signal. This amplified noise could then make control of the device difficult and potentially cause for instability with walking. Given this argument, we believe there is a maximum level of slacking that can be obtained with the proportional myoelectric controller presented here. When using the timing-based controller, the actuation is consistently the same for each step regardless of muscle activity. Because of this, users can potentially slack their muscle activity further than with the proportional myoelectric controller without any change to actuation.

Another hypothesis for interpreting the differences in soleus muscle recruitment between the two controllers is that when using the proportional myoelectric controller, users can only slack so far due to the means in which the controller is triggered. No matter what, subjects must use some amount of muscle recruitment to actuate the proportional myoelectric controller. Due to the fact that this controller inherently guarantees synchronous actuation with the user, the user is always moving with the device during actuation. When using the timing-based controller, subjects do not necessarily need to move with the device.

They could potentially lean into the actuation and let it propel them forward in a way that is not possible with the proportional myoelectric controller. This could potentially explain the observed increases in peak exoskeleton power and decreases in biological ankle power. Once figuring out this strategy, subjects can exploit it and become disengaged at a muscle level during walking. Thus, subjects are able to slack further when using the timing-based controller.

Equally interesting to the resulting differences in these two control strategies are how in which the two were similar. The results from this study show that regardless of the control strategy being used, the actuation from the exoskeletons resulted in large reductions the user's metabolic work rate compared to walking unpowered in the devices. The absolute value of these reductions is comparable to previous work in the field [77, 89, 101, 111]. Although it is not a novel finding to show that actuation of an exoskeleton can reduce the metabolic work rate compared to unpowered walking, it is a good proof that both control strategies were able to work in parallel with user to offload some of the energetic requirements of walking. Additionally, gait kinematics between the two controllers were relatively unchanged (Tables 5.2 and 5.3). We found that all lower extremity joint kinematics were largely unchanged from one controller to the other, as evident that all regressions between the two controllers resulted in  $R^2$  values greater than 0.98 (Fig. 5.5). We also observed that regardless of the controller being used, subjects adapted to large increases in total ankle power compared to the unpowered walking condition. This large increase in total ankle power corresponded with large reductions in power at the hip. These reductions in hip power were congruent with reductions in EMG activity at the rectus femoris (Fig. 5.4B). This trade off in joint power and muscle activity between the ankle and hip is consistent with previous work by our research group and that observed by others with different devices and controllers [89, 105, 111]. We find all of these resulting similarities an interesting finding as they shows that if designed properly, these two different types of control approaches can result in very similar biomechanical and energetic adaptations. With the correct design, a researcher could potentially use either type of control scheme with an ankle exoskeleton and achieve largely the same results for steady-state walking; the major differences being in the resulting ankle muscle recruitment and ankle mechanics.

It is difficult to pinpoint the reasons behind the biomechanical differences observed between the two controllers, but the fact that they exist lend insight to when one controller may be better suited than another. For example, if a device is targeted toward therapeutic rehabilitation of neurological injuries [8], a controller driven by neural signals may be more beneficial than one driven by mechanically intrinsic signals due to users being more engaged at a muscle level when using a controller driven by neural signals. This suggestion

is drawn from the success of gait training with human therapists being more successful than that with robotic devices in patients with chronic stroke [70]. This difference is attributed to patients' active involvement when working with a therapist over a robotic device. As this study has only considered testing with healthy subjects, further research would need to be conducted with a clinical population to draw definitive conclusions on this. Additionally, the results from this study suggest that if a metabolic reduction is of interest, it appears that either type of control strategy could be employed.

We acknowledge that this study is a comparison of a single controller driven by neural signals and a single controller driven by mechanically intrinsic signals. There are an infinite number of possible controllers for each that could be compared; however, we believe this is a strong starting point for future work in better understanding controller design for specific applications. Seeing as each control strategy lends itself to different pros and cons, a hybrid of the two approaches may be advantageous, an area of research many have already begun exploring [6,94,129,148]. We also acknowledge that this experiment was performed with a hardware platform that is constrained to a lab setting and is limited in torque output. Further research would need to be performed to show how these principals hold on different devices and walking scenarios.

## 5.5 Conclusion

This study aimed to compare the differences between walking in bilateral ankle exoskeletons using a dynamic gain proportional myoelectric controller and using a timing-based mechanically intrinsic controller. We hypothesized that these two controllers would result in different measures of metabolic work rate due to expected differences in biomechanical measures. We observed no differences in metabolic work rate, small changes in joint kinetics at the knee and hip, and virtually no difference on all leg joint kinematics between the two controllers. The major differences between these two controllers that we did observe were at the ankle. Subjects showed increased soleus muscle activity when using the proportional myoelectric controller than when using the timing-based controller. This corresponded with significantly larger positive and net total ankle power when using the proportional myoelectric controller than when using the timing-based controller. These findings suggest that a controller driven by neural signals may be better suited for therapeutic rehabilitation applications while either controller is well suited for human augmentation purposes.

## CHAPTER 6

# Discussion and Conclusion

Through my dissertation work I have developed and explored the feasibility of adaptive controllers for assistive robotic devices. Additionally, I have investigated the energetic and biomechanical effects of such control schemes on the user, lending insight into how users may adapt and use such devices. What is novel about these controllers is that they autonomously adapt based upon a physiological measure taken from the user. To accomplish this work, I first developed mathematical models and methods to analyze non-steady-state physiological measures (Chapter 2). I then employed these mathematical techniques to conduct the real-time optimization of an assistive robotic device through minimizing measures of users' metabolic work rate (Chapter 3). Making a tangential step along the same lines of adaptive control, I then showed how muscle recruitment could also be used as a physiological measure to base adaptive control on (Chapter 4). Lastly, I conducted a systematic comparison of the energetic and biomechanical outcomes between a controller driven by neural signals versus a controller driven by mechanically intrinsic signals to investigate when one type of control may be more advantageous to use than another (Chapter 5). In this final chapter, I will discuss the implications of this work and how it can be built upon in the future.

### 6.1 Discussion of Contributions

The field of assistive robotic devices faces the difficult question of how to best supply assistance to a device's user. A solution I have posed to this question is to allow the device to adapt to the individual user. This technique allows for customized subject-specific control and lets an algorithm objectively answer the question of how to best supply assistance to the user. The work I have described in the previous four chapters has targeted specific areas of development that can allow for adaptive controllers to become clinically relevant for assistive devices.

The work I presented in Chapter 2 described a technique for estimating and analyzing non-steady-state physiological measures. I took great care in developing this analysis such that it can be applied generally to any physiological measure so long as the measure can be described as a discrete linear system. In doing so, this work has laid the ground work for future developments in using other physiological measures to drive adaptive controllers. However, one of the major impacts of this work is its implications outside of the realm of assistive robotic devices. The parameters considered when mapping a cost landscape do not necessarily need to be parameters on an assistive robotic device. These parameters can easily be any number of different movement parameters, such as walking speed, walking inclines, or step frequency [63, 104, 133]. Therefore, these same techniques could be used during general biomechanics experiments. Furthermore, the demonstrated experimental application of the instantaneous cost mapping analysis in Chapter 2 showed that the developed techniques allow for the rapid exploration of a parameter space when analyzing metabolic work rate. This has huge implications for clinical research as many patients with disability cannot physically walk for the long durations of time required by the current methods of steady-state analysis of metabolic work rate. By using the methods described in this dissertation, experimental biomechanics work can be conducted with clinical populations without requiring them to walk for extended lengths of time. This opens the door to a whole realm of biomechanics research that was not feasible prior to these methods being developed.

The work I have described in Chapter 3 was the first ever example of optimizing the control of an individual device based upon a user's metabolic work rate. The techniques developed in this chapter were also described as mathematically general as possible as to be applicable to any dimensionality of space being optimized. This optimization approach could drastically improve upon the current heuristic and subjective tuning of clinical devices that is common practice in the prescription of a device as described in Chapter 1. As such, a device could co-adapt with a user over long periods of time to identify optimal parameter configurations all while the user learns to best use the device. Since publication, a number of other research groups have built upon this technique using different control paradigms and optimization algorithms [85, 152].

In Chapter 4, I presented an adaptive proportional myoelectric controller that adapted to users' levels of muscle recruitment. This research was unique in that it allowed for control driven by neural signals while always maximizing the devices power output regardless of the levels of muscle recruitment the user adapted to. In doing so, this control scheme allowed users to adapt to the amount of total ankle activity their body desired by regulating their own biological contribution all while the controller maintained synchronization

between the device and the user. The results from this study showed that when given the freedom to drive adaptation with their own muscle recruitment, subjects adapted toward increases in total ankle power in order to decrease their levels of hip power and thus achieve a reduction in their metabolic work rate compared to unpowered walking. This was the first ever study with an assistive device to show this biomechanical interplay between the ankle and hip. Since publication of this work, other studies have confirmed that this interplay is evident despite different device hardware or control [105, 111]. This discovery can have large implications in a clinical environment during device prescription. For example, if someone has a disability that negatively affects the amount of hip power they can output during gait, they may benefit from using an ankle exoskeleton. Additionally, the contributions of this work illustrate how healthy subjects adapt to added assistance at the ankle and will aid in informing future device design.

Lastly, in Chapter 5 I investigated what some of the biomechanical and energetic differences may be in using different controllers. Specifically, how would users use a device differently if the controller were driven by neural signals versus driven by mechanically intrinsic signals so long as each controller had the same average actuation signal. Findings from this work show that energetically, the two controllers are equivalent for an ankle exoskeleton meaning that if human augmentation is the application, either control strategy could potentially be used. However, these same findings showed that subjects recruited less muscle activity when using the controller driven by mechanically intrinsic measures. This discovery suggests that a controller driven by neural signals may be better suited for applications in therapeutic rehabilitation as active involvement during motion has been shown to have more positive outcomes than passive involvement [70]. The contributions of this work may better inform device design for clinical applications focused on therapeutic rehabilitation.

As a collection of work, the chapters of this dissertation have targeted the current state of device tuning and evaluation and proposed a number of improvements that can have a major impact on the field as a whole. Adaptive controllers for assistive devices is a relatively new area of interest and research, but there is already quite a bit of momentum surrounding it. The idea of Body-in-the-Loop optimization and adaptive tuning has already been picked up by a number of other research groups in the field that are trying out different algorithms on a wide variety of hardware [85, 152]. However, to the best of my knowledge, the studies presented here are the first examples of Body-in-the-Loop optimization and adaptive tuning of a device based upon physiological measures. This ground work will be a vital contribution to the field as it is the first known example of this concept being put to use on a device, thus proving its feasibility.

## 6.2 Limitations and Need for Future Research

Chapters 2 and 3 have focused on using metabolic work rate as the physiological objective function to drive a Body-in-the-Loop optimization. Admittedly, metabolic work rate may not be the only cost function to consider in such an optimization; however, it is a good starting point for these types of adaptive controllers due to its ease of collection and ubiquity in the field. During walking, there may be a large number of objective functions that the human body cares about and these would need to be considered in such an optimization. In order to propel this research forward, future research will need to consider additional objective functions such as comfort, perceived effort, or stability; however, these metrics are often difficult to quantify. Research aimed at targeting such objective functions through alternative sensing means will be greatly beneficial to this area of work.

One limitation of focusing on driving an adaptive controller with measures of metabolic work rate is that current methods for estimating metabolic work rate require using a mask that covers the mouth to sample oxygen consumption and carbon dioxide production. It is not feasible to be wearing such a mask on a daily basis when using a device. This downfall makes adaptation based upon alternative physiological measures, such as muscle activity as described in Chapter 4, much more appealing. Future research that focuses on alternative and more discreet sensing of metabolic work rate will allow for adaptive controllers to be more easily and readily implemented. Such work has already taken interest in the field and their success could also allow for sensor fusion to consider multiple different objective functions during an online optimization [12, 76]. In order to make Body-in-the-Loop optimization obtainable to use in the real world, new sensing techniques will need to be developed to allow for discrete and transparent sensing during daily use of the device. The future real-world implementations of this research could be as simple as users putting on a wearable sensing device, much like a Fitbit [128] or smart textile [135], to allow a device to seamlessly adapt to the user throughout the day during use.

In addition to future work in sensing, work in algorithm development will also be crucial to moving the implementation of adaptive controllers forward. The Body-in-the-Loop optimization presented in Chapter 3 relied on a gradient descent algorithm. This simple algorithm worked well in initial testing, but gradient descent methods have their drawbacks. Mainly, a gradient descent algorithm can get trapped in local minima. However, since a gradient descent is only doing a local approximation of the cost landscape, it can easily adapt to changing landscapes as is the case when a user is learning and adapting to a device. A gradient descent algorithm served as a good choice for proof of concept testing, but this body of work could greatly benefit from further focus on more sophisticated al-

gorithms. Future research will need to call upon non-convex optimization techniques or machine learning to push this work forward.

### 6.3 Concluding Remarks

In my view, the two capstones of my dissertation work were the implementations of two very different adaptive controllers as presented in Chapters 3 and 4. I took two very different approaches in designing these controllers and discussing their outcomes lends itself to some very interesting observations. First, in the Body-in-the-Loop optimization work, I designed a controller and algorithm that was explicitly told to adapt such that it minimized users' energetic consumption. In this framework, I as the designer have predefined a target outcome of the human-machine system. Inherently, I have encoded and decided that the exoskeleton and wearer will work together in a way that minimizes the measured metabolic work rate. In contrast to that, with the adaptive gain proportional myoelectric controller I have designed a controller that was only told to maintain maximal power output regardless of the users muscle recruitment. This controller design can be thought of as an adaptive controller that is adapting in order to maintain a constant output. In this framework, I as the designer have only predefined a target outcome for the machine of the human-machine system. In doing so, I have allowed the human nervous system to adapt and use the device in whatever way it preferred. With this difference in predefined outcomes of the two controllers in mind, we can make some interesting observations.

In the case of the adaptive myoelectric controller, the human system is treated as somewhat of a black box. Because in this study the human system is truly driving the adaptation of the device, albeit unconsciously, how the device is being used is completely unknown to the controller. Unlike the Body-in-the-Loop optimization, the adaptive myoelectric controller has no notion of a cost landscape or a target physiological measure to minimize. However, the human nervous system seems to. When adapting and using this type of controller, the human nervous system is theoretically conducting its own optimization based upon some cost landscape that is unknown to us. It is difficult to determine what the objective function is that the human nervous system is trying to minimize as it adapts to the added assistance of the device; nonetheless, it would appear that energetic cost is a large part of it. Subjects adapted their gait over multiple training sessions to lower their metabolic work rate. Most interestingly, subjects adapted to using unconventional joint mechanics in doing so as they increased their levels of total ankle power and reduced their levels of hip power compared to unpowered walking. This was an outcome that was only made possible due to the added power the device.

I am by no means advocating for one type of adaptive controller over another, but I think it is important to identify the differences in each. The Body-in-the-Loop approach is dependent upon some definition of a target outcome by the designer. In my work I have focused on metabolic work rate, but you could imagine how the objective function of this optimization could easily be altered to something different such as muscle activity, joint mechanics, or gait symmetry. What is interesting about this a priori definition of outcome is that the designer needs to have some expectation for what the human system will do. Where this becomes difficult is it is not always obvious how the human body will adapt to a given device. Take for example the unexpected biomechanical outcomes of the testing with the adaptive myoelectric controller. Given these results, I believe it is unclear if we as designers should be the ones guessing about how the human system will or should use a given device until we have a better understanding of what the human nervous system is adapting for. As our understandings of how the human system adapts to added assistance becomes more clear, we can begin to make larger strides in the adaptive control of assistive robotic devices.

The work I have focused on during my dissertation is among the pioneering research in the realm of adaptive control for assistive robotic devices. As such, this work has set the path for an infinite number of subsequent research questions that incorporates control, human-machine interactions, physiological modeling, and human biomechanics. This work has paved the way for many years of interesting and clinically relevant research questions to come. Most importantly, this work has proven that adaptive controllers driven by physiological measures is even feasible. There is no doubt in my mind that adaptive controllers will be the standard for future assistive robotic devices and this is a vital area in which our field will begin to focus its efforts.

## BIBLIOGRAPHY

- [1] T2 product brochure. Accessed Feb. 2015: <http://www.biom.com/assets/2002129-Rev-D-BiOM-T2-Product-Brochure-Web.pdf>.
- [2] H. Akaike. A new look at the statistical model identification. *Automatic Control, IEEE Transactions on*, 19(6):716–723, 1974.
- [3] R. M. Alexander. *Optima for Animals*. Princeton University Press, Princeton, 1996.
- [4] A. T. Asbeck, S. M. De Rossi, K. G. Holt, and C. J. Walsh. A biologically inspired soft exosuit for walking assistance. *The International Journal of Robotics Research*, 34(6):744–762, 2015.
- [5] A. T. Asbeck, K. Schmidt, and C. J. Walsh. Soft exosuit for hip assistance. *Robotics and Autonomous Systems*, 73:102–110, 2015.
- [6] S. Au, M. Berniker, and H. Herr. Powered ankle-foot prosthesis to assist level-ground and stair-descent gaits. *Neural Networks*, 21(4):654–666, 2008.
- [7] S. K. Au, J. Weber, and H. Herr. Powered ankle-foot prosthesis improves walking metabolic economy. *IEEE Transactions on Robotics*, 25(1):51–66, 2009.
- [8] L. N. Awad, J. Bae, K. O'Donnell, S. M. De Rossi, K. Hendron, L. H. Sloop, P. Kudzia, S. Allen, K. G. Holt, T. D. Ellis, et al. A soft robotic exosuit improves walking in patients after stroke. *Science Translational Medicine*, 9(400):eaai9084, 2017.
- [9] J. Bae, M. De Rossi, S. Marco, K. O'Donnell, K. L. Hendron, L. N. Awad, T. R. Teles Dos Santos, V. L. De Araujo, Y. Ding, K. G. Holt, et al. A soft exosuit for patients with stroke: Feasibility study with a mobile off-board actuation unit. In *Rehabilitation Robotics (ICORR), 2015 IEEE International Conference on*, pages 131–138. IEEE, 2015.
- [10] S. K. Banala, S. H. Kim, S. K. Agrawal, and J. P. Scholz. Robot assisted gait training with active leg exoskeleton (alex). *Neural Systems and Rehabilitation Engineering, IEEE Transactions on*, 17:2–8, 2009.
- [11] R. D. Bellman, M. A. Holgate, and T. G. Sugar. Sparky 3: Design of an active robotic ankle prosthesis with two actuated degrees of freedom using regenerative kinetics.

In *Biomedical Robotics and Biomechanics, 2nd IEEE RAS & EMBS International Conference on*, pages 511–516. IEEE, 2008.

- [12] T. Beltrame, R. Amelard, A. Wong, and R. Hughson. Prediction of oxygen uptake dynamics by machine learning analysis of wearable sensors during activities of daily living. *Scientific Reports*, 7, 2017.
- [13] S. Bhatnagar, H. Prasad, and L. Prashanth. *Stochastic Recursive Algorithms for Optimization: Simultaneous Perturbation Methods*, volume 434. Springer, 2012.
- [14] BionX. *Instructions for Use BiOM T2 Ankle*. Bedford, Massachusetts, 12 2015.
- [15] C. Bishop. *Pattern Recognition and Machine Learning*. Springer, New York, 2007.
- [16] O. M. Blake and J. M. Wakeling. Estimating changes in metabolic power from emg. *SpringerPlus*, 2(1):1, 2013.
- [17] J. A. Blaya and H. Herr. Adaptive control of a variable-impedance ankle-foot orthosis to assist drop-foot gait. *Neural Systems and Rehabilitation Engineering, IEEE Transactions on*, 12:24–31, 2004.
- [18] R. Blessey, H. Hislop, R. Waters, and D. Antonelli. Metabolic energy cost of unrestrained walking. *Physical Therapy*, 56(9):1019–1024, 1976.
- [19] J. Brockway. Derivation of formulae used to calculate energy expenditure in man. *Human Nutrition. Clinical Nutrition*, 41(6):463–471, 1987.
- [20] G. A. Brooks, T. D. Fahey, T. P. White, et al. *Exercise Physiology: Human Bioenergetics and Its Applications*. Mayfield Publishing Company, Mountain View, 1996.
- [21] R. C. Browning, J. R. Modica, R. Kram, A. Goswami, et al. The effects of adding mass to the legs on the energetics and biomechanics of walking. *Medicine and Science in Sports and Exercise*, 39(3):515, 2007.
- [22] K. P. Burnham and D. R. Anderson. Kullback-leibler information as a basis for strong inference in ecological studies. *Wildlife Research*, 28(2):111–119, 2001.
- [23] K. P. Burnham and D. R. Anderson. *Model Selection and Multimodel Inference: A Practical Information-Theoretic Approach*. Springer Science & Business Media, 2002.
- [24] S. M. Cain, K. E. Gordon, and D. P. Ferris. Locomotor adaptation to a powered ankle-foot orthosis depends on control method. *Journal of NeuroEngineering and Rehabilitation*, 4:48, 2007.
- [25] S. M. Cain, K. E. Gordon, and D. P. Ferris. Locomotor adaptation to a powered ankle-foot orthosis depends on control method. *Journal of Neuroengineering and Rehabilitation*, 4(1):48, 2007.

- [26] P. Candace Tefertiller, B. Pharo, et al. Efficacy of rehabilitation robotics for walking training in neurological disorders: a review. *Journal of Rehabilitation Research and Development*, 48(4):387, 2011.
- [27] J. M. Caputo, P. G. Adamczyk, and S. H. Collins. Optimizing prosthesis design to maximize user satisfaction using a tethered robotic ankle-foot prosthesis. In *Dynamic Walking*, 2015.
- [28] J. M. Caputo and S. H. Collins. Prosthetic ankle push-off work reduces metabolic rate but not collision work in non-amputee walking. *Scientific Reports*, 4:7213, 2014.
- [29] J. M. Caputo and S. H. Collins. A universal ankle-foot prosthesis emulator for human locomotion experiments. *Journal of Biomechanical Engineering*, 136(3):035002, 2014.
- [30] P. Cavanagh and P. Komi. Electromechanical delay in human skeletal muscle under concentric and eccentric contractions. *European Journal of Applied Physiology and Occupational Physiology*, 42(3):159–163, 1979.
- [31] C.-P. Chou and B. Hannaford. Measurement and modeling of mckibben pneumatic artificial muscles. *Robotics and Automation, IEEE Transactions on*, 12(1):90–102, 1996.
- [32] S. H. Collins and A. D. Kuo. Controlled energy storage and return prosthesis reduces metabolic cost of walking. *Power*, 600:800, 2005.
- [33] S. H. Collins, M. B. Wiggin, and G. S. Sawicki. Reducing the energy cost of human walking using an unpowered exoskeleton. *Nature*, 522(7555):212–215, 2015.
- [34] S. L. Delp, F. C. Anderson, A. S. Arnold, P. Loan, A. Habib, C. T. John, E. Guendelman, and D. G. Thelen. Opensim: open-source software to create and analyze dynamic simulations of movement. *Biomedical Engineering, IEEE Transactions on*, 54:1940–1950, 2007.
- [35] I. Díaz, J. J. Gil, and E. Sánchez. Lower-limb robotic rehabilitation: literature review and challenges. *Journal of Robotics*, 2011, 2011.
- [36] Y. Ding, I. Galiana, C. Siviý, F. A. Panizzolo, and C. Walsh. Imu-based iterative control for hip extension assistance with a soft exosuit. In *Robotics and Automation (ICRA), 2016 IEEE International Conference on*, pages 3501–3508. IEEE, 2016.
- [37] Y. Ding, F. A. Panizzolo, C. Siviý, P. Malcolm, I. Galiana, K. G. Holt, and C. J. Walsh. Effect of timing of hip extension assistance during loaded walking with a soft exosuit. *Journal of NeuroEngineering and Rehabilitation*, 13(1):87, 2016.
- [38] A. M. Dollar and H. Herr. Lower extremity exoskeletons and active orthoses: challenges and state-of-the-art. *Robotics, IEEE Transactions on*, 24(1):144–158, 2008.

- [39] J. M. Donelan, R. Kram, et al. Mechanical and metabolic determinants of the preferred step width in human walking. *Proceedings of the Royal Society of London B: Biological Sciences*, 268(1480):1985–1992, 2001.
- [40] J. M. Donelan, R. Kram, and A. D. Kuo. Mechanical work for step-to-step transitions is a major determinant of the metabolic cost of human walking. *Journal of Experimental Biology*, 205(23):3717–3727, 2002.
- [41] R. G. Eston, A. V. Rowlands, and D. K. Ingledeew. Validity of heart rate, pedometry, and accelerometry for predicting the energy cost of childrens activities. *Journal of Applied Physiology*, 84(1):362–371, 1998.
- [42] D. J. Farris and G. S. Sawicki. The mechanics and energetics of human walking and running: a joint level perspective. *Journal of The Royal Society Interface*, 9:110–118, 2011.
- [43] W. Felt, J. C. Selinger, J. M. Donelan, and C. D. Remy. “body-in-the-loop”: Optimizing device parameters using measures of instantaneous energetic cost. *PloS One*, 10(8):e0135342, 2015.
- [44] D. P. Ferris, J. M. Czerniecki, and B. Hannaford. An ankle-foot orthosis powered by artificial pneumatic muscles. *Journal of Applied Biomechanics*, 21(2):189–197, 2005.
- [45] D. P. Ferris, K. E. Gordon, G. S. Sawicki, and A. Peethambaran. An improved powered ankle-foot orthosis using proportional myoelectric control. *Gait & posture*, 23(4):425–428, 2006.
- [46] D. P. Ferris and C. L. Lewis. Robotic lower limb exoskeletons using proportional myoelectric control. In *Annual International Conference of the IEEE Engineering in Medicine and Biology Society*, pages 2119–2124. IEEE, 2009.
- [47] D. P. Ferris, G. S. Sawicki, and M. A. Daley. A physiologist’s perspective on robotic exoskeletons for human locomotion. *International Journal of Humanoid Robotics*, 4:507–528, 2007.
- [48] J. M. Finley, A. J. Bastian, and J. S. Gottschall. Learning to be economical: the energy cost of walking tracks motor adaptation. *The Journal of Physiology*, 591:1081–1095, 2013.
- [49] S. Galle, P. Malcolm, S. H. Collins, and D. De Clercq. Reducing the metabolic cost of walking with an ankle exoskeleton: Interaction between actuation timing and power. *Journal of NeuroEngineering and Rehabilitation*, 14(1):35, 2017.
- [50] S. Galle, P. Malcolm, S. H. Collins, J. Speeckaert, and D. De Clercq. Optimizing robotic exoskeletons actuation based on human neuromechanics experiments: Interaction of push-off timing and work. AMAM, 2015.

- [51] S. Galle, P. Malcolm, and D. De Clercq. 2d parameter sweep of bilateral exoskeleton actuation: push off timing and work. In *Dynamic Walking 2014*, 2014.
- [52] S. Galle, P. Malcolm, W. Derave, and D. D. Clercq. Adaptation to walking with an exoskeleton that assists ankle extension. *Gait & Posture*, 38(3):495 – 499, 2013.
- [53] S. Galle, P. Malcolm, W. Derave, and D. De Clercq. Uphill walking with a simple exoskeleton: Plantarflexion assistance leads to proximal adaptations. *Gait & Posture*, 41:246–251, 2015.
- [54] A. Gams, T. Debevec, T. Petric, and J. Babic. Metabolic cost of squatting using robotic knee exoskeleton. In *Raad 2012 Proceeding. 21th International Workshop on Robotics in Alpe-Adria-Danube Region*, page 184. ESA, 2012.
- [55] E. S. Gardinier, B. M. Kelly, J. Wensman, and D. H. Gates. A controlled clinical trial of a clinically-tuned powered ankle prosthesis in people with transtibial amputation. *Clinical Rehabilitation*, page 0269215517723054, 2017.
- [56] J. Geeroms, L. Flynn, R. Jimenez-Fabian, B. Vanderborght, and D. Lefeber. Ankle-knee prosthesis with powered ankle and energy transfer for cyberlegs  $\alpha$ -prototype. In *Rehabilitation robotics (ICORR), 2013 IEEE international conference on*, pages 1–6. IEEE, 2013.
- [57] A. S. Go, D. Mozaffarian, V. L. Roger, E. J. Benjamin, J. D. Berry, M. J. Blaha, S. Dai, E. S. Ford, C. S. Fox, et al. Heart disease and stroke statistics 2014 update: a report from the american heart association. *Circulation*, 129(3):e28, 2014.
- [58] C. C. Gordon, T. Churchill, C. E. Clauser, B. Bradtmiller, and J. T. McConville. Anthropometric survey of us army personnel: methods and summary statistics 1988. Technical report, DTIC Document, 1989.
- [59] K. E. Gordon and D. P. Ferris. Learning to walk with a robotic ankle exoskeleton. *Journal of Biomechanics*, 40(12):2636–2644, 2007.
- [60] K. E. Gordon, C. R. Kinnaird, and D. P. Ferris. Locomotor adaptation to a soleus emg-controlled antagonistic exoskeleton. *Journal of Neurophysiology*, 109:1804–1814, 2013.
- [61] R. D. Gregg and J. W. Sensinger. Towards biomimetic virtual constraint control of a powered prosthetic leg. *Control Systems Technology, IEEE Transactions on*, 22(1):246–254, 2014.
- [62] K. N. Gregorczyk, L. Hasselquist, J. M. Schiffman, C. K. Bensek, J. P. Obusek, and D. J. Gutekunst. Effects of a lower-body exoskeleton device on metabolic cost and gait biomechanics during load carriage. *Ergonomics*, 53(10):1263–1275, 2010.
- [63] T. M. Griffin, T. J. Roberts, and R. Kram. Metabolic cost of generating muscular force in human walking: insights from load-carrying and speed experiments. *Journal of Applied Physiology*, 95(1):172–183, 2003.

- [64] A. Gupta, M. K. O'Malley, V. Patoglu, and C. Burgar. Design, control and performance of ricewrist: a force feedback wrist exoskeleton for rehabilitation and training. *The International Journal of Robotics Research*, 27(2):233–251, 2008.
- [65] J. He, R. Kram, and T. A. McMahon. Mechanics of running under simulated low gravity. *Journal of Applied Physiology*, 71(3):863–870, 1991.
- [66] H. Herr. Exoskeletons and orthoses: Classification, design challenges and future directions. *Journal of NeuroEngineering and Rehabilitation*, 6(1):1, 2009.
- [67] J. Hicks, A. Seth, S. Hamner, and M. Demers. Simulation with opensim - best practices.
- [68] N. Hogan. A review of the methods of processing emg for use as a proportional control signal. *Biomedical Engineering*, 11:81–86, 1976.
- [69] K. W. Hollander, R. Ilg, T. G. Sugar, and D. Herring. An efficient robotic tendon for gait assistance. *Journal of Biomechanical Engineering*, 128:788–791, 2006.
- [70] T. G. Hornby, D. D. Campbell, J. H. Kahn, T. Demott, J. L. Moore, and H. R. Roth. Enhanced gait-related improvements after therapist-versus robotic-assisted locomotor training in subjects with chronic stroke. *Stroke*, 39(6):1786–1792, 2008.
- [71] T. Hortobágyi, A. Finch, S. Solnik, P. Rider, and P. DeVita. Association between muscle activation and metabolic cost of walking in young and old adults. *The Journals of Gerontology Series A: Biological Sciences and Medical Sciences*, 66(5):541–547, 2011.
- [72] M.-J. Hsu, D. H. Nielsen, S.-J. Lin-Chan, and D. Shurr. The effects of prosthetic foot design on physiologic measurements, self-selected walking velocity, and physical activity in people with transtibial amputation. *Archives of Physical Medicine and Rehabilitation*, 87(1):123–129, 2006.
- [73] H. Huang, D. L. Crouch, M. Liu, G. S. Sawicki, and D. Wang. A cyber expert system for auto-tuning powered prosthesis impedance control parameters. *Annals of Biomedical Engineering*, 44(5):1613–1624, 2016.
- [74] S. Huang, J. P. Wensman, and D. P. Ferris. An experimental powered lower limb prosthesis using proportional myoelectric control. *Journal of Medical Devices*, 8(2):024501, 2014.
- [75] K. Ingraham, D. Ferris, and C. D. Remy. Influence of uncertainty in metabolic dynamic time constant on instantaneous cost mapping techniques. In *Dynamic Walking 2016*, 2016.
- [76] K. A. Ingraham, D. P. Ferris, and C. D. Remy. Using wearable physiological sensors to predict energy expenditure. In *Rehabilitation Robotics (ICORR), 2017 International Conference on*, pages 340–345. IEEE, 2017.

- [77] R. W. Jackson and S. H. Collins. An experimental comparison of the relative benefits of work and torque assistance in ankle exoskeletons. *Journal of Applied Physiology*, 119(5):541–557, 2015.
- [78] R. W. Jackson, C. L. Dembia, S. L. Delp, and S. H. Collins. Estimated changes in muscle-level dynamics and energetics under different levels of exoskeleton-applied work and torque. In *Dynamic Walking 2015*, 2015.
- [79] R. Jimenez-Fabian and O. Verlinden. Review of control algorithms for robotic ankle systems in lower-limb orthoses, prostheses, and exoskeletons. *Medical Engineering & Physics*, 34:397–408, 2012.
- [80] P.-C. Kao and D. P. Ferris. Motor adaptation during dorsiflexion-assisted walking with a powered orthosis. *Gait & Posture*, 29:230–236, 2009.
- [81] P.-C. Kao, C. L. Lewis, and D. P. Ferris. Invariant ankle moment patterns when walking with and without a robotic ankle exoskeleton. *Journal of Biomechanics*, 43:203–209, 2010.
- [82] H. Kazerooni, J. Racine, L. Huang, and R. Steger. On the control of the berkeley lower extremity exoskeleton (bleex). In *Proceedings of the 2005 IEEE International Conference on Robotics and Automation*, pages 4353–4360. IEEE, 2005.
- [83] A. Kilicarslan, S. Prasad, R. G. Grossman, and J. L. Contreras-Vidal. High accuracy decoding of user intentions using eeg to control a lower-body exoskeleton. In *2013 35th Annual International Conference of the IEEE Engineering in Medicine and Biology Society (EMBC)*, pages 5606–5609. IEEE, 2013.
- [84] M. W. Kilpatrick, R. R. Kraemer, E. J. Quigley, J. L. Mears, J. M. Powers, A. J. Dedeia, and N. F. Ferrer. Heart rate and metabolic responses to moderate-intensity aerobic exercise: A comparison of graded walking and ungraded jogging at a constant perceived exertion. *Journal of Sports Sciences*, 27(5):509–516, 2009.
- [85] M. Kim, Y. Ding, P. Malcolm, J. Speeckaert, C. J. Siviý, C. J. Walsh, and S. Kuindersma. Human-in-the-loop bayesian optimization of wearable device parameters. *PLoS One*, 12(9):e0184054, 2017.
- [86] C. R. Kinnaird and D. P. Ferris. Medial gastrocnemius myoelectric control of a robotic ankle exoskeleton. *Neural Systems and Rehabilitation Engineering, IEEE Transactions on*, 17:31–37, 2009.
- [87] J. R. Koller, D. H. Gates, D. P. Ferris, and C. D. Remy. body-in-the-loop optimization of assistive robotic devices: A validation study. In *Robotics: Science and Systems Conference*, 2016.
- [88] J. R. Koller, D. H. Gates, D. P. Ferris, and C. D. Remy. Confidence in the curve: Establishing instantaneous cost mapping techniques using bilateral ankle exoskeletons. *Journal of Applied Physiology*, 122(2):242–252, 2017.

- [89] J. R. Koller, D. A. Jacobs, D. P. Ferris, and C. D. Remy. Learning to walk with an adaptive gain proportional myoelectric controller for a robotic ankle exoskeleton. *Journal of NeuroEngineering and Rehabilitation*, 12(1):1, 2015.
- [90] A. D. Kuo. Energetics of actively powered locomotion using the simplest walking model. *Journal of Biomechanical Engineering*, 124(1):113–120, 2002.
- [91] N. Lamarra, B. J. Whipp, S. A. Ward, and K. Wasserman. Effect of interbreath fluctuations on characterizing exercise gas exchange kinetics. *Journal of Applied Physiology*, 62(5):2003–2012, 1987.
- [92] B. E. Lawson, J. Mitchell, D. Truex, A. Shultz, E. Ledoux, and M. Goldfarb. A robotic leg prosthesis: Design, control, and implementation. *IEEE Robotics & Automation Magazine*, 21(4):70–81, 2014.
- [93] B. E. Lawson, H. A. Varol, A. Huff, E. Erdemir, and M. Goldfarb. Control of stair ascent and descent with a powered transfemoral prosthesis. *Neural Systems and Rehabilitation Engineering, IEEE Transactions on*, 21(3):466–473, 2013.
- [94] S. Lee and Y. Sankai. Power assist control for walking aid with hal-3 based on emg and impedance adjustment around knee joint. In *Intelligent Robots and Systems, 2002. IEEE/RSJ International Conference on*, volume 2, pages 1499–1504. IEEE, 2002.
- [95] C. L. Lewis and D. P. Ferris. Walking with increased ankle pushoff decreases hip muscle moments. *Journal of Biomechanics*, 41(10):2082–2089, 2008.
- [96] C. L. Lewis and D. P. Ferris. Invariant hip moment pattern while walking with a robotic hip exoskeleton. *Journal of Biomechanics*, 44(5):789–793, 2011.
- [97] D. Li, A. Becker, K. A. Shorter, T. Bretl, and E. Hsiao-Wecksler. Estimating system state during human walking with a powered ankle-foot orthosis. *Mechatronics, IEEE/ASME Transactions on*, 16:835–844, 2011.
- [98] M. Liu, P. Datsoris, and H. H. Huang. A prototype for smart prosthetic legs-analysis and mechanical design. In *Advanced Materials Research*, volume 403, pages 1999–2006. Trans Tech Publ, 2012.
- [99] V. Y. Ma, L. Chan, and K. J. Carruthers. Incidence, prevalence, costs, and impact on disability of common conditions requiring rehabilitation in the united states: stroke, spinal cord injury, traumatic brain injury, multiple sclerosis, osteoarthritis, rheumatoid arthritis, limb loss, and back pain. *Archives of Physical Medicine and Rehabilitation*, 95(5):986–995, 2014.
- [100] P. Maciejasz, J. Eschweiler, K. Gerlach-Hahn, A. Jansen-Troy, and S. Leonhardt. A survey on robotic devices for upper limb rehabilitation. *Journal of NeuroEngineering and Rehabilitation*, 11(3):10–1186, 2014.

- [101] P. Malcolm, W. Derave, S. Galle, and D. De Clercq. A simple exoskeleton that assists plantarflexion can reduce the metabolic cost of human walking. *PLoS One*, 8(2):e56137, 2013.
- [102] P. Malcolm, R. E. Quesada, J. M. Caputo, and S. H. Collins. The influence of push-off timing in a robotic ankle-foot prosthesis on the energetics and mechanics of walking. *Journal of NeuroEngineering and Rehabilitation*, 12(1):1, 2015.
- [103] L. V. McFarland, S. L. Hubbard Winkler, A. W. Heinemann, M. Jones, A. Esquenazi, et al. Unilateral upper-limb loss: satisfaction and prosthetic-device use in veterans and servicemembers from vietnam and oif/oef conflicts. *Journal of Rehabilitation Research & Development*, 47(4):299–316, 2010.
- [104] A. E. Minetti, C. Moia, G. S. Roi, D. Susta, and G. Ferretti. Energy cost of walking and running at extreme uphill and downhill slopes. *Journal of Applied Physiology*, 93(3):1039–1046, 2002.
- [105] L. M. Mooney and H. M. Herr. Biomechanical walking mechanisms underlying the metabolic reduction caused by an autonomous exoskeleton. *Journal of NeuroEngineering and Rehabilitation*, 13(1):4, 2016.
- [106] L. M. Mooney, E. J. Rouse, and H. M. Herr. Autonomous exoskeleton reduces metabolic cost of human walking during load carriage. *Journal of NeuroEngineering and Rehabilitation*, 11(1):1, 2014.
- [107] D. Novak, B. Beyeler, X. Omlin, and R. Riener. Workload estimation in physical human–robot interaction using physiological measurements. *Interacting with Computers*, 27(6):616–629, 2015.
- [108] R. Nuckols and G. S. Sawicki. The goldilocks zone: Interplay of elastic exoskeleton assistance and walking speed on the mechanics and energetics of walking. In *40th Annual Meeting of American Society of Biomechanics*, Raleigh, North Carolina, August 2016.
- [109] J. Olivier, A. Ortlieb, P. Bertusi, T. Vouga, M. Bouri, and H. Bleuler. Impact of ankle locking on gait implications for the design of hip and knee exoskeletons. In *2015 IEEE International Conference on Rehabilitation Robotics (ICORR)*, pages 618–622. IEEE, 2015.
- [110] R. E. Quesada, J. M. Caputo, and S. H. Collins. Increasing ankle push-off work with a powered prosthesis does not necessarily reduce metabolic rate for transtibial amputees. *Journal of Biomechanics*, 2016.
- [111] B. Quinlivan, S. Lee, P. Malcolm, D. Rossi, M. Grimmer, C. Siviyy, N. Karavas, D. Wagner, A. Asbeck, I. Galiana, et al. Assistance magnitude versus metabolic cost reductions for a tethered multiarticular soft exosuit. *Science Robotics*, 2(2):eaah4416, 2017.

- [112] D. Quintero, D. J. Villarreal, and R. D. Gregg. Preliminary experiments with a unified controller for a powered knee-ankle prosthetic leg across walking speeds. In *Intelligent Robots and Systems (IROS), 2016 IEEE/RSJ International Conference on*, pages 5427–5433. IEEE, 2016.
- [113] D. J. Reinkensmeyer et al. Slacking by the human motor system: computational models and implications for robotic orthoses. In *2009 EMBC*, 2009.
- [114] E. J. Rouse, L. M. Mooney, and H. M. Herr. Clutchable series-elastic actuator: Implications for prosthetic knee design. *The International Journal of Robotics Research*, 33(13):1611–1625, 2014.
- [115] S. J. Russell, P. Norvig, J. F. Canny, J. M. Malik, and D. D. Edwards. *Artificial Intelligence: A Modern Approach*, volume 2. Prentice hall Upper Saddle River, 2003.
- [116] G. S. Sawicki and D. P. Ferris. Mechanics and energetics of level walking with powered ankle exoskeletons. *Journal of Experimental Biology*, 211(9):1402–1413, 2008.
- [117] G. S. Sawicki, C. L. Lewis, and D. P. Ferris. It pays to have a spring in your step. *Exercise and Sport Sciences Reviews*, 37:130, 2009.
- [118] J. C. Selinger and J. M. Donelan. Estimating instantaneous energetic cost during non-steady-state gait. *Journal of Applied Physiology*, 117(11):1406–1415, 2014.
- [119] J. C. Selinger, S. M. OConnor, J. D. Wong, and J. M. Donelan. Humans can continuously optimize energetic cost during walking. *Current Biology*, 25(18):2452–2456, 2015.
- [120] K. Seo, J. Lee, Y. Lee, T. Ha, and Y. Shim. Fully autonomous hip exoskeleton saves metabolic cost of walking. In *Robotics and Automation (ICRA), 2016 IEEE International Conference on*, pages 4628–4635. IEEE, 2016.
- [121] R. Shadmehr and H. H. Holcomb. Neural correlates of motor memory consolidation. *Science*, 277:821–825, 1997.
- [122] M. K. Shepherd and E. J. Rouse. Design and characterization of a torque-controllable actuator for knee assistance during sit-to-stand. In *Engineering in Medicine and Biology Society (EMBC), 2016 IEEE 38th Annual International Conference of the*, pages 2228–2231. IEEE, 2016.
- [123] A. H. Shultz, J. E. Mitchell, D. Truex, B. E. Lawson, and M. Goldfarb. Preliminary evaluation of a walking controller for a powered ankle prosthesis. In *Robotics and Automation (ICRA), 2013 IEEE International Conference on*, pages 4838–4843. IEEE, 2013.

- [124] A. M. Simon, K. A. Ingraham, N. P. Fey, S. B. Finucane, R. D. Lipschutz, A. J. Young, and L. J. Hargrove. Configuring a powered knee and ankle prosthesis for transfemoral amputees within five specific ambulation modes. *PloS One*, 9(6):e99387, 2014.
- [125] J. A. Spanias, A. M. Simon, E. J. Perreault, and L. J. Hargrove. Preliminary results for an adaptive pattern recognition system for novel users using a powered lower limb prosthesis. In *Engineering in Medicine and Biology Society (EMBC), 2016 IEEE 38th Annual International Conference of the*, pages 5083–5086. IEEE, 2016.
- [126] W. A. Sparrow. *Energetics of human activity*. Human Kinetics, Windsor, 2000.
- [127] F. Sup, H. A. Varol, J. Mitchell, T. J. Withrow, and M. Goldfarb. Preliminary evaluations of a self-contained anthropomorphic transfemoral prosthesis. *IEEE/ASME Transactions on Mechatronics*, 14(6):667–676, 2009.
- [128] J. Takacs, C. L. Pollock, J. R. Guenther, M. Bahar, C. Napier, and M. A. Hunt. Validation of the fitbit one activity monitor device during treadmill walking. *Journal of Science and Medicine in Sport*, 17(5):496–500, 2014.
- [129] K. Z. Takahashi, M. D. Lewek, and G. S. Sawicki. A neuromechanics-based powered ankle exoskeleton to assist walking post-stroke: a feasibility study. *Journal of NeuroEngineering and Rehabilitation*, 12:23, 2015.
- [130] M. R. Tucker, J. Olivier, A. Pagel, H. Bleuler, M. Bouri, O. Lamercy, J. del R Millán, R. Riener, H. Vallery, and R. Gassert. Control strategies for active lower extremity prosthetics and orthotics: A review. *Journal of NeuroEngineering and Rehabilitation*, 12(1):1, 2015.
- [131] P. H. Tzu-wei, K. A. Shorter, P. G. Adamczyk, and A. D. Kuo. Mechanical and energetic consequences of reduced ankle plantar-flexion in human walking. *Journal of Experimental Biology*, 218(22):3541–3550, 2015.
- [132] T. K. Uchida, A. Seth, S. Pouya, C. L. Dembia, J. L. Hicks, and S. L. Delp. Simulating ideal assistive devices to reduce the metabolic cost of running. *PLoS One*, 11(9):e0163417, 2016.
- [133] B. R. Umberger and P. E. Martin. Mechanical power and efficiency of level walking with different stride rates. *Journal of Experimental Biology*, 210(18):3255–3265, 2007.
- [134] W. van Dijk, H. van der Kooij, and E. Hekman. A passive exoskeleton with artificial tendons: design and experimental evaluation. In *2011 IEEE International Conference on Rehabilitation Robotics*, pages 1–6. IEEE, 2011.
- [135] R. Villar, T. Beltrame, and R. L. Hughson. Validation of the hexoskin wearable vest during lying, sitting, standing, and walking activities. *Applied Physiology, Nutrition, and Metabolism*, 40(10):1019–1024, 2015.

- [136] C. J. Walsh, K. Endo, and H. Herr. A quasi-passive leg exoskeleton for load-carrying augmentation. *International Journal of Humanoid Robotics*, 4(03):487–506, 2007.
- [137] R. L. Waters and S. Mulroy. The energy expenditure of normal and pathologic gait. *Gait & posture*, 9(3):207–231, 1999.
- [138] M. Wehner, B. Quinlivan, P. M. Aubin, E. Martinez-Villalpando, M. Baumann, L. Stirling, K. Holt, R. Wood, and C. Walsh. A lightweight soft exosuit for gait assistance. In *Robotics and Automation (ICRA), 2013 IEEE International Conference on*, pages 3362–3369. IEEE, 2013.
- [139] B. J. Whipp. Rate constant for the kinetics of oxygen uptake during light exercise. *Journal of Applied Physiology*, 30(2):261–263, 1971.
- [140] M. Windrich, M. Grimmer, O. Christ, S. Rinderknecht, and P. Beckerle. Active lower limb prosthetics: A systematic review of design issues and solutions. *Biomedical Engineering Online*, 15(3):140, 2016.
- [141] D. Winter and H. Yack. Emg profiles during normal human walking: stride-to-stride and inter-subject variability. *Electroencephalography and Clinical Neurophysiology*, 67:402–411, 1987.
- [142] D. A. Winter. Kinematic and kinetic patterns in human gait: Variability and compensating effects. *Human Movement Science*, 3(1-2):51–76, 1984.
- [143] E. T. Wolbrecht, V. Chan, D. J. Reinkensmeyer, and J. E. Bobrow. Optimizing compliant, model-based robotic assistance to promote neurorehabilitation. *IEEE Transactions on Neural Systems and Rehabilitation Engineering*, 16(3):286–297, 2008.
- [144] T. H. Wonnacott and R. J. Wonnacott. *Regression: A second Course in Statistics*. Wiley New York, 1981.
- [145] A. R. Wu and A. D. Kuo. Determinants of preferred ground clearance during swing phase of human walking. *Journal of Experimental Biology*, 219(19):3106–3113, 2016.
- [146] T. Yan, M. Cempini, C. M. Oddo, and N. Vitiello. Review of assistive strategies in powered lower-limb orthoses and exoskeletons. *Robotics and Autonomous Systems*, 64:120–136, 2015.
- [147] A. Young and D. Ferris. State-of-the-art and future directions for robotic lower limb exoskeletons. *IEEE Transactions on Neural Systems and Rehabilitation Engineering*, 2016.
- [148] A. Young, T. Kuiken, and L. Hargrove. Analysis of using emg and mechanical sensors to enhance intent recognition in powered lower limb prostheses. *Journal of Neural Engineering*, 11(5):056021, 2014.

- [149] P. Zamparo, M. Francescato, G. Luca, L. Lovati, and P. Prampera. The energy cost of level walking in patients with hemiplegia. *Scandinavian Journal of Medicine & Science in Sports*, 5(6):348–352, 1995.
- [150] M. Zarrugh and C. Radcliffe. Predicting metabolic cost of level walking. *European Journal of Applied Physiology and Occupational Physiology*, 38(3):215–223, 1978.
- [151] J. Zhang, C. C. Cheah, and S. H. Collins. Experimental comparison of torque control methods on an ankle exoskeleton during human walking. In *Robotics and Automation (ICRA), 2015 IEEE International Conference on*, pages 5584–5589. IEEE, 2015.
- [152] J. Zhang, P. Fiers, K. A. Witte, R. W. Jackson, K. L. Poggensee, C. G. Atkeson, and S. H. Collins. Human-in-the-loop optimization of exoskeleton assistance during walking. *Science*, 356(6344):1280–1284, 2017.
- [153] H. Zhao, E. Ambrose, and A. D. Ames. Preliminary results on energy efficient 3d prosthetic walking with a powered compliant transfemoral prosthesis. In *Robotics and Automation (ICRA), 2017 IEEE International Conference on*, pages 1140–1147. IEEE, 2017.